UNIVERSITY of OKLAHOMA

GRADUATE COLLEGE

Observations and Simulations of the Southern Ocean Marine Boundary Layer Cloud Condensation Nuclei During the Austral Spring and Summer

A DISSERTATION

SUBMITTED TO THE GRADUATE FACULTY

In partial fulfillment of the requirement for the

Degree of

DOCTOR OF PHILOSOPHY

By Qing Niu

Norman, Oklahoma

2026

Observations and Simulations of Southern Ocean Marine Boundary Layer Cloud Condensation Nuclei during the Austral Spring and Summer

A DISSERTATION APPROVED FOR THE SCHOOL OF METEOROLOGY

BY THE COMMITTEE CONSISTING OF

Dr. Greg McFarquhar, Chair

Dr. Jens Redemann

Dr. Steven Cavallo

Dr. Deborah A. Trytten

Table of Contents

Abstract

During 2017 November - 2018 March Measurements of Aerosols, Radiation, and Clouds over the Southern Ocean (MARCUS) campaign the Atmospheric Radiation Measurement Program Mobile Facility-2 (AMF2) was installed on an Australian icebreaker conducting resupply voyages over the Southern Ocean (SO) (50°S–68°S, 63°E–150°E). The AMF2 captured the seasonal and latitudinal variation of Marine Boundary Layer (MBL) Cloud Condensation Nuclei (CCN) and clouds which play a crucial role in regulating radiative balance in the atmosphere. During the Austral spring and summer, two regions of cloud and aerosol patterns are seen over the north SO (north of 60°S, NSO) and the south SO (SSO) south of 62°S. During MARCUS, the NSO witnessed surface wind speed with a mode of 12-17 m s^{-1} from the N-W and surface pressure with two modes of 980 and 995 hPa, while the SSO has a wind speed mode of 4-8 m s^{-1} from the S-E and a single pressure mode of 975 hPa. When the ship was close to an extratropical cyclone center, decreased surface pressure, drastic changes of surface wind, increased precipitation, and decreased Marine Boundary Layer Height (MBLH) were consistently observed. The observed MBLH shows a Pearson correlation of 0.73 with the surface horizontal wind speed, consistent with the dominance of surface turbulent mixing over the open water. The increased surface CCN number concentration (N_{CCN}) observed south of 62°S is consistent with the presence of secondary CCN and their transport through katabatic flows above the MBL in the free troposphere so that wet scavenging is avoided. The age of these hypothesized sulfates is quantified using the ratio between the number of condensation nuclei (CN) to CCN (N_{CN}/N_{CCN}). Back-trajectories show that air

masses containing more fresh particles ($3.5 < N_{CN}/N_{CCN} < 16$) have a higher MBLH (median of 0.8-1 km) in their history compared to the air masses (MBLH median of 0.4-0.8 km) with $N_{CN}/N_{CCN} < 1.6$.

Previous studies identified that modeled MBL cloud droplet number concentration (N_d) is underestimated by a factor of 2 over the summertime SO close to the Antarctic coast. Here, comparisons between the observed CCN from MARCUS and simulated CCN from the Community Atmospheric Model 6 (CAM6) are presented. Modeled MBL N_{CCN} is underestimated, by close to 100% at latitudes south of 55°S with the N_{CCN} bias 1) largest close to the Antarctic coast during summer, implying the biased CCN type has seasonal and latitudinal variation and, 2) three times larger over sea ice than over open water, implying sea spray CCN are better simulated compared to secondary CCN. Assessments of aerosol size distribution indicate an underestimation of accumulation-mode-aerosols (Ac) with diameters 70 nm < D < 100 nm. CCN supersaturation spectra indicates that the observed CCN had lower hygroscopicity compared to simulated CCN, implying differences in CCN chemical composition. Because secondary aerosols including sulfate are less hygroscopic than sea salt CCN, the CCN-activation-ratio derived using bulk hygroscopicity kappa in the Abdul-Razzak function is under-calculated with an overestimation of critical supersaturation south of 62°S. For CCN serves as the nuclei on which water condense to activate, the biases reported here highlight shortfalls in simulated CCN that can be important to the well-documented underestimated N_d by Earth System Models, a key feature and uncertainty of pre-industrial conditions.

Further, the overestimate of sea salt and underestimate of sulfate as MBL CCN was investigated by adjusting surface emission parameterizations. For sea salt, when updating the 10-m wind (U_{10}) dependence from $U_{10}^{3.41}$ to $U_{10}^{2.8}$, the simulated N_{CCN} are within a factor of 2 of those observed for 74% of times over 50-55°S (previously 45%), while tripling the surface gaseous dimethyl sulfide emissions (DMS×3) increases agreement from 37% to 58% south of 55°S. In combination, these changes ($U_{10}^{2.8}$ and DMS×3) improve agreement between the simulated and surface-retrieved N_d. The mode of N_d increases from 40 cm^{-3} to 100 cm^{-3} after the updates, resulting in more reflective clouds along the Antarctic coast with an extra 5 ~ 12 W m^{-2} cloud shortwave forcing back to space. In detail, 1) the performance of the DMS×3 simulation depends not only on the absolute values of DMS emission over the SO, but also on regions and elevations where DMS is elevated; 2) the consequential increase in small sulfates and decrease in large sea salts makes the N_{CCN}-supersaturation (SS_w) spectra closer to that of observations. However, the observed shape of the spectra is not fully represented, implying this method does not completely solve the identified bias and further observations are thus needed.

1. Introduction

1.1. Southern Ocean as a natural test bed for natural CCN

The Southern Ocean (SO), surrounding the ice-covered Antarctic continent and sea ice, is the most pristine environment on Earth due to its remoteness from anthropogenic and continental aerosol sources (Hoose et al. 2009; Hamilton et al. 2014; McCoy et al. 2015; Uetake et al. 2020). Extratropical cyclones associated with the Antarctic Polar Front (Dong et al. 2006) are pervasive over the SO (Simmonds and Keay 2000; Hoskins and Hodges 2005; Lang et al. 2018) and are accompanied by high surface winds (Yuan et al. 2009), substantial low cloud cover (below 3 km altitude), and frequent boundary layer precipitation (Mace 2010; IPCC 2013; McCoy et al. 2014). In recent years, an increasing number of field campaigns have been conducted to sample both clouds and aerosol properties over the SO due to its unique remote and heterogeneous synoptically active environment (Schmale et al. 2019; McFarquhar et al. 2021).

Clouds forming in pristine regions, such as over the SO, are highly sensitive to perturbations of aerosols on which water vapor to condense on as nuclei to activate (Koren et al., 2014). However, the understanding of the sources and sinks of marine Cloud Condensation Nuclei (CCN) is limited, particularly south of 60°S, because of the paucity of measurements, leading to large uncertainties in the representation of aerosol processes in Earth System models. Humphries et al. (2021) showed that CCN and aerosols varied latitudinally over the SO, with Niu et al. (2024) subsequently illustrating that the increased number concentration of CCN-active aerosols is associated with

smaller values of scattering Angstrom Exponent and less hygroscopicity south of the 62°S compared to further north.

Beyond the observed latitudinal patterns of CCN, other recent studies have provided more information on the sources, sinks, and types of CCN. For example, Thomas et al. (2022) used a combination of satellite and reanalysis data between 45-65°S to illustrate that sea spray aerosols constituting sea salt and primary organic aerosols, hereafter called SS-CCN (Sea Spray CCN), dominate aerosol loading over the SO during the winter. Fossum et al. (2018) showed that the contributions of CCN from sea spray aerosols are higher for maritime air masses compared to those originating over the Antarctic continent, particularly when the surface wind speed is larger than 16 m s^{-1}. These strong surface winds are associated with the frequent extratropical cyclones over the SO around the storm track (Hanley et al. 2010).

Besides the SS-CCN, Humphries et al. (2015) found that ultra-fine particles with D <100 nm over the SO are linked to air masses originating over the Antarctic and form through gas-to-particle conversion and grow over both the sea ice marginal zone in the Marine Boundary Layer (MBL) and in the free troposphere over the Antarctic plateau (Lachlan-Cope et al. 2020). Quinn et al. (2017) showed that entrainment of free tropospheric homogeneous nucleated new particles into the Southern Hemisphere MBL produces Aitken mode aerosols, which can grow and eventually serve as CCN near the surface. Thus, the formation of secondary aerosols from biogenic gaseous emissions and gas to particle conversion is another key source of CCN, especially during summer when the SO is one of the most biologically active regions in the world (Ayers and Gras 1991; O'Dowd et al. 1997; Sim´o and Dachs 2002; McCoy et al. 2015; Fossum et al. 2018; Alroe et al.

2020). The aerosol precursors of these CCN come from gas-to-particle conversion that occurs through dimethyl sulfide (DMS) to methanesulfonic acid (MSA) or hydroperoxymethyl thioformate (HPMTF), and then to sulfur dioxide vapor and ultimately to sulfate aerosols (Chen et al, 2018; Veres et al., 2020). Quinn et al. (2017) and McCoy et al. (2021) pointed out that entrainment of free tropospheric nucleated new particles into the Southern Hemisphere MBL produces boundary layer Aitken mode aerosols, which can grow and serve as CCN near the surface. Recently, new particle formation events were also observed within the pristine MBL (Zheng et al., 2021), which impact the surface CCN budget. Humphries et al. (2015) found that ultra-fine particles, defined as particles with D <100 nm, over the SO are linked to air masses arriving from the Antarctic as new particle formation and growth events occur over both the sea ice marginal zone in the boundary layer and free troposphere over the Antarctic plateau (Lachlan-Cope et al. 2020). This CCN type hereafter is referred to as MB-CCN (Marine Biogenic CCN).

As for sinks, wet removal has been identified as the dominant sink of CCN and accumulation mode aerosols (Pruppacher and Klett 1997). Humphries et al. (2021) illustrate that the N_{CCN} is related to increases in the elevation of the originating air mass and a decrease in the accumulated total precipitation over the trajectory. Further, Kang et al. (2022) demonstrated that coalescence scavenging drives cloud droplet number concentration in SO low clouds. In fact, Tansey et al. (2023) showed that surface precipitation was observed 44% ± 4% of the time between April 2016 and March 2017 over Macquarie Island (54.5°S, 158.9°E) in the SO. The frequent drizzle over the SO and its wet scavenging/deposition effects can thus be a vital sink for the SO surface CCN (Sanchez et al., 2021; Humphries et al., 2021; Alinejadtabrizi et al., 2024).

The balance between precipitation sinks and the entrainment of sulfates and other aerosols into the MBL from the surface and free troposphere must be considered to determine the CCN concentration. All the above studies helped interpret the connections between varying processes acting on different types of CCN. In nature, however, one nucleus can be composed of multiple chemical compositions, and processes like coating and aging can add extra complexity to the CCN. Observations about CCN types thus are reported using, for example, fractional number and mass concentration (Humphries et al., 2021). Sanchez et al. (2021) tried to reduce this complexity by using a K-means cluster on SOCRATES (the Southern Ocean Clouds, Radiation, Aerosol Transport Experimental Study) field campaign data. They interpreted a scatter plot of N_{CCN} against total number concentration of aerosol nuclei N_{CN}, where K-means cluster was applied to label aerosols that could be identified through processes associated with their sources and sinks, such as Aged, Recent Particle Formation (RPF), plus Aged, Scavenged, and RPF plus scavenged.

In Chapter 2, data acquired by instruments on board the Aurora Australis (AA) during resupply voyages from Hobart, Australia, to Australian Antarctic research stations during the MARCUS field project (McFarquhar et al. 2021) are used to investigate latitudinal and seasonal sources and sinks of CCN over the SO. Chapter 2 aims at statistical investigations of meteorological factors that controls the N_{CCN}, particularly the increased amount of N_{CCN} close to the coast of Antarctic in January and February 2018.

1.2. Comparison of observed and simulated SO CCN

Earth System Models (ESMs) are used to interpret processes related to the sources and sinks of CCN in Chapter 3. Shortwave radiative fluxes calculated from the recent versions of ESMs

simulated clouds do not match those observed by satellites over the remote SO (Fiddes, S. L. et al., 2022; Medeiros et al., 2023). The high positive bias over the Antarctic Peninsula has been highlighted as one of the largest biases of reflected shortwave solar radiation over the Southern Hemisphere, and in fact, globally (Mallet et al., 2023). Mace et al. (2023) illustrated natural marine cloud brightening over the Antarctic marginal ice zone using satellite retrievals over the summertime SO, demonstrating that most scenarios with higher cloud droplet number concentration show up over the Antarctic coast.

McCoy et al. (2020) pointed out that a number of ESMs underestimated N_d over the summer SO by a factor of 2 compared to in-situ field measurements. Many models predict N_d based on the cloud supersaturation and availability of CCN. As such, an assessment of simulated CCN against observations acquired during field campaigns over the SO is necessary. In the Community Atmospheric Model 6 (CAM6, Bogenschutz et al., 2018), the activation of aerosol particles is represented using a parameterization (Abdul-Razzak and Ghan, 2000) based on the Kohler theory (Kohler et al., 1936), which directly takes into consideration the effects of particle size, composition, and hygroscopicity of participating species on particle activation. Specifically, the simulated CCN can be assessed from two aspects: 1) the number concentration of accumulation mode aerosols (Ac), which have dry diameters between 0.07 and 1 um (Schwartz, 1996) and form the majority of CCN (Williams et al. 2002, IPCC, 2024); and 2) the activation of these CCN-active Ac into cloud droplets, which can depend on aerosol type.

Lee et al. (2013) previously quantified the magnitude and causes of uncertainty of CCN in global models, showing that the dominant uncertainties in representing N_{CCN} in remote regions are aerosol

microphysical processes, including emission, sulfate formation during cloud-processing, and aerosol deposition. The observed N_{CCN} seasonality and aerosol size distributions over the SSO imply the potential existence of substantial sulfate CCN. In contrast, a larger contribution from primary sea spray aerosols was reported over the NSO (Humphries et al. 2015, 2021). Further, airborne measurements of substantial sulfate CCN in the lower troposphere over the SO were made by Twohy et al. (2021), Sanchez et al. (2021), and McCoy et al. (2021) during SOCRATES, conducted in the same Australasia sector of the SO as MARCUS in the 2018 summer over lower latitudes.

An assessment of simulated Ac in CAM6 against SOCRATES observations highlighted a consistent low bias in CAM6 of particles with diameters between 70 and 800 nm between the surface and up to 5-km at latitudes between 45°S and 62°S (McCluskey et al., 2023). Additionally, it was reported that the simulated particles with 100 nm < D < 500 nm were dominated by sea salt aerosol, whereas observed particles of the same size were dominated by sulfate (McCluskey et al., 2023). However, most airborne data do not extend poleward of 62°S, leading to the remote SSO being rarely targeted for CCN simulation and observation comparison studies.

In Chapter 3, MARCUS observations, including those acquired over the coastal Antarctic, are used to assess simulated CCN and aerosols over the SO by examining 1) CCN concentrations (Section 3.1), 2) Ac size and composition (Section 3.2), and 3) hygroscopicity (Section 3.3). Sea ice conditions are also analyzed to further interpret the bias of N_{CCN} (Section 3.4). Chapter aims at evaluating the simulation of primary and secondary CCN in an ESM with observations from MARCUS as bench marks.

1.3. Guiding Simulations with Observations

The work described in Chapter 3 is motivated by that in Chapter 2, which discussed the biases of SO N_{CCN}, namely 1) an overestimation of N_{CCN} at 0.2% and 0.5% supersaturation ($N_{CCN,\,0.2}$ and $N_{CCN,\,0.5}$) north of 55°S associated with an overestimation of accumulation mode sea salts, and 2) a close to 100% underestimation of $N_{CCN,\,0.2}$ and $N_{CCN,\,0.5}$ south of 55°S associated with an underestimation of secondary CCN, potentially sulfates. Chapter 4 aims at an observation-oriented modification of simulations to achieve better agreement between simulated and observed N_{CCN}, and to determine its influence on simulated N_d and solar radiation.

In atmospheric models such as CAM6, mixed aerosols are typically represented by several specific types. For the SS-CCN and MB-CCN, the most relevant CAM6-simulated aerosol types, respectively, are sea salt and sulfate. The sea salts are CCN-active particles that are emitted by bubbles bursting from the ocean surface, driven by surface winds. Empirical formulas as a function of horizontal wind speed at 10-m (U_{10}) parameterize sea salt emissions, which can be activated at given thermodynamic conditions based on the Köhler theory. The formation of secondary sulfate CCN, however, follows more complicated chemical processes.

In CAM6, biogenic volatile sulfurous and organic compounds, such as dimethyl sulfide (DMS, CH_3SCH_3), produced by phytoplankton and bacteria, represent an abundant natural source of sulfur (Hopkins et al., 2023; Teng et al., 2021; Ayers & Gras, 1991; Charlson et al., 1987). After its release to the atmosphere, DMS oxidizes to form methane sulfonic acid (MSA), sulfuric acid (H_2SO_4), and other oxidation products (Chen et al., 2018; Fung et al., 2022) that can lead to new particle formation in the free troposphere and MBL (Zheng et al., 2021). These ultrafine Aitken

particles can be transported through subsidence and entrainment, where they can further grow and act as CCN (Clarke et al., 1998).

The SO is where global DMS production maximizes but is poorly constrained in models (Bock et al. 2021; Revell et al., 2019). Efforts made to better describe and quantify complex sulfate/DMS oriented chemistry into ESMs are still ongoing (e.g., Kang et al. 2025, Jongebloed et al., 2024, Revell et al., 2019, Cala et al., 2023, Zhao et al., 2024). Instead of representing all the details of sulfate chemistry, this dissertation aims at investigating the balance between sea-salt and sulfates as SO CCN and its subsequent influence on N_d and radiation in the commonly used CAM6. For sulfate aerosols regulating SO CCN seasonal and latitudinal variation (McCluskey et al. 2023, McCoy et al. 2021, Niu et al. 2024, and Humphries et al. 2021), given CAM6 with its simplified chemistry, a stopgap is made to manually elevate the sulfur source by increasing surface DMS emission.

In Chapter 4, data acquired from the MARCUS, SOCRATES and CAPRICORN2 (Clouds Aerosols Precipitation Radiation and atmospheric Composition over the Southern Ocean) field campaigns during the 2018 summer are curated to investigate the CCN in the CAM6 model. In particular, 1) the CAM6 simulated N_{CCN} is modified by reducing sea salt emissions and increasing DMS emissions, 2) the performance of CAM6 with these modifications is evaluated by comparing simulations with observations during a sea-salt-dominant case and a sulfate-dominant case, 3) the sequential influence on N_d by comparing simulated N_d with those from surface-based remote sensing retrievals is checked, and 4) the resulted impacts on the top of atmosphere cloud shortwave radiative forcing is illustrated by comparing with the base-run results.

2. Untangling the meteorological controls of the Marine Boundary Layer Cloud Condensation Nuclei over the Southern Ocean – Results from MARCUS (II)

2.1. Introduction

Investigating the meteorological controls of the MBL CCN has always been a challenge given measurements of both aerosols and meteorology include signals on both locally weather-related scales and underlying large scales. The large-scale influences include seasonality for long-term single station (e.g. Cape Grim at Australia) observations, spatial and vertical variation for air-borne field campaigns (e.g. SOCRATES), and seasonal and spatial variation for ship-borne field campaigns (e.g. MARCUS). Therefore, to untangle these signals become important to understand the CCN budget.

Gras et al. (2017) applied multi-decadal observations of CCN at Cape Grim to characterize the instantaneous response of Ac number concentration on surface wind speed vary for aerosols with different size ranges. A positive wind dependence is found for Ac with $D > 350$ nm while a negative wind dependence is found for Ac with $100\ nm < D < 350\ nm$. This can be related to larger size Ac contain more wind-generated sea salts from surface injection while smaller size Ac are related to in-cloud growth mechanism involving aqueous-phase photochemical oxidation of gaseous precursors together with physical processes of diffusion and coalescence. It is therefore not surprising to see Sanchez et al. (2021) showing no significant correlation between surface wind and $N_{CCN,\ 0.3}$ during the SOCRATES given $N_{CCN,\ 0.3}$ provides an integrated number of Ac with different size.

Given the instantaneous influence of surface wind on N_{CCN} depend on the type of aerosols, the relative importance between the primary SS-CCN and the secondary MB-CCN thus become the key factor determine N_{CCN}. At Cape Grim, the dominance of SS-CCN can be used to explain the positive wind dependence of N_{CCN} in the winter, and the dominance of MB-CCN can explain the negative wind dependence in the summer. During MARCUS, Niu et al. (2024) illustrates an increased amount of small Ac (70 nm < D < 100 nm) and decreased amount of large Ac (700 nm < D < 1000 nm) over the SSO during the spring and summer. Together with analysis of hygroscopicity, Niu et al. (2024) hypothesized that the CCN over the NSO contains more primary sea salts while that close to the Antarctic contains substantial secondary sulfates. Combined with CAPRICORN data, Humphries et al. (2021) confirmed that 1) positive correlations between wind speed and chloride (as a tracer for sea salt) across the SO, and 2) pole-ward increased sulfate mass in chemical composition.

Beyond observations, the relative importance between the primary SS-CCN and the secondary MB-CCN is also the key simulating the CCN in the model. Niu et al. (2025) shows the bias of SO MBL N_{CCN} is strongly related to the sea ice condition, which can determine the balance between the primary and secondary CCN by reducing the SS-CCN emissions from the open water.

However, for lacking chemical compositions of CCN during the MARCUS, in this study we continued the method in Sanchez et al. (2020) where the aerosols acquired during the SOCRATES are clustered as “Fresh” or “Recent Particle Formation (RPF)” versus “Aged” using the ratio between CN and CCN. The Fresh/RPF air masses have substantial Aitken mode aerosols with D < 70 nm, indicative of recent particle formation. While the Aged regime represents cases in which

Ac is prominent and thus high N_{CCN}, likely due to atmospheric processes that increase particle size over time such as the condensation of VOC oxidation products or cloud processing.

Another challenge comes from the Ac have long residence times of approximately 5 days in the free troposphere at altitudes between 4 and 8 km because they do not sediment quickly nor coagulate easily (Williams et al. 2022). Therefore, both the current sources and sinks, the vertical and horizontal transportation, and the history of the airmasses can all influence on the measured MBL N_{CCN}.

Given the N_{CCN} are often found to be higher above the SO MBL (Hudson et al. 1998) with longer lifetime compared to that within the MBL, the air mass elevation along the history is of consider as an influencing factor in this analysis.

In this Chapter, data acquired by instruments on board the Aurora Australis (AA) during resupply voyages from Hobart, Australia to Australian Antarctic research stations during the Measurements of Aerosols, Radiation, and Clouds over the Southern Ocean (MARCUS) field project (McFarquhar et al. 2021) are used to untangle the meteorological factors controlling the N_{CCN} over the SO.

2.2. Methods

2.2.1. Instrumentation

Aerosol measurements, instrumentation and quality control for MARCUS data are described in Section 2 in Niu et al. (2024). Details of ship location, carbon monoxide and ozone measurement, weather balloons with radiosondes, meteorological variables acquired using Vaisala weather transmitter (WXT520) including surface wind and pressure are described in Niu et al. (2021).

2.2.2. Relative location in cyclone system

The Extratropical Cyclones and Fronts Database (Naud et al., 2010) was also used to generate environmental variables associated with cyclone systems. This dataset includes 6 hourly cyclone information detected and tracked by the MCM system version 4 using the ERA-interim sea level pressure (SLP), and front locations detected by the MERRA-2 gridded SLP (data can be found via https://portal.nccs.nasa.gov/datashare/Obs-ETC/Fronts-ETC/). In this dissertation, the nearest storm was first found according to the distance between the ship and storm center. The distance between the closest low center location and the AA is only used when the AA is sufficiently close (< 1000 km) and associated with a cyclone system via manual and subjective judgement. The associated cyclone center applies to all time periods during the period 3 hours before and after the time of each reanalysis field. To understand the relationship between the wind directions and the ship's relative location to its closest cyclone center, the relative distance has been calculated using the square root of the latitude and longitude differences as a general evaluation. The relative distance is calculated using the Haversine formula assuming a spherical Earth with great-circle distances, with the latitude and longitude of AA and its closest cyclone center as inputs.

2.2.3. HYSPLIT4 back trajectory simulation

The Hybrid Single Particle Lagrangian Integrated Trajectories (Hysplit4, Stein et al. 2015) model is used to derive 120-hour back trajectories with one hour time resolution. The Global Data Assimilation System (GDAS) reanalysis data are used as meteorology input (ftp://arlftp.arlhq.noaa.gov/pub/archives/gdas1/). The starting point is the location of AA at 50 meters above ground level (AGL), which is around the aerosol inlet in AMF2. The 4-D results of the back trajectories are collocated with the 1 degree 1 hour frequency ERA-5 reanalysis fields which provide the total precipitation, mixing layer depth, and low cloud coverage. To evaluate the

quality of the ERA5 fields, the Marine Boundary Layer Height (MBLH) is derived using the soundings released from the Balloon-Borne Sounding System (Riihimaki et al., doi.org/10.5439/1991783) on the AA. The boundary layer depth is calculated from the bulk Richardson number using a critical threshold of 0.25 (Weisman, M. L., and J. B. Klemp, 1982). Details and comparisons of the MBLH between the ERA5 and that from the sondes is presented in Section 2.3. After quality testing, the MBLH from the ERA5 is collocated with the Hysplit4 back trajectories so that MBLH along the air mass history can be known.

2.3. Results

2.3.1. Pressure, Wind, and Storms

With the analysis of N_{CCN} as a function of season and latitude have been carried out in Niu et al. (2024), the meteorology during which the measurements are acquired are also investigated. In this section, surface pressure, surface wind, and the adjacency of storms are illustrated.

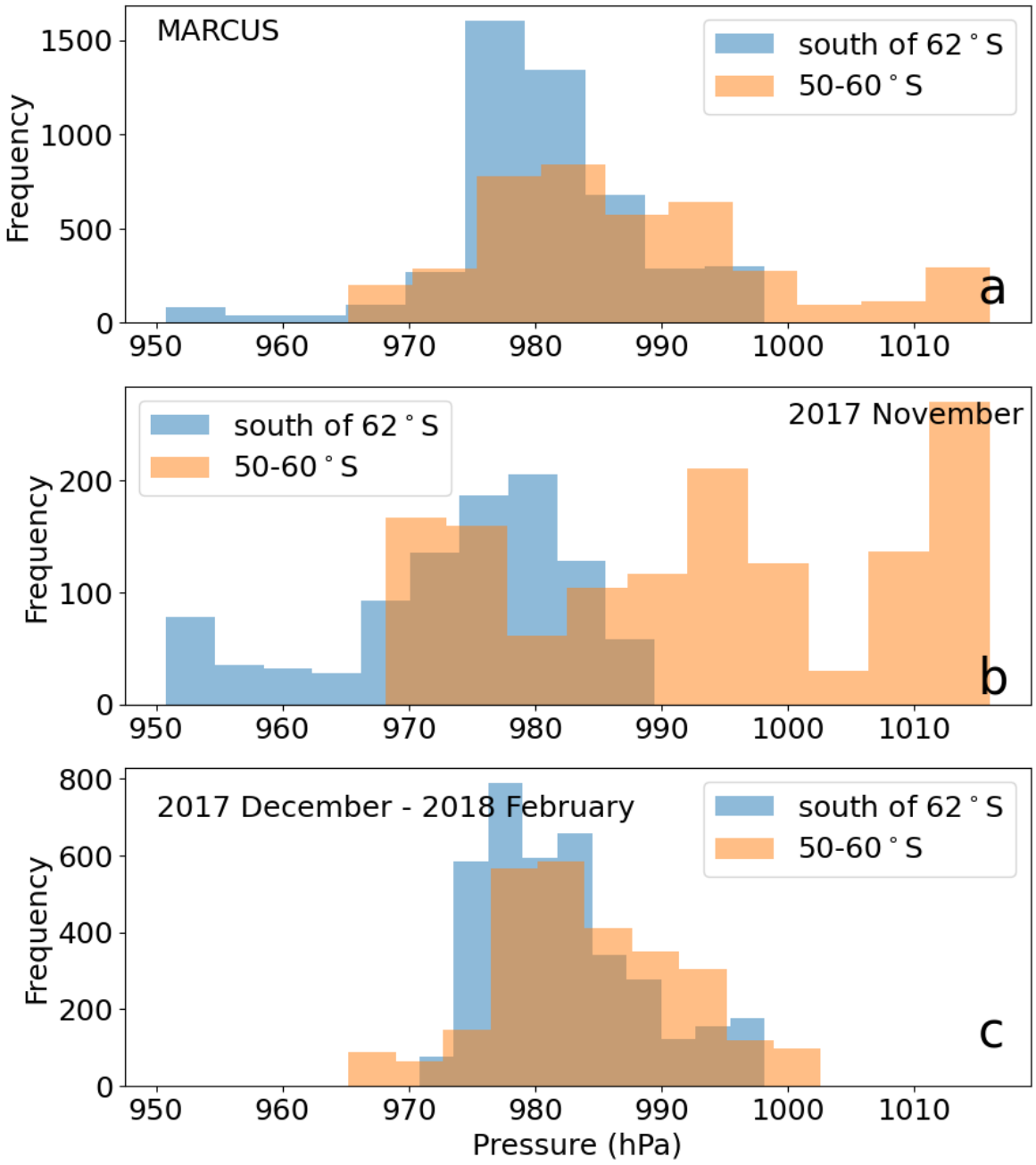

Figure 2.1 Histogram of surface pressure measured by the Vaisala weather transmitter (WXT530) over the north Southern Ocean (NSO, 50-60°S) in orange, over the south Southern Ocean (SSO, south of 62°S) during the whole MARCUS in a, during November 2017 in b, and during December 2018 – February 2018 in c.

Figure 2.1 illustrates the distribution of surface pressure measured onboard the AA, showing that both the scenarios of $P < 975$ hPa and $P > 1000$ hPa are more frequent over the NSO (in orange)

during the 2017 November compared to December 2017 – February 2018. Fig 2.1a shows the full distribution of surface pressure during MARCUS, which shows a statistically significant higher pressure for the NSO than SSO ($P < 0.05$). Pressures over the NSO have a range of 965 - 1015 hPa with modes at 980 hPa and 990 hPa, while that over the SSO has a range of 950-1000 hPa with a single mode at 975 hPa. This is consistent with the NSO is close to the extratropical high and the SSO is close to the sub-polar low. This distribution is further analyzed by season in Fig 2.1b (November 2017) and Fig 1c (December 2017 – February 2018).

The wide distribution of surface pressure in Fig 2.1a is largely contributed by the samples acquired during the spring (Fig 2.1b, November 2017). In Fig 2.1b, the high and low values of pressure can be related to the greater meridional amplitude of Rossby waves in November. In November, while SSO is closer to the polar core, dominated by cold air, the mid-latitudes are much warmer in the spring, resulting in a strong meridional temperature gradient over the NSO. It enhances the westerlies and their vertical shear, reinforcing strong baroclinicity and storm formation over the NSO. More pronounced waviness in the November isobars in Fig S2.1a may steer the storms into the lower-pressure-SSO (blues of $P < 969$ hPa in Fig 2.1b), in combination resulting in the lowest pressures during MARCUS.

During summer (Fig 2.1c, Dec 2017 - Feb 2018), the warming Antarctic received stronger solar radiation. Sea ice retreat over the SSO enables the temperature contrast between NSO and SSO to weaken, thus the sub-polar lows get less intense. This is consistent with Fig 2.1c in which blue values get increased compared to Fig 2.1b. In summary, though the lowest pressure shows up during the December 2017 - February 2018 over SSO, the storms are more often over the NSO. And these NSO storms during the November are often stronger than those during the other months.

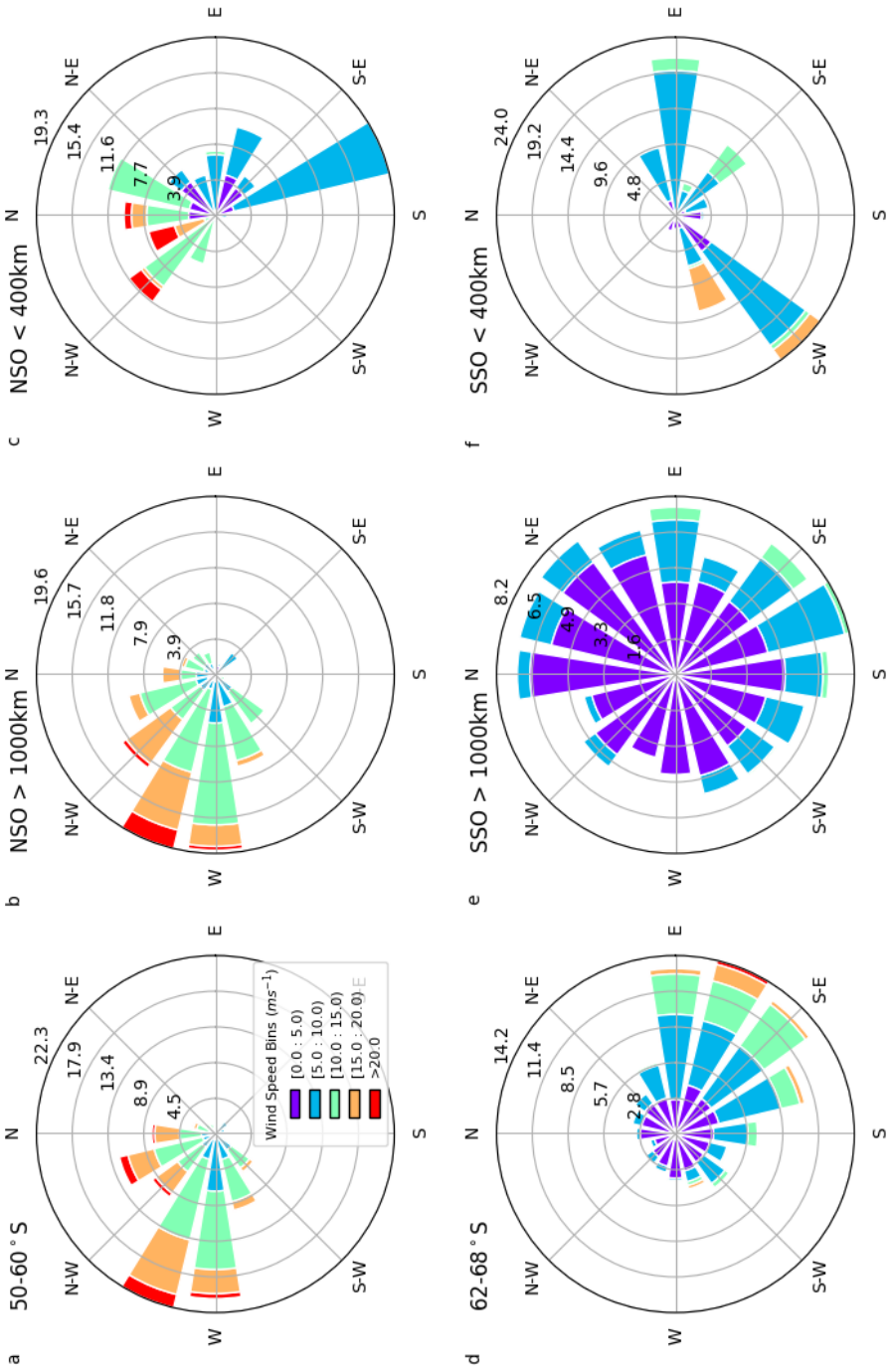
a
50-60 ° S
b
NSO > 1000km
c
NSO < 400km
d
62-68 ° S
e
SSO > 1000km
f
SSO < 400km
N
N-E
E
S-E
S
S-W
W
N-W
Wind Speed Bins (ms⁻¹)
[0.0 : 5.0)
[5.0 : 10.0)
[10.0 : 15.0)
[15.0 : 20.0)
>20.0

Figure 2.2 Wind-Rose velocity plots generated using wind speed and direction measurements obtained with the Vaisala weather transmitter (WXT530) during MARCUS. Data measured over the NSO (50-60°S) in a, and over the SSO (south of 62°S) in d. Clustering by the distance between AA and its closest cyclone center is applied to illustrate the scenarios with limited influence from the storms (D < 400 km, c and f) and with intense influence from the storm (D > 1000 km, b and e).

Figure 2.2 illustrates the distribution of surface wind during the MARCUS by the relative distance to the closest cyclone center. Fig 2.2a shows the NSO has north-westerly (NW) with a stronger mode of 10-15 m s^{-1}, while the south-easterlies (SE) sampled over the SSO (south of 62°S, Fig. 2.2d) have a weaker mode of 5-10 m s^{-1}. This is also consistent with the density of isobars in Fig S2.1. The prevailing winds of NW over NSO and SE over the SSO are consistent with the surface wind in the Ferrel Cell and the Polar Cell, respectively. When close to cyclones, the wind speed becomes higher.

With D > 1000 km, the influence of extratropical cyclones on the ship-borne wind should be limited (Fig 2.2b and Fig 2.2e). Fig 2.2b shows dominant prevailing N-W wind, consistent with Fig 2.2a, implying the wind over the NSO are dominantly westerlies except when the ship is close to storms (Fig 2.2c). Fig 2.2f shows all the winds > 15 m s^{-1} are associated with storms over the SSO. Fig 2.2e shows that when the AA is away from any of a storm, the winds are usually < 10 m s^{-1} and come from almost any direction, with only a slightly higher frequency of easterlies.

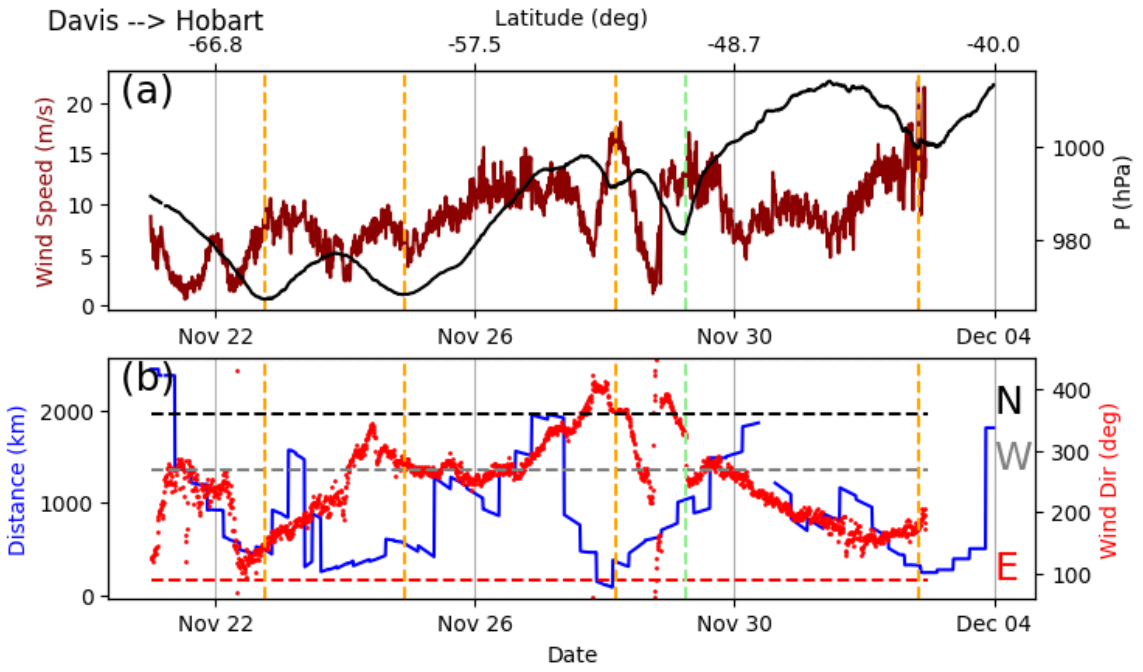

Figure 2.3 Time series of wind speed (brown) and surface pressure (black) in a, and wind direction (red) and relative distance between AA and the closest cyclone center (blue) in b during the voyage from Davis to Hobart, with the corresponding latitudes labeled on the top. Wind direction and that plus 360° are plotted for visualization continuity, with the dashed horizontal lines illustrating the wind direction of west (W), north (N), and east (E). The dashed orange lines identify the times when AA is heavily influenced by its closest cyclone < 400 km. The dashed light-green line identifies an event on 2017-11-29 0600Z that is influenced by its closest cyclone > 400 km away. Wind and pressure are measured by the Vaisala weather transmitter (WXT530) onboard. Storm center information is from the Modern-Era Retrospective analysis for Research and Applications (MERRA-2) data.

While the AA is a mobile observing platform, the cyclones are developing and moving at the same time. In Figure 2.3, when the AA is thus sampling conditions influenced by the cyclone center, indicated by the orange dashed lines, there are coincident lows of surface pressure (black curves in Fig 2.3a). At 2017-11-28 04:00, the AA is influenced by an extratropical cyclone nearby. The minimum of pressure corresponds to a high of wind speed (brown curves in Fig 2.3a). This can be related to the fact that the high wind is associated with the strong temperature gradient close to the storms and fronts associated with its closest cyclone. This is also consistent with the drastic change of wind directions from northerly to easterly in Fig 2.3b. After this, there is a short recovery of the

northerly which is related to another cyclone on 2017-11-29 0600Z (green dashed line). The maps of mean sea level (MSL) pressure from the ERA5 data during 2017-11-27 to 2017-11-29 are shown in Figure S2.2-2.4 to show the consistency with Figure 2.3. The geo-location of the low-pressure center relative to the AA (blue lines) can also be confirmed. Like the voyage from Davis to Hobart, the other voyages between Hobart, Australia, and the Antarctic stations are included in Figure S2.2. In total, we identified 14 events during the MARCUS voyages when AA is < 400 km away from a cyclone.

2.3.2. Marine Boundary Layer Height

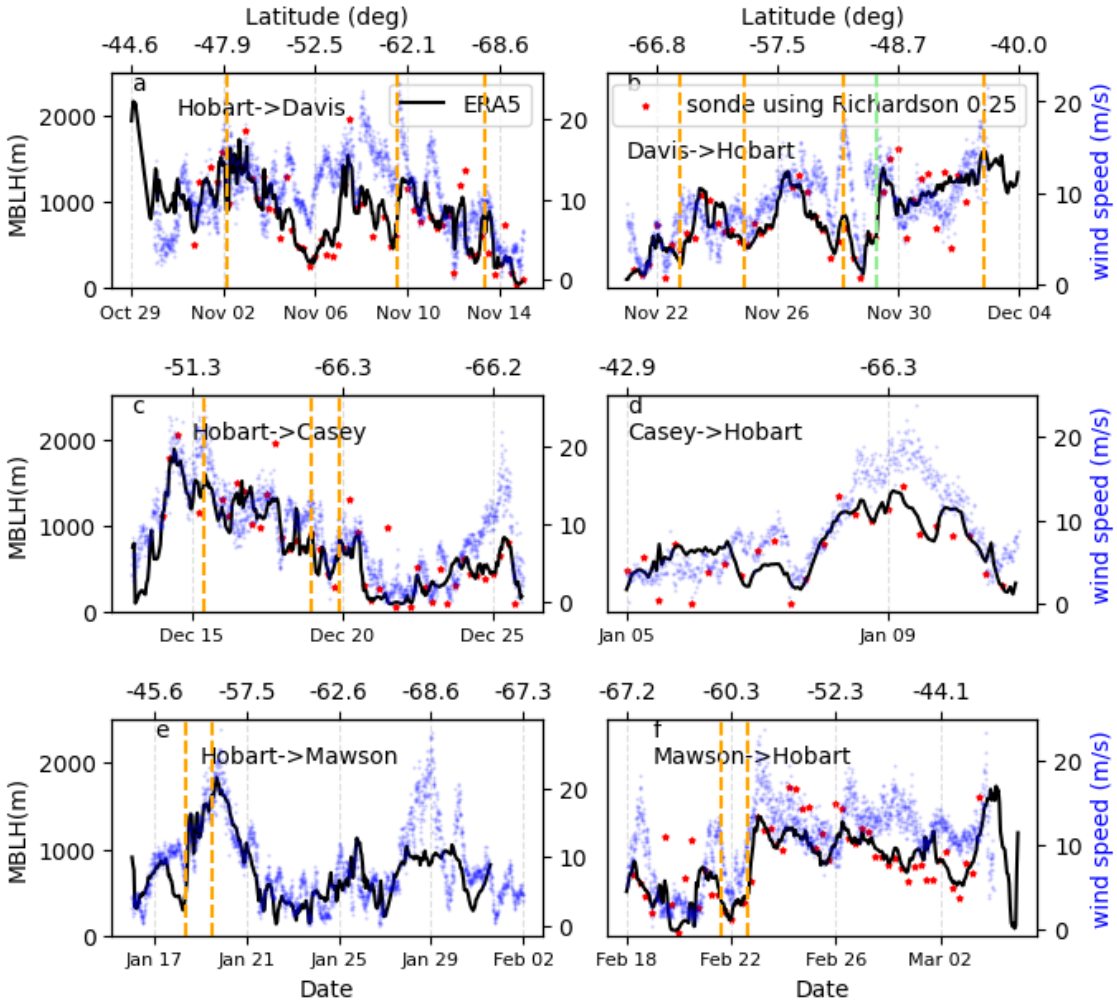

Figure 2.4 Marine Boundary Layer Height (MBLH) in black and surface wind speed in blue as a function of time during MARCUS voyages between Hobart and the Antarctic stations, with corresponding latitudes marked on the top. Red dots are the MBLH derived using the sonde data, and black lines are those from the ERA5 after co-location with the AA location. Vertical orange lines indicate the times when AA is < 400 km to a cyclone center, as the orange lines in Figure 3 and S2.

Figure 4 shows the corresponding MBLH above mean sea level calculated from bulk Richardson number, buoyancy (stability) divided by shear (turbulence production), using a critical threshold of 0.25 (Richardson et al., 1922). In Figure 4, the sonde data acquired during MARCUS are used to calculate the MBLH (red dots), and the ERA5 data of MBLH are compared with (black lines). A linear regression is applied on the results of the two methods, deriving MBLH (scatter plot in Figure S2.4), with a Pearson correlation coefficient of 0.7 and RMSE of 233 m (Figure S2.5). This result provides confidence that the MBLH calculated from ERA5 are robust and useful for analysis, which is important considering the sonde data are only available 4 times per day with missing data during both intense weather and the voyage from Hobart to Mawson (Fig. 2.4e). For the 14 of 15 events influenced by the cyclones shown by orange and green vertical dashed lines in Figure 2.4, the MBLH curves have discontinuity points.

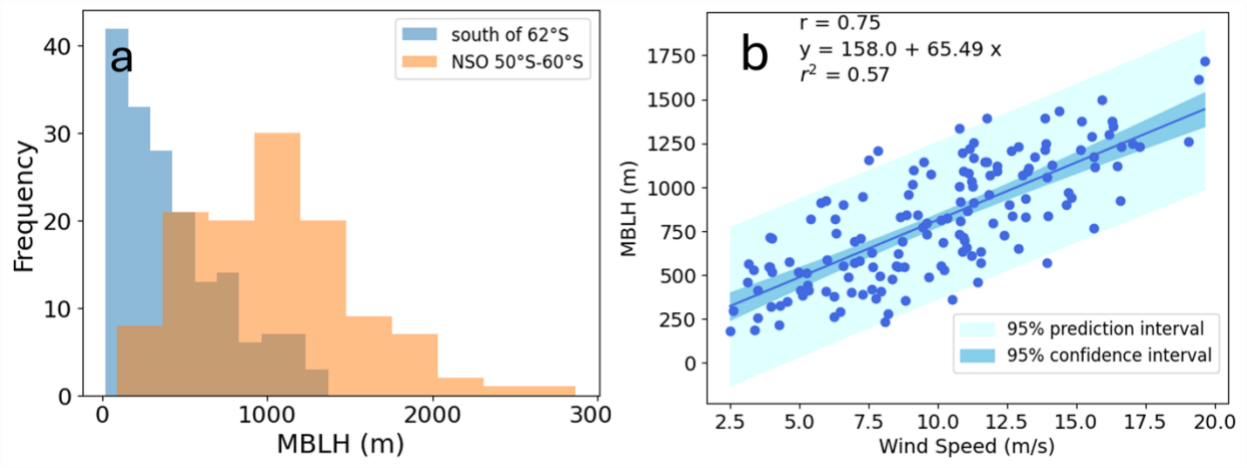

Figure 2.5 Histogram of MBLH above the mean sea level from the ERA5 (a) over NSO in yellow and over SSO in blue during the MARCUS. Linear fits between the surface wind speed and the

MBLH is shown in (b), with light and dark shading indicating the 95% prediction interval and 95% confidence interval, respectively.

The relationship between the MBLH and wind speed is shown in Figure 2.5. Fig. 2.5a shows that the values of MBLH have a mode of 1000 m above mean surface level over the NSO (yellow), larger than the MBLH values shown over the SSO (blue) that have no prominent mode. Fig. 2.5b shows the MBLH from the ERA5 is linearly correlated with the surface wind speed, with a Pearson correlation coefficient of 0.75 and $P < 0.01$. This is consistent with wind-driven turbulence being the dominant mixing mechanism in the boundary layer, with the higher wind speed at the surface promoting vertical mixing and deepening the MBL. Turbulence typically homogenizes the cloud-containing layer, frequently coupling this layer to the surface source of moisture that maintains the cloud layer (e.g., Nicholls 1984; Bretherton and Wyant 1997). Figure 2.5 is consistent with results from the wind rose plots in Figure 2.2, given that the surface wind speeds over the NSO are larger compared to those over the SSO, just as the MBLHs are larger over the NSO. Over the open water over NSO, higher wind speeds increase both latent and sensible heat fluxes, which can destabilize the MBL and promote upward mixing, thus raising its top.

2.3.3. Back trajectories from Hysplit4

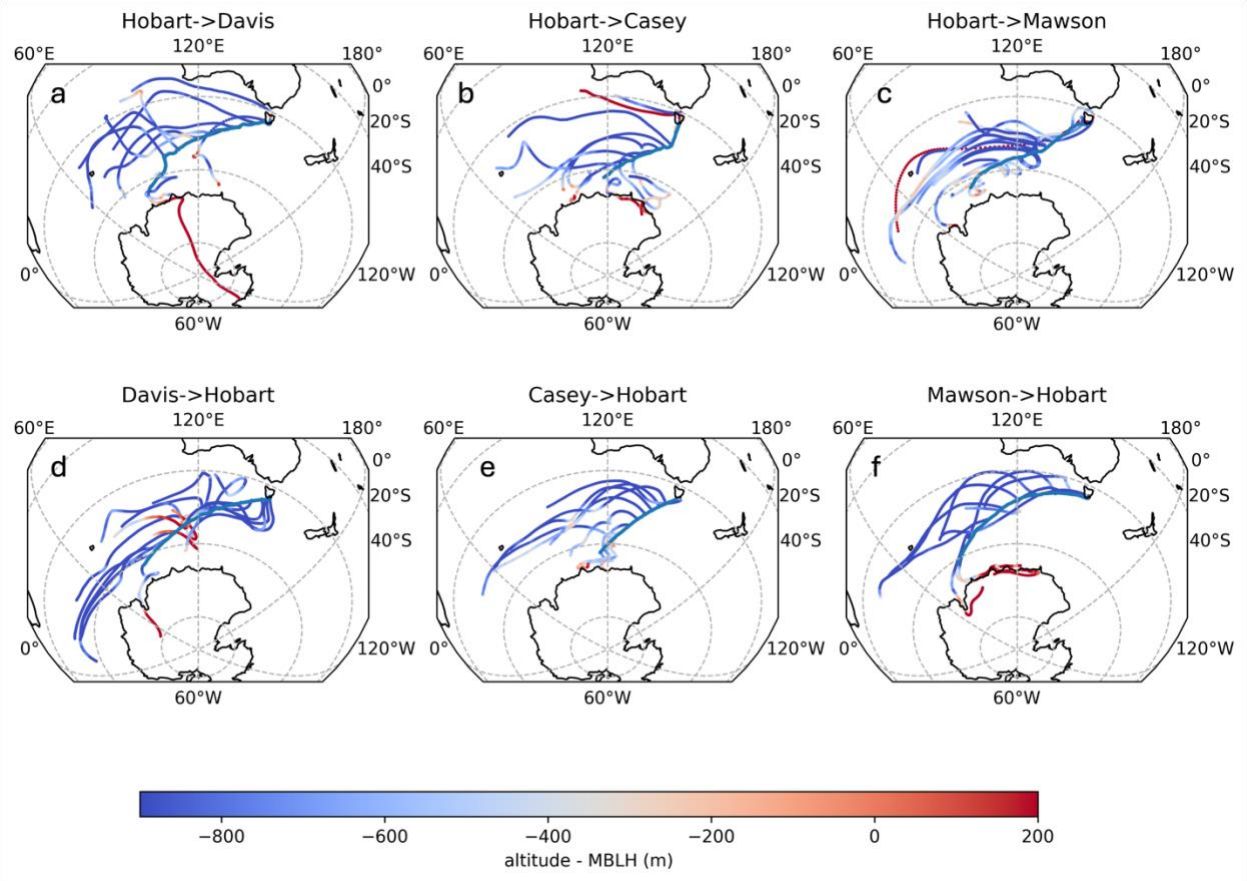

Figure 2.6 Hysplit4 120 back trajectory results overlaid on the map over the 45-60°S for each MARCUS voyage colored by the values of altitude minus the MBLH as determined from the ERA5 reanalysis. The AA ship track is overlaid on the map.

The relative location of the air masses' origins to the MBL in the 120-h history is illustrated in Figures 2.6 and 2.7. Figure 2.6 shows that most of the air for those parts of the MARCUS voyages over the NSO comes from the west, consistent with the strong dominance of the westerlies seen in Figure 2.2. It is also seen in Figure 2.6 that with a starting point north of 60°S for the Hysplit4, most of the air masses stay within the MBL during their transport over the SO, as indicated by the blue coloring. However, there are several exceptions when the air mass gets close to cyclone centers over the NSO when the MBL is lower (decreased wind speed at the center of the cyclone).

There are also times when the histories show the origins of air masses are close to the Antarctic continent (the reds by the Antarctic coast).

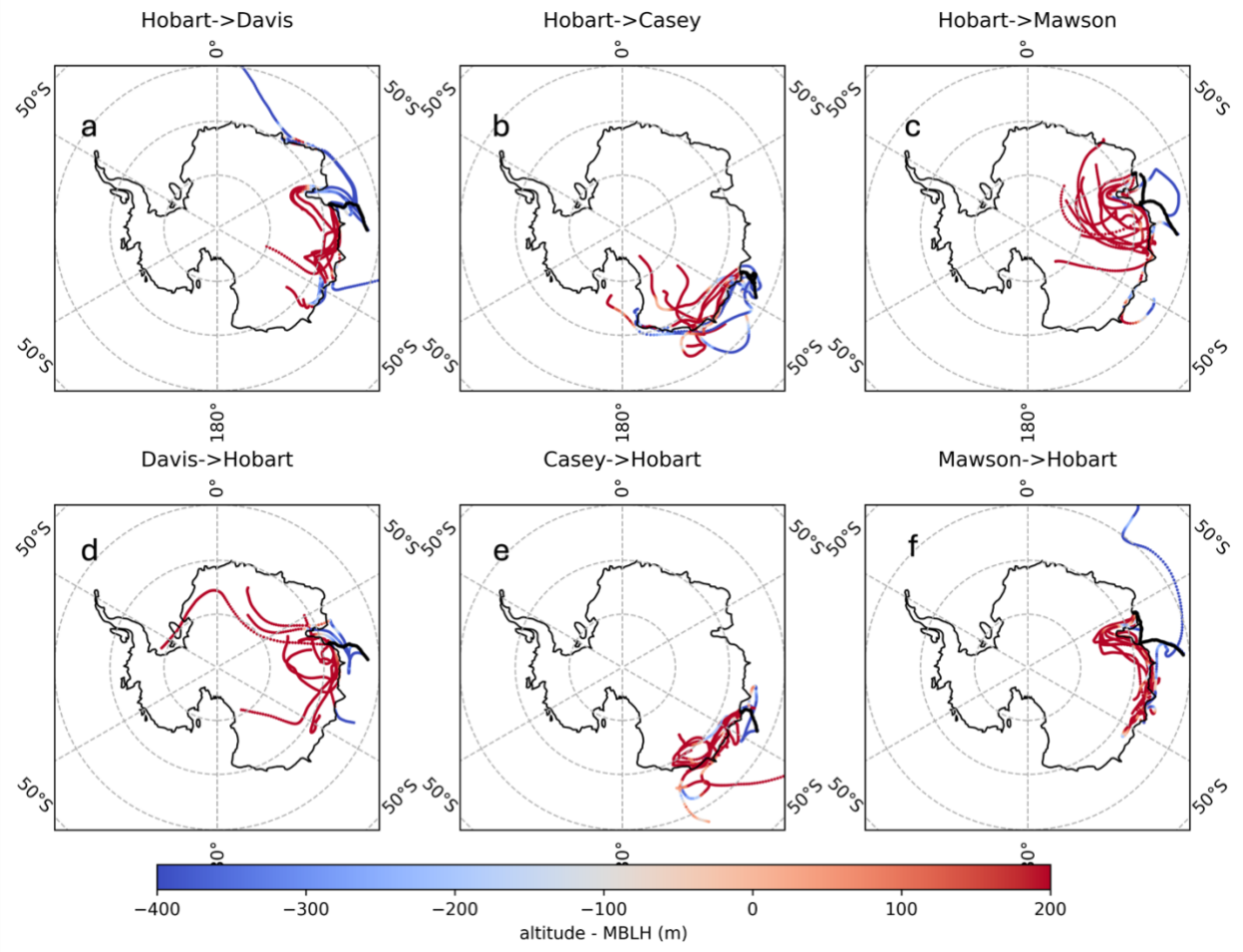

Figure 2.7 As in Figure 2.6, except for the Hysplit4 with starting points over south of 62°S.

Figure 2.7 shows that easterlies prevailed over the SSO during MARCUS, but that the surface wind directions air mass origins had have a larger range. Figure 2.7 shows that most air masses over the SSO are transported from above the MBL as indicated by the red coloring. Given precipitation mainly occurs in the boundary layer (Stull R. B., 1988), air masses transported above

the MBL should be less influenced by processes such as wet scavenging by rain or snow. Furthermore, these air masses above the MBL are less influenced by surface conditions (e.g., sea ice, water, or both), which serve as potential sources for primary CCN. This is consistent with Niu et al. (2024) and the analysis discussed in Chapter 3, which shows CCN over the SSO have smaller sizes in the summer and are mostly secondary CCN. The simulated air mass origin and its elevation get confirmed in surface-observed carbon monoxide and ozone, shown in Figure 2.8.

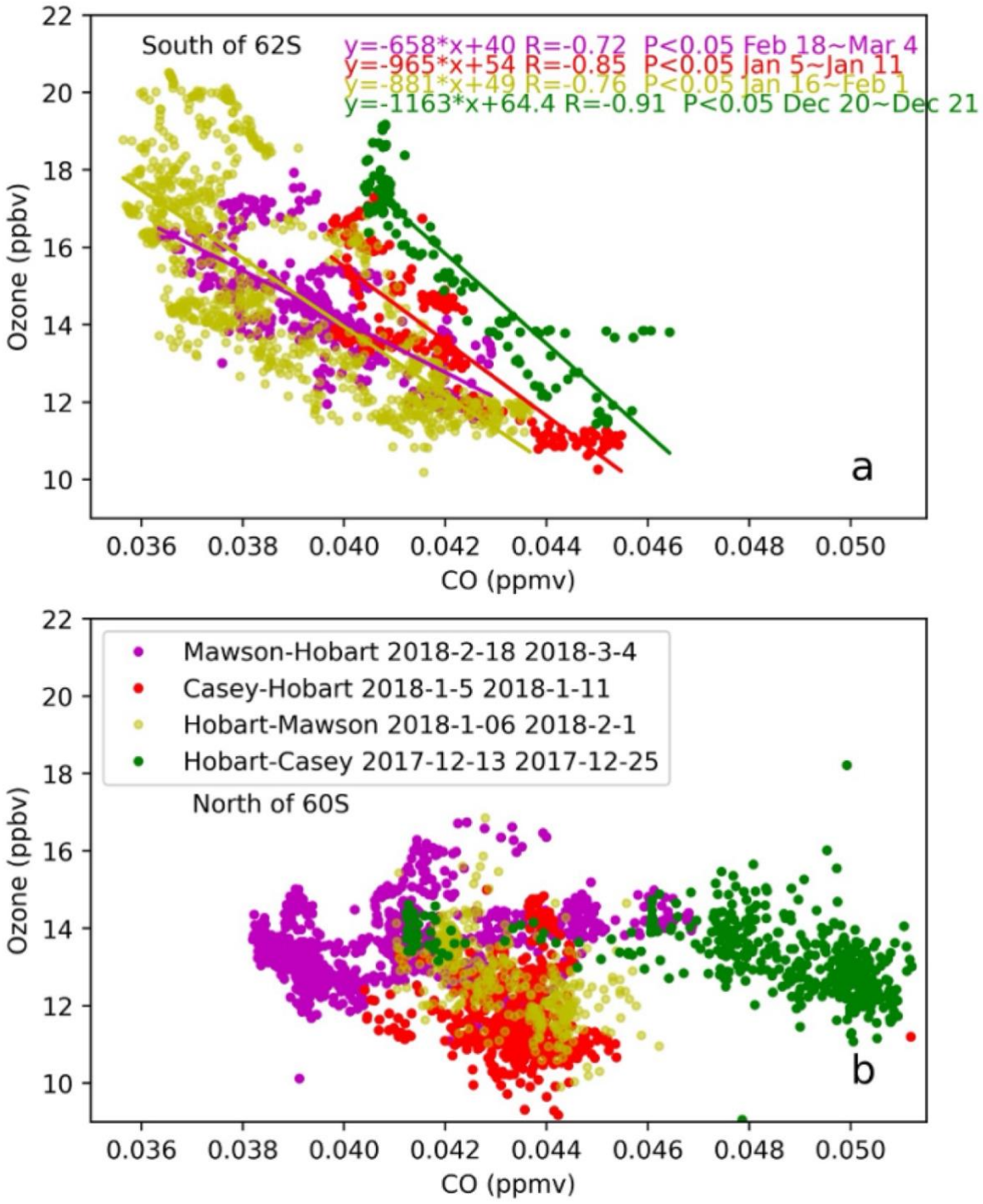

Figure 2.8 Ozone mixing ratio as a function of carbon monoxide (CO) mixing ratio during MARCUS voyages south of 62°S (SSO) (a) and between 45°S and 60°S (b), colored by voyage. Results of linear regressions and statistical significance tests are shown by the corresponding color only in (a), given that no similar significance is achieved using data in (b).

2.3.4. Aged and fresh aerosols

To further examine the air mass origin, Figure 2.8 shows the mixing ratio of CO and ozone after the quality control discussed in Niu et al. (2024) is performed, in which a machine learning algorithm is applied to identify time periods when the AA aerosol data are contaminated by the ship stack onboard the AA. Both the concentrations of CO below 0.05 parts per million by volume (ppmv) and the surface ozone range within 10-20 parts per billion by volume (ppbv) are typical values for stable, unpolluted conditions given a clean MBL background (Kanaya et al., 2019; Williams et al., 2019; Kok et al., 1998; Robinson et al., 1984). Figure 2.8 shows that the CO mixing ratio over the SSO is less compared to its further north, particularly during the voyage from Hobart to Mawson (in yellow) and from Hobart to Casey (in green). This is consistent with the previous observations of Robinson et al. (1984), which show the lowest values of surface observed CO, 35-45 ppbv, can be found near Antarctica. This poleward CO decline can be attributed to the absence of continental pollution and efficient atmospheric cleansing mechanisms. The surface ozone mixing ratios observed during the MARCUS are consistent with those presented by Kanaya et al. (2019), Parrish et al. (2014), and data from stations at Arrival Heights, Antarctica, New Zealand (77.83°S, 166.2°E), and Lauder, New Zealand (65.04°S, 169.68°E) (https://gml.noaa.gov/dv/iadv/graph.php?code=LAU&program=ozwv&type=vp). Although there are no available ozone vertical profiles from MARCUS, previous studies show that ozone over the SO increases with altitude, with 10-30 ppbv in the MBL, gradually increasing to above 30 ppbv at the MBL top (~1.5-2 km), then reaching 30-50 ppbv in the free troposphere (~2-8 km), exceeding

100 ppbv from upper troposphere to lower stratosphere and eventually reaching a concentration peak of 2-8 ppmv in the stratosphere (Bourgeois et al., 2020, Thompson et al. 2020, Johnson et al. 1990). Given climatically that ozone gradually increases with height while the source of the CO is primarily the surface layer, the higher concentrations of ozone between 45°S to 60°S compared to those over the SSO show that the air mass origins thus have higher altitudes over the SSO compared to further north, consistent with Figure 2.6 and 2.7.

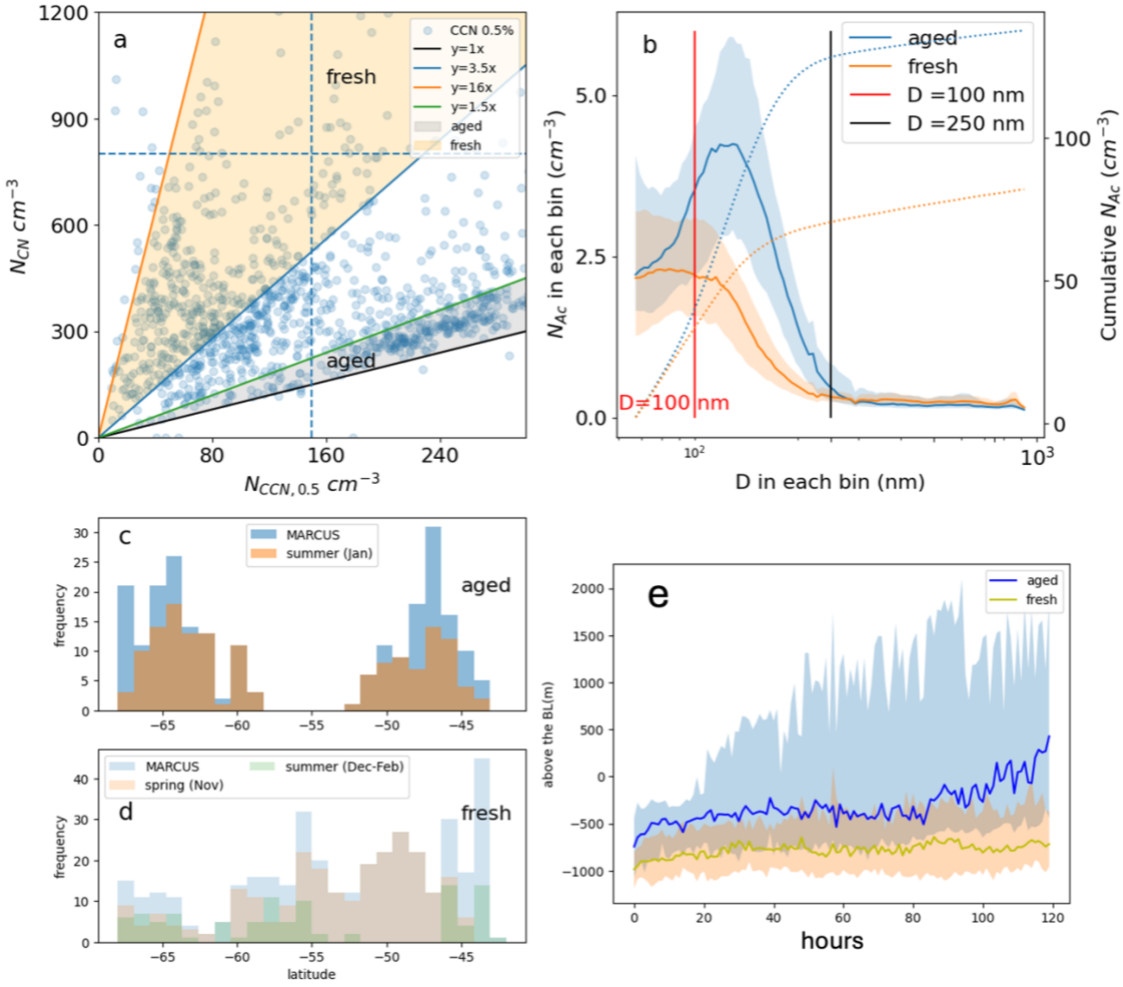

Figure 2.9 a) Scatter plot of the number concentration of total nuclei (N_{CN}) and CCN measured at 0.5% supersaturation ($N_{CCN,0.5}$) during MARCUS. The cluster "fresh" ("aged") refers to a sample

of air with a $3.5 < N_{CN} / N_{CCN} < 16$ ($N_{CN} / N_{CCN} < 1.6$). **b)** Number concentration of accumulation mode aerosols (N_{Ac}) in each bin for aerosols labeled as fresh and aged respectively in orange and blue, with the red and black reference lines indicating 100 nm and 250 nm for aerosol size. Dashed lines show the cumulative number concentration of Ac with the axis on the right. Histogram of the latitude of aged **(c)** and fresh **(d)** air masses sampled during all MARCUS cruises in blue and colored by season, with November (spring) in d and December – February (summer) in c (orange) and d (green). **e)** Difference between the air mass altitude and the MBLH as a function of the past 120 hours in e, for aged aerosols in blue and fresh aerosols in yellow. The shadings cover the 1st and 3rd quartiles, and the lines represent the median values for each cluster in each hour. The air mass altitude is determined from the ERA5 data at the location of the Hysplit4 back trajectories.

Figure 2.9 compares the origins, size distributions and locations of fresh and aged aerosols for the MARCUS cruises. Figure 2.9a shows that aerosols labeled as fresh have a high ratio (3.5-16) between N_{CN} and $N_{CCN,0.5}$. This is potentially caused by recent particle formation (RPF) and its related increased amount of N_{CN}. As the aerosol particles age, it is likely that they grow so that a higher portion of the Aitken mode aerosols grow into the accumulation mode and hence can serve as CCN, leading to a lower ratio between N_{CN} and $N_{CCN,0.5.}$ Figure 2.9b shows that the group of fresh aerosols has a peak between 60 nm and 100 nm, while the aged group of aerosols shows a mode of 100-200 nm, with a peak close to 150 nm. Both groups show less contribution of aerosols with $D > 250$ nm to the total number of Ac compared to aerosols with $D < 250$ nm. Figure 2.9c shows that most of the aged aerosols are acquired either south of 60°S or north of 52°S, mostly during the summer of 2018 January (orange color).

The fresh aerosols are also seen over a broader range of latitudes, with them occurring most frequently in 2017 spring (November) over the 45°S–60°S region, suggesting this is a prominent time and location for RPF events. Fresh aerosols are also seen during the summer (December-February 2018) but have less than 25% of the occurrence frequency compared with spring. This is counter intuitive in that summer has been identified as the time of rich biological activities and

frequent RPF events. Instead, the larger NCCN during the peak summer by the coast of Antarctica is related to the group of aged aerosols after aging. Figure 2.9e shows the height of the air mass above the boundary layer as a function of hour in the past 120-hour as determined from the HYSPLIT analysis. A positive value of "above the Boundary Layer (BL)" indicates the air mass is above the MBL, and a negative value indicates the aerosol is within the MBL. To connect with Figures 2.6 and 2.7, most of the air masses sampled over the NSO have traveled within the MBL. The group of fresh aerosols (in orange) in Figure 2.9e indicates mostly negative values in the past 5 days, consistent with presence inside the boundary layer. As Figure 2.7 showed that the low values of ozone shown in Figure 2.8. With Figure 2.9c and 2.9d showing the fresh aerosols are more frequent over NSO compared to SSO, consistency can be reached through Figure 2.6 – 2.9. The group of aged aerosols tend to have lower MBLH along the history (Figure S2.6), and most of the aged aerosols over the SSO origin from above the MBLH. Based on Figure 2.7, the air masses of aged aerosols spend a longer time over the MBL than within the MBL.

2.4. Conclusions

The analysis in this chapter builds upon the analysis presented in Niu et al. (2024) that showed the latitudinal variation of CCN size, hygroscopicity, and type. In this chapeter, the meteorological controls are analyzed to untangle the influence from large-scale dynamics, extratropical cyclones, and air mass histories. The following conclusions are achieved.

- The different patterns of CCN shown in Niu et al. (2024) are related to the CCN sources. The NSO for being within the Ferrel Cell is dominated by westerlies through spring to summer. The storms are more intense during the spring, leading to higher surface wind speed. The SSO for being within the Polar Cell has easterlies as prevailing wind, but the wind directions are within a broader range, and the wind is weaker compared to that over

the NSO. Most high winds over both NSO and SSO are associated with the approach of storm(s).

- Over the SO, the Marine Boundary Layer Height (MBLH) is linearly correlated with the surface wind speed, consistent with the dominance of turbulent mixing controlling the vertical development of the MBL. Thus, a higher MBLH is seen over the NSO compared to that over SSO given the higher wind speeds and more intense cyclones sampled during MARCUS over the NSO.

- Hysplit4 back trajectories show air masses sampled over the NSO traveled within the MBL for much of the 5 days before they were sampled, while the air masses sampled over the SSO traveled above the MBL for much of the previous 5 days. This is consistent with the ship-borne CO and ozone mixing ratio during MARCUS.

- The ratio between N_{CN} and N_{CCN} is used to label the aerosols as fresh and aged. A high N_{CN}/N_{CCN} ratio indicates recent particle formation, and a low value is indicative of aged aerosols. The group of aged aerosols have a mode of 150 nm in their size distributions in the accumulation mode size range and shows up more frequent over the SSO or between 45°S -50°S during the deep summer (2018 January). The RPF events, however, are more frequently identified over the NSO during the 2017 stormy spring (November). Latitudinally, the increased amount of N_{CCN} is found to be related to the increased number of aged aerosols. Instead of a smaller amount of total precipitation over the SSO compared to NSO (Humphries et al. 2021), this study shows that air mass travel above the MBL is closely related to the increased amount of secondary CCN by the coast of the Antarctic in the 2018 summer.

3. Comparisons of N_{CCN} between the CAM6 and MARCUS Observations

3.1. Introduction

Shortwave radiative fluxes calculated from recent versions of Earth System Models (ESMs) simulated clouds do not match those observed by satellites over the remote Southern Ocean (SO) (Fiddes, S. L. et al., 2022; Medeiros et al., 2023). The high positive bias over the Antarctic Plateau has been highlighted as one of the largest biases of shortwave solar radiation reaching the surface over the Southern Hemisphere, and in fact, globally (Mallet et al., 2023). Mace et al. (2023) illustrated natural Marine Cloud Brightening (MCB) over the Antarctic marginal ice zone using satellite retrievals over the summertime SO, demonstrating that most scenarios with higher cloud droplet number concentration show up over the Antarctic Plateau.

McCoy et al. (2020) pointed out that some ESMs underestimated the marine cloud droplet number concentration (N_d) over the summer SO by a factor of 2 compared to in-situ field measurements. Many models predict N_d based on the cloud supersaturation and availability of Cloud Condensation Nuclei (CCN). As such, an assessment of simulated CCN against observations acquired during field campaigns over the SO is necessary. In the Community Atmospheric Model 6 (CAM6), the activation of aerosol particles is represented using a parameterization (Abdul-Razzak and Ghan, 2000) based on Kohler theory (Köhler, H.,1936), which directly takes into consideration the effects of particle size, composition, and hygroscopicity of participating species on particle activation. Specifically, the simulated CCN can be assessed from two aspects: 1) the number concentration of accumulation mode aerosols (Ac), which have dry diameters between 0.07 and 1 um (Schwartz, 1996) and form the majority of CCN (Williams et al. 2002; IPCC, 2024);

and 2) the activation of these CCN-active Ac into cloud droplets, which can depend on aerosol type.

Sea spray aerosols that are generated by wind driven processes constituting sea salts with varying fractions of organics are a key aerosol type throughout the year over the SO (O'Dowd et al. 2007; Hudson et al., 2011; Quinn et al., 2014). This CCN type is hereafter referred to as SS-CCN (Sea Spray CCN). During the summer, the formation of secondary aerosols near the surface from biogenic gaseous emissions and gas to particle conversion also becomes a crucial SO aerosol type. In fact, the summertime SO is one of the most biologically active regions in the world (Ayers and Gras 1991; O'Dowd et al. 1997; Sim´o and Dachs 2002; Ayers and Cainey, 2007; McCoy et al. 2015; Fossum et al. 2018; Alroe et al. 2020), and Marine Biogenic CCN, hereafter MB-CCN, are reported to drive the strong seasonality of CCN over the SO (Sanchez et al., 2018; Humphries et al. 2022). The aerosol precursors of these CCN come from gas-to-particle conversion that occurs through dimethyl sulfide (DMS) to methanesulfonic acid (MSA) or hydroperoxymethyl thioformate (HPMTF), and then to sulfur dioxide vapor and ultimately to sulfate aerosols (Chen et al, 2018; Veres et al., 2020). Quinn et al. (2017) and McCoy et al. (2021) pointed out that entrainment of free tropospheric nucleated new particles into the Southern Hemisphere marine boundary layer (MBL) produces boundary layer Aitken mode aerosols, which can grow and serve as CCN near the surface.

Recently, new particle formation events were also observed within the pristine MBL (Zheng et al., 2021), which impact the surface CCN budget. Humphries et al. (2015) found that ultra-fine particles, defined as particles with D <100 nm, over the SO are linked to air masses arriving from the Antarctic as new particle formation and growth events occur over both the sea ice marginal

zone in the boundary layer and free troposphere over the Antarctic plateau (Lachlan-Cope et al. 2020). Mace et al. (2024) illustrated that N_d is high within katabatic air masses that descend from the Antarctic ice sheet but decrease with time as the air masses pass over the SO open water.

The sinks as well as sources of CCN are necessary for simulating the important aerosol-cloud-climate feedback over the SO region. Coalescence scavenging is regarded as the dominant sink of in cloud CCN and accumulation mode aerosols, which occurs when a cloud droplet forms in supersaturated conditions (Pruppacher and Klett, 1998; Wood, 2006; Mechem et al., 2006; Kang et al., 2022, McFarquhar, 2022). While the scavenged aerosols can fall out and reach the surface after raindrops form through collision-coalescence, some particles remain in the boundary layer as falling rain droplets evaporate. Wet removal/deposition is regarded as the dominant sink for SO surface CCN (Sanchez et al., 2021; Humphries et al., 2021; Alinejadtabrizi et al., 2024). Mace et al. (2024) illustrated a case during MARCUS using MERRA-2 reanalysis and Moderate Resolution Imaging Spectroradiometer (MODIS) derived N_d, showing the increase of snow precipitation rates matched the decrease of N_d.

The 2017–18 ship-based Measurements of Aerosols, Radiation, and Clouds over the Southern Ocean (MARCUS) field experiment included in-situ and remote sensing instruments for aerosols, clouds, precipitation, and radiation measurements (McFarquhar et al., 2021). Niu et al. (2024) characterized the latitudinal gradient of MBL CCN number concentration (N_{CCN}) and Ac size by comparing observations acquired over the north SO (NSO, 50°S-60°S) to those over the south SO (SSO, south of 62°S). They found that the SSO was associated with higher N_{CCN} and stronger seasonality compared to the NSO.

The observed N_{CCN} seasonality and aerosol size distributions over the SSO implied the potential existence of substantial sulfate CCN. In contrast, a larger contribution from primary sea spray aerosols was reported over the NSO (Humphries et al. 2015, 2021). Further, airborne measurements of substantial sulfate CCN in the lower troposphere over the SO were reported by Twohy et al. (2021), Sanchez et al. (2021), and McCoy et al. (2021) during the Southern Ocean Clouds, Radiation, Aerosol Transport Experimental Study (SOCRATES), conducted in the same Australasia sector of the SO in the 2018 summer over lower latitudes.

Lee et al. (2013) previously quantified the magnitude and causes of uncertainty of CCN in global models, showing that the dominant uncertainties in representing N_{CCN} in remote regions are aerosol microphysical processes including emissions close to sources, sulfate formation during cloud-processing, and aerosol deposition. An assessment of simulated Ac in CAM6 against SOCRATES observations highlighted a consistent low bias in CAM6 of particles with diameters between 70 and 800 nm between the surface and up to 5-km at latitudes between 45°S and 62°S (McCluskey et al., 2023). Additionally, it was reported that the simulated particles with 100 nm < D < 500 nm were dominated by sea salt aerosol, whereas observed particles of the same size were dominated by sulfate (McCluskey et al., 2023). However, most airborne data do not extend poleward of 62°S, leading to the remote SSO being rarely targeted for CCN simulation and observation comparison studies.

In this chapter, recent field observations are used to assess simulated CCN and aerosols over the SO. Observations over the coastal Antarctic provide insight into aerosol-cloud interactions in extreme pristine environments that have the lowest anthropogenic pollutants anywhere on Earth. Observations made during field campaigns (Section 3.2.1) are used to assess simulations

conducted with the CAM6 (Section 3.2.2), by examining 1) CCN concentrations (Section 3.3.1), 2) Ac size and composition (Section 3.3.2), and 3) hygroscopicity (Section 3.3.3). Sea ice condition is also analyzed to further interpret the bias of N_{CCN} (Section 3.3.4).

3.2. Methods

3.2.1. Observations

During MARCUS, the Australian icebreaker, Aurora Australis (AA), made three full latitudinal transects over the SO on resupply voyages from Hobart, Australia (42.9°S, 147.3°E) to the Australian Antarctic stations Casey (66.16 °S, 110.3°E), Davis (68.3° S, 77.6° E), and Mawson (67.4° S, 62.5°E). The nature of the resupply voyages meant that specific cloud or weather systems were not targeted so that the data collected are expected to be representative of cloud and aerosol conditions over the SO in general. Only three voyages between Antarctic stations are used in this study. Because effluents from the AA ship stack contaminated aerosols measurements much of the time, periods when ship stack contamination impacted the measurement of aerosols have been removed using the machine learning method of Niu et al. (2024), resulting in 26% data recovery.

The primary aerosol instruments used in the current analysis were the CCN-100 and Ultra High Sensitivity Aerosol Spectrometer (UHSAS), both manufactured by Droplet Measurement Technologies, Inc. and that were included on the DOE ARM Mobile Facility 2 (AMF2) Aerosol Observing System (Uin et al., 2019). For the CCN-100, an hourly cycle was adopted such that the supersaturation with respect to water (SS_w) was changed every 12 minutes, including 2 minutes for conditions to reach equilibrium and 10 minutes of 1 Hz observations at five different SS_w (0.1%, 0.2%, 0.5%, 0.8%, and 1.0% Uin et al., 2022). The UHSAS provided aerosol size distributions for particles with optical diameters of 60 nm < D < 1000 nm by measuring light scattered by particles passing through an infrared laser using optical detectors to determine diameter (D). Data were

reported with a time resolution of 10 seconds. For MARCUS, the first size bins (60 - 70 nm) were not used because of decreased counting efficiency and the last size bins (700 nm - 1000 nm) were not used to avoid artificial errors. The manufacturer specified the uncertainty of the CCN-100 and UHSAS as under 5% for number concentration during laboratory calibration (Uin et al., 2016 and 2019). There were dryers upstream of the UHSAS but not for the CCN-100, thus in this study measurements from UHSAS and CCN-100 are both displayed in this study (e.g. in Figure 3.4), but the hygroscopicity parameter cannot be derived and are not reported using the observations. During MARCUS the uncertainties were influenced by conditions such as ambient air pressure, instrument air flow, sea spray and plume contamination, and therefore can be higher than associated with the laboratory calibration.

The sea ice presence was acquired by manually labeling data from a camera set up onboard to monitor the sea state. The open water, scattered ice, and solid sea ice as shown in Figure S3.2, were respectively labeled as 0, 0.5, and 1. Although this sea ice fraction is qualitative, it does provide additional context for the sea-state, as demonstrated by the time series in Figure S3.3.

The precipitation intensity was assessed using the sky-pointing Marine W-Band (95 GHz) ARM Cloud Radar (WACR). Following Mace et al. (2021), a +4.5 dBZ correction factor was applied to measured reflectivity. The quality control of radar data was provided by the ARM Data Quality Office (https://doi.org/10.5439/1498736). Reflectivity below 1-km was used to represent surface conditions, and a 10-min average was applied to pair with the aerosol sampling.

3.2.2. Simulation

The simulation used in this chapter was conducted with the Community Atmosphere Model version 6 (CAM6, Bogenschutz et al., 2018). CAM6 is the atmospheric component of Version 2.1 of the Community Earth System Model (CESM2.1, publicly available at

http://www.cesm.ucar.edu/models/cesm2.1/). CAM6 incorporates a two-moment cloud microphysics scheme for four hydrometeor classes (liquid, ice, rain, and snow), following Morrison-Gettelman MG2 scheme (Gettelman & Morrison, 2015). CAM6 also uses the Cloud Layers Unified by Bi-normals (CLUBB, Golaz et al., 2002; Larson and Golaz, 2005) parameterization for the planetary boundary layer, shallow convection, and cloud macrophysics. CAM6 retains the deep convection scheme of Zhang and McFarlane (1995) that was used in CAM5. The precipitation from the CLUBB and deep convection schemes is referred to as large-scale (stratiform) and convective precipitation, respectively. In the CAM6 configuration used in this study, sea ice was based on the monthly mean climatology from the Community Ice CodE (CICE5, Hunke et al., 2015), and sea ice fraction is used as the primary variable to describe the model sea ice coverage. The observed sea ice acquired from manually labeling and simulated sea ice from CAM6 are shown for comparison, and manually labeled sea ice fraction estimates qualitatively agreed with the emulated sea ice fraction over 70% of the time (Figure S3.3).

Aerosols in CAM6 are predicted by a four-mode version of the Modal Aerosol Module (MAM4) (Liu et al., 2016), initialized based on climatological profiles in 2000 from the CMIP6 emissions inventory (Feng et al., 2020). MAM4 represents the aerosol size distribution using four lognormal modes: Aitken mode (20-80 nm), accumulation mode (80 nm -1 um), coarse mode (1-10 um), and insoluble primary carbon accumulation mode (80 nm -1 um). Each mode's lognormal size distribution is defined by its prognostic aerosol number and mass mixing ratios and a fixed geometric standard deviation (σ_g). Each species (sea salt, sulfate, secondary organic aerosol, primary organic aerosol, black carbon, and mineral dust) is also characterized by its optical properties, density, and hygroscopicity. Details are summarized in supporting information (SI) Table S3.1. The activation of aerosols into cloud droplets in CAM6 is diagnosed as a function of

the modeled sub-grid scale updraft velocity and aerosol composition and size distribution (Abdul-Razzak & Ghan, 2000). Simple gas-phase chemistry is included for secondary aerosols such as sulfate. This includes (1) DMS oxidation with OH and NO_3 to form SO_2; (2) SO_2 oxidation with OH to form H_2SO_4 (gas); (3) H_2SO_2 production (HO_2 + HO_2); and (4) H_2O_2 loss (photolysis and H_2O_2 + OH). The rate coefficients for these reactions are provided from the MOZART model (Emmons, L.K., et al. (2010)).

For aerosol size distributions, only aerosols with 70 < D < 700 nm are available as measured by the UHSAS. The model data are thus truncated to be comparable with observations. The truncated number concentrations were calculated using

$$\mathrm{N(Dmin, Dmax)} = \frac{N_0}{2}\left[\mathrm{erf}\left(\frac{\ln(D_{max}/\widehat{\mathrm{Dn}})}{\sqrt{2}\ln\sigma_g}\right) - \mathrm{erf}\left(\frac{\ln(D_{\min}/\widehat{\mathrm{Dn}})}{\sqrt{2}\ln\sigma_g}\right)\right] \quad , (1)$$

where erf is the Gauss Error Function, N_0 is the total number concentration, $D_{\min}$ and D_{max} are the lower and upper detection limits for aerosol instruments, σ_g is the fixed geometric standard deviation, and $\widehat{\mathrm{Dn}}$ is the median diameter. Mass concentrations are calculated using

$$\mathrm{M(Dmin, Dmax)} = \frac{M_0}{2}\left[\mathrm{erf}\left(\frac{\ln(D_{max}/\widehat{\mathrm{Dv}})}{\sqrt{2}\ln\sigma_g}\right) - \mathrm{erf}\left(\frac{\ln(D_{\min}/\widehat{\mathrm{Dv}})}{\sqrt{2}\ln\sigma_g}\right)\right] \quad , (2)$$

where $\widehat{Dv}$ is the volume median diameter and can be represented using $\widehat{Dn} = \widehat{\mathrm{Dv}}\exp(3\ln\sigma_g)$ (Zender et al., 2010). Comparisons of observed and modeled number concentrations are quantified by the modified normalized mean bias (B_n) and fractional gross error (E_f) as expressed by $B_n = \frac{2}{N}\sum\frac{f_i - O_i}{f_i + O_i}$, $E_f = \frac{2}{N}\sum\left|\frac{f_i - O_i}{f_i + O_i}\right|$, where B_n describes the mean fractional difference between the modeled estimates (f) and observations (O), and E_f measures the model absolute error.

The CAM6 analytic radar reflectivity is calculated using the CloudSat simulator within the Cloud Feedback Model Intercomparison Project Observation Simulator Package (COSP, Bodas-Salcedo et al., 2011), which provides synthetic radar reflectivity at a frequency of 94 GHz for comparison with the observed W-band reflectivity.

The CAM6 simulation was performed with specified dynamics for surface temperature and winds (i.e., nudging) to Modern ERA-retrospective Analysis for Research and Applications (MERRA-2) reanalysis with a 24-hour relaxation timescale, following the model setup of Gettelman et al. (2020). A finite-volume dynamical core of 0.9° longitude × 1.25° latitude resolution was used with 32 vertical levels and a model time step of 30 min. The model output was written to disk every 10 minutes.

For co-located comparisons of model output against observations, the 1-min averaged ship track was used to determine the geographic location of the ice breaker at a given time. The closest grid cell and the closest time steps were used in each interpolation to obtain a singular value at the ship location at a given time within a voyage. Simulated meteorological conditions including temperatures and winds were compared with in-situ observations, and general consistency was seen as shown in Figure 3.1.

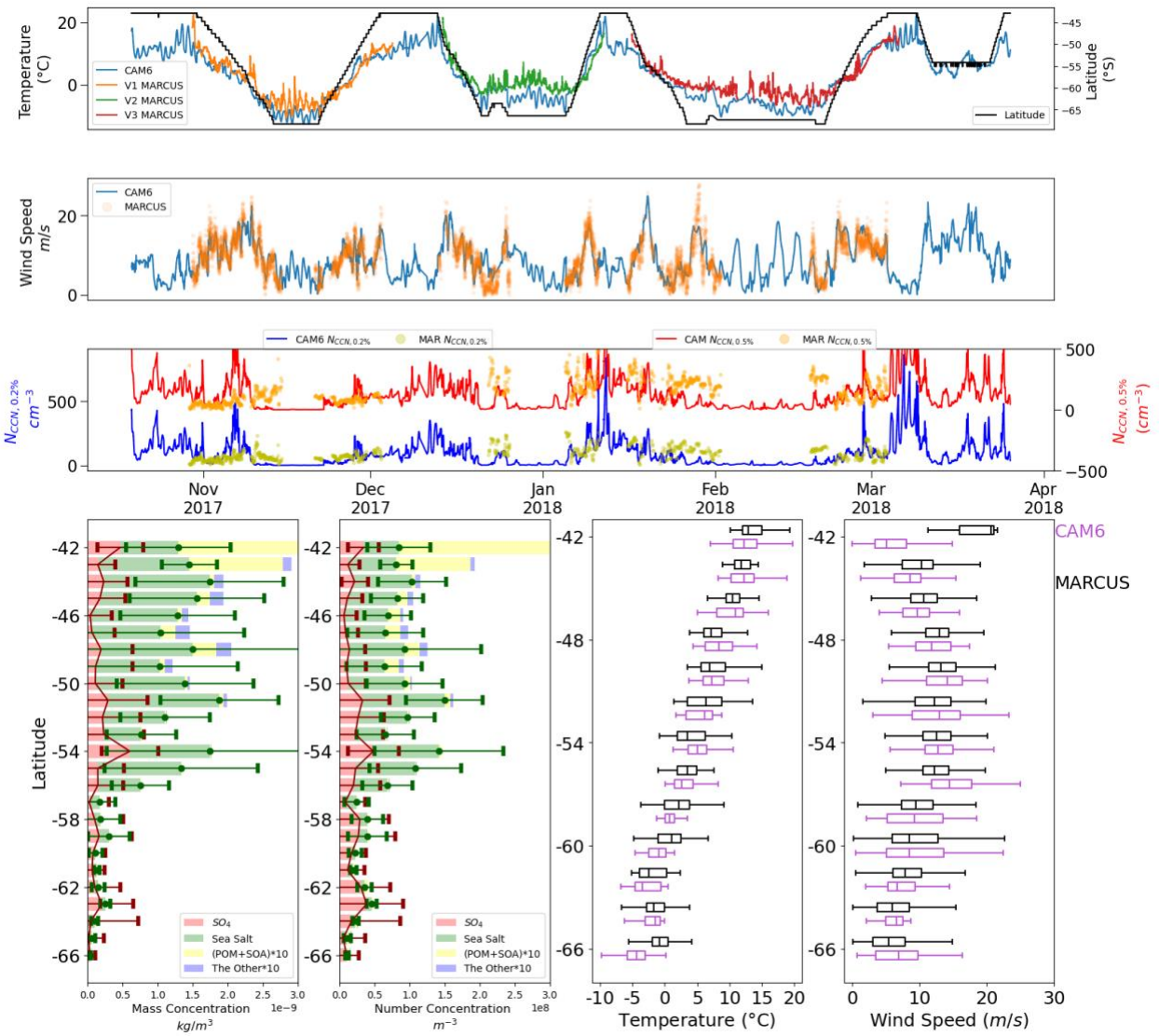

Figure 3.1 Time series of air temperature (a), surface wind speed (b), N_{CCN} measured at 0.2% (blue) and 0.5% (red) SS_W (c) with lines for CAM6 simulations and scatter points for MARCUS voyages. Latitudinal dependence of simulated Ac chemical composition by mass (d) and by number (e). The bar charts (d, e) have whiskers of sea salt and sulfates for one standard deviation, with red lines connecting the mean of sulfates in each 1-degree latitude bin. The whiskers extend from the box to the farthest data point, lying within 1.5 times of the inter-quartile range in each 2-degree latitude bin. POM stands for primary organic matter, SOA for secondary organic aerosols, and "the other" includes dust and black carbon, POM+SOA, and "other" are all multiplied by 10 in (d, e). Time series of latitudes in black in (a). Latitudinal dependence of air temperature (f), and surface wind speed (g) with simulations in purple and observations in black. Observations are from the CCN-100 and Aerosol Observing System Surface Meteorology onboard.

3.3. Results

3.3.1. Assessing the bias of N_{CCN} in CAM6 against MARCUS

Figure 3.1f and 3.1g show that the nudged simulation reproduces the observed winds and temperature. Statistically, simulated temperature is significantly correlated with observed temperatures with R^2 of 0.69 and RMSE (Root Mean Square Error) of 2.61°. Simulated wind speed is significantly correlated with observed wind speed with R^2 of 0.68 and RMSE of 3.43 ms^{-1}. This indicates that the main variables driving the local sea spray aerosol emissions are consistent with the conditions when the observations were made. The surface temperature at the highest latitudes simulated in CAM6 has a standard deviation of 2.5° C, which is larger compared to that over the other latitudes. This is likely due to variability in sea ice coverage at the Antarctic Plateau. Figure 3.1g shows that both model and observations have the highest wind speeds between 48°S -56°S, and the lowest wind speeds south of 60°S, consistent with Humphries et al. (2021).

Figure 3.1c illustrates that the consistency between modeled and observed N_{CCN} is much less compared to that of both temperature and surface wind speed. At the start of November, CAM6 overestimated the N_{CCN} by up to +400%. But in December, the observed N_{CCN} shows higher peak values than those from the CAM6 by up to +60%, and similarly for the end of January and sometimes for the middle of February. These N_{CCN} biases identified on the time series are quantified as a function of latitude in Figure 3.2. Figures. 3.1d and 3.1e show that most simulated Ac with 70 nm< D < 700 nm is dominated by sea salt north of 56°S by both number and mass, consistent with the higher wind speeds as those latitudes shown in Figure 3.1g.

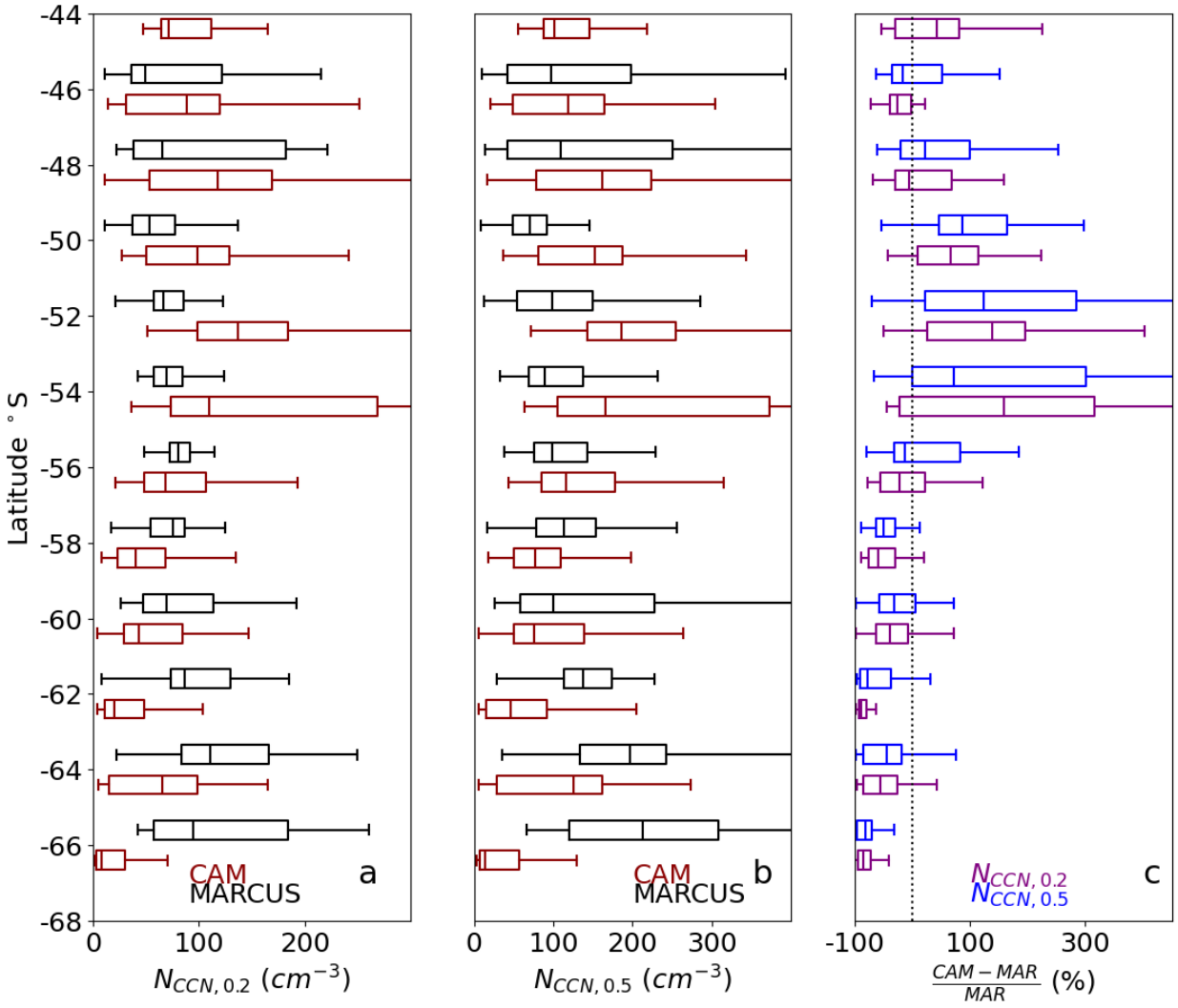

Figure 3.2 Latitudinal dependence of N_{CCN} measured at SS_W 0.2% (a) and 0.5% (b), with observations in black and simulation in red, and the calculated relative biases (c). The dashed line on (c) represents the scenario where simulations and observations perfectly agree (a bias of zero). The whiskers extend from the box to the farthest data point, lying within 1.5 times of the inter-quartile range in each one-degree latitude bin.

Recent aircraft-based cloud droplet number concentration and below cloud CCN measurements over the Australasian sector of the SO suggest that the typical maximum SSw reached in clouds over the SO is about 0.3% (Sanchez et al., 2021; Twohy et al., 2021). Thus, CCN observations measured during MARCUS at 0.2% and 0.5% supersaturation ($N_{CCN,\,0.2}$ and $N_{CCN,\,0.5}$) are examined to give maximum insight about how aerosols affect clouds. $N_{CCN,\,0.2}$ and $N_{CCN,\,0.5}$ over

the SO vary from (minimum – maximum), 89-181 and 90-298 cm^{-3} respectively (Figure 4 in Niu et al., 2024).

A comparison between the observed and simulated CCN number concentrations as a function of latitude is provided in Figure 3.2. In general, the N_{CCN} is overestimated over 50°S -54°S but shows relative agreement with the simulation over 44°S-48°S. Both the sign and magnitude of the bias of $N_{CCN, 0.2}$ and $N_{CCN, 0.5}$ vary greatly north of 55°S, including positive median relative biases of larger than +100% between 52°S-54°S and negative median relative biases between 46°S-47°S. Whiskers over latitudes north of 55°S are longer compared to further south, implying larger variations in each latitude degree. For the area south of 56°S, both modeled $N_{CCN, 0.2}$ and $N_{CCN, 0.5}$ are consistently underestimated, sometimes with the relative bias as large as -100%. This underestimation of N_{CCN} in CAM6 could be caused by 1) missing sources, including a lack of primary marine organic aerosols (Zhao et al., 2021); mis-representation of sea salts, new/recent particle formation (NPF) from marine gaseous precursors, and other local and transported aerosol types and 2) the overestimation of aerosol sinks such as wet scavenging, or 3) a combination of the above reasons.

Many recent studies (e.g. Sanchez et al., 2021; Humphries et al., 2021, Alinejadtabrizi et al., 2024, Mace et al., 2024) emphasize that wet scavenging plays a significant role in N_{CCN}. To investigate the potential influence of precipitation, Figure 3.3 illustrates that model bias is not exclusively associated with the presence or absence of precipitation. Figures 3.3c and 3.3d compare $N_{CCN, 0.2}$ and $N_{CCN, 0.5}$ from the CAM6 and MARCUS for time periods when there was no precipitation at the surface from both the models and observations. No precipitation is defined as times with 1) surface-1-km vertical mean reflectivity diagnosed using the CAM6 output smaller than -20 dBz,

and 2) the vertical-mean of the lowest five detectable layers from the WACR observations is less than -20 dBZ.

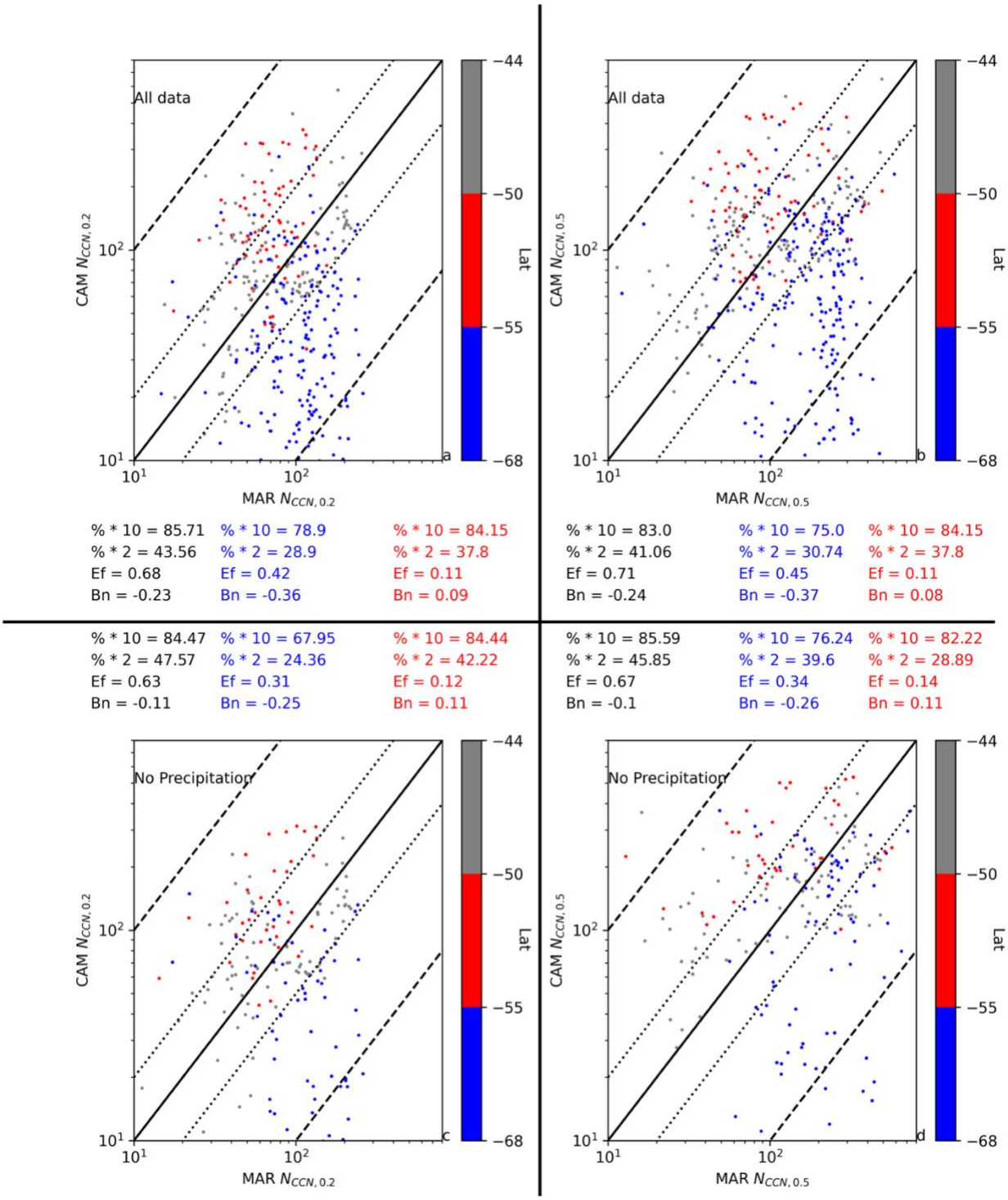

Figure 3.3 Scatter plot of simulated-observed N_{CCN} measured at 0.2% (a, c), 0.5% (b, d) SS_w during the whole MARCUS period (a, b), and that during no-precipitation (c, d), defined as both ship-borne 94 GHz radar and model diagnosed reflectivity < -20 dBz, with the marker color indicating latitude. In each panel, the black solid line corresponds to the 1:1 line and the modified normalized mean bias (B_n), fractional gross error (E_f), and percentage of total points within a factor of 2 (dotted lines) and a factor of 10 (dotted and dashed lines) are listed. The B_n in blue and red respectively refers to the values south of 55°S and between 50-55°S, and the black notes results over all MARCUS latitudes.

Figure 3.3 shows that the simulated N_{CCN} are biased compared with the MARCUS observations, with >50% biased by more than a factor of 2, and ~15% of them by more than a factor of 10. In addition, the simulated N_{CCN} does not capture the strong latitudinal gradient of observed N_{CCN} shown in Figure 2 with both Niu et al. (2024) and Humphries et al. (2021) also previously illustrating an increase in N_{CCN} over the SSO. To reduce the influence from the Australian continent on observations, including anthropogenic pollutants from Hobart, biases over 50°S – 55°S and 55°S – 60°S are exclusively noted in red and blue in Figure 3.3.

Figure 3.3 illustrates that in the absence of precipitation, CCN are overestimated between 50°S and 55°S by CAM6, with a normalized mean bias B_n of +11% for both $N_{CCN,\,0.2}$ and $N_{CCN,\,0.5}$. The N_{CCN} are underestimated south of 55°S, with a normalized mean bias B_n of -25% for $N_{CCN,\,0.2}$ and -26% for $N_{CCN,\,0.5}$. Biases are also clustered using methods in Niu et al. (2024) in Supporting Figure S3.4, showing that B_n between 50°S and 62°S is only 1% and 3% for $N_{CCN,\,0.2}$ and $N_{CCN,\,0.5}$. This can be caused by the offset of positive biases north of 55°S and negatives biases further south. Nevertheless, both $N_{CCN,\,0.2}$ and $N_{CCN,\,0.5}$ have a consistent negative B_n, -36% and -42% respectively over the SSO (62°S -68°S). And this underestimation of N_{CCN} close to the Antarctic is consistent in both Figure 3.3 and Figure S3.2, for both 0.2% and 0.5% SS_w, with and without precipitation.

This negative bias close to the Antarctic Plateau during the non-precipitating scenarios motivates the use of available observations of aerosol size distributions, aerosol chemical composition, and

CCN hygroscopicity to better understand the source of the high N_{CCN} bias over the NSO and low N_{CCN} bias over SSO.

3.3.2. Size distributions

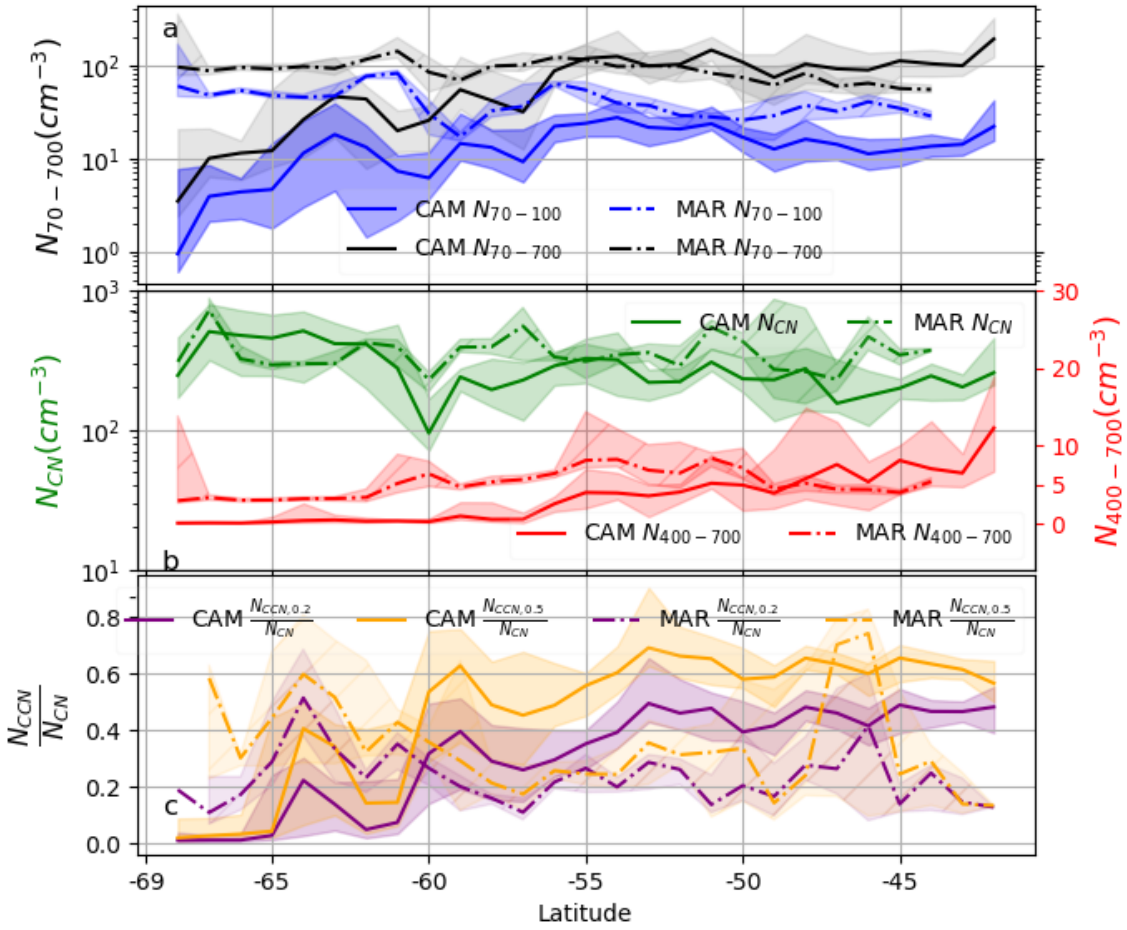

Figure 3.4 Number concentrations of Ac with diameters between 70-100 nm (small Ac, blue), 70-700 nm (Ac, black), 400-700 nm (large Ac, red), and 10-3000 nm (total Condensation Nuclei (CN), green) with lines connecting median values in each 1° latitude bin. Observed Ac number concentration determined using the UHSAS from the first three voyages of MARCUS (dashed lines) and from equivalent times and locations for simulated small Ac by the CAM6 (solid lines) in a) and for large Ac in b). Latitudinal dependence of ratio between N_{CCN} measured by CCN-100 at 0.2% and 0.5% supersaturation, and total condensation nuclei (N_{CN}) with 10 nm < D < 3000 nm as measured by condensation particle counter, shown in purple and yellow respectively in c) for simulations (solid) and observations (dashed line). All shadows represent ranges between the 1st and 3rd quartile.

In general, Ac do not sediment quickly nor coagulate easily and thus have long enough lifetimes to be capable of serving as CCN in the atmosphere (Williams et al., 2002). The simulated $N_{70\text{-}700}$ (black line) overlaps with the observed $N_{70\text{-}700}$ (black dash line) north of 55°S but separates apart further south. As Figure 3.4a and 3.4b show that the observed $N_{70\text{-}100}$ is 47-81% of N_{CCN} and $N_{400\text{-}700}$ is only ~ 5% of N_{CCN}, this suggests the CCN are dominated by the small Ac with 70 nm < D < 100 nm. This is reasonable from the Kelvin-Kohler-Junge theory (Köhler, H.,1936) given the typical maximum SS_w reached in clouds over the SO is about 0.3%. Further, the small Ac dominates the number of total Ac and increases poleward (blue dashed line), while the large Ac with 400 nm < D < 700 nm decreases poleward (red dashed line), both at a significance level of 0.05. Though both small and large Ac are underestimated in the simulation, the underestimation of small Ac ($N_{70\text{-}100}$) mostly influences the biased N_{CCN} south of 55°S. For 85% of the time, the simulated $N_{70\text{-}100}$ (blue solid line) are under 20 cm^{-3} while all of the observed $N_{70\text{-}100}$ are greater than 20 cm^{-3}. At the furthest southern latitudes (66°S-68°S), Figure 3.4a shows the relative bias of $N_{70\text{-}100}$ is as large as -89%.

Given enhanced SS_w, Aitken mode aerosols can also be activated into CCN (Kaufman & Tanré, 1994). The simulated N_{CN} are also shown in Figure 3.4b. Figure S10 in the supporting information also illustrates the relative bias of N_{CN} as a function of latitude. Figure S3.11 and S3.12 respectively extend the Figure 3.4 by clustering the data acquired in November and February. Overall, the absolute value of the N_{CN} relative bias is less than that of N_{CCN}, with underestimation of N_{CN} over the NSO 64% of the time, implying potential high biases in processes such as vapor condensation, coagulation, and cloud processing.

Figure 3.4c shows that the CCN activation ratios, at both 0.2% and 0.5% SS_w, are 15-45% higher over the SSO than over the NSO (except for the 46-47°S bins). The average ratio of $N_{CCN,\,0.4}/N_{CN}$ was previously reported to be 0.34 off Tasmania during summer (Andreae 2009). Further, Humphries et al. (2021) reported median ratios of $N_{CCN,\,0.2}/N_{CN}$ ($N_{CCN,\,0.5}/N_{CN}$) of 0.65 (0.81) over the summer SSO with an increase of activation ratio poleward. However, the CAM6 simulations show a reversed pattern with a higher CCN activation ratio over the NSO. A CCN activation ratio close to one implies that most aerosols in the measured size range are activated given the supersaturation in the CCN-100, while a small CCN activation ratio implies only specific aerosols with larger sizes and higher hygroscopicity are activated. Thus, CAM6 over-activated aerosols as CCN over the NSO and under-activated aerosols over the SSO compared to observations.

For CAM6, the bias of N_{CCN}/N_{CN} can come from either the numerator or denominator or both. The overestimation of the activation ratio over the NSO in Figure 3.4b is consistent with the underestimation of N_{CN} over the NSO in Figure 3.4c. The underestimation of N_{CCN}/N_{CN} over the SSO is consistent with the underestimation of N_{CCN} over the SSO. Whether a CN serves as CCN is related to its size and composition. Within the context of the SO, there are two primary sources: the production of sea spray aerosol through bubble bursting to produce film and jet drops, and the emission of gases that condense to produce secondary marine aerosol. For the sea spray emission compounds, most sea salt CCN are large (dry diameter >1 μm) while sulfate particles mostly have Dp <0.5 μm (Russell et al. 2023). Given the dominant source of sulfate aerosols south of 55°S. The underestimation of N_{CCN} south of 55°S is most likely related to the underestimation of small

particles (both $N_{70\text{-}100}$ and Aitken mode aerosols). However, biases from, for example, parameterizations of aerosols using MAM4 cannot be excluded.

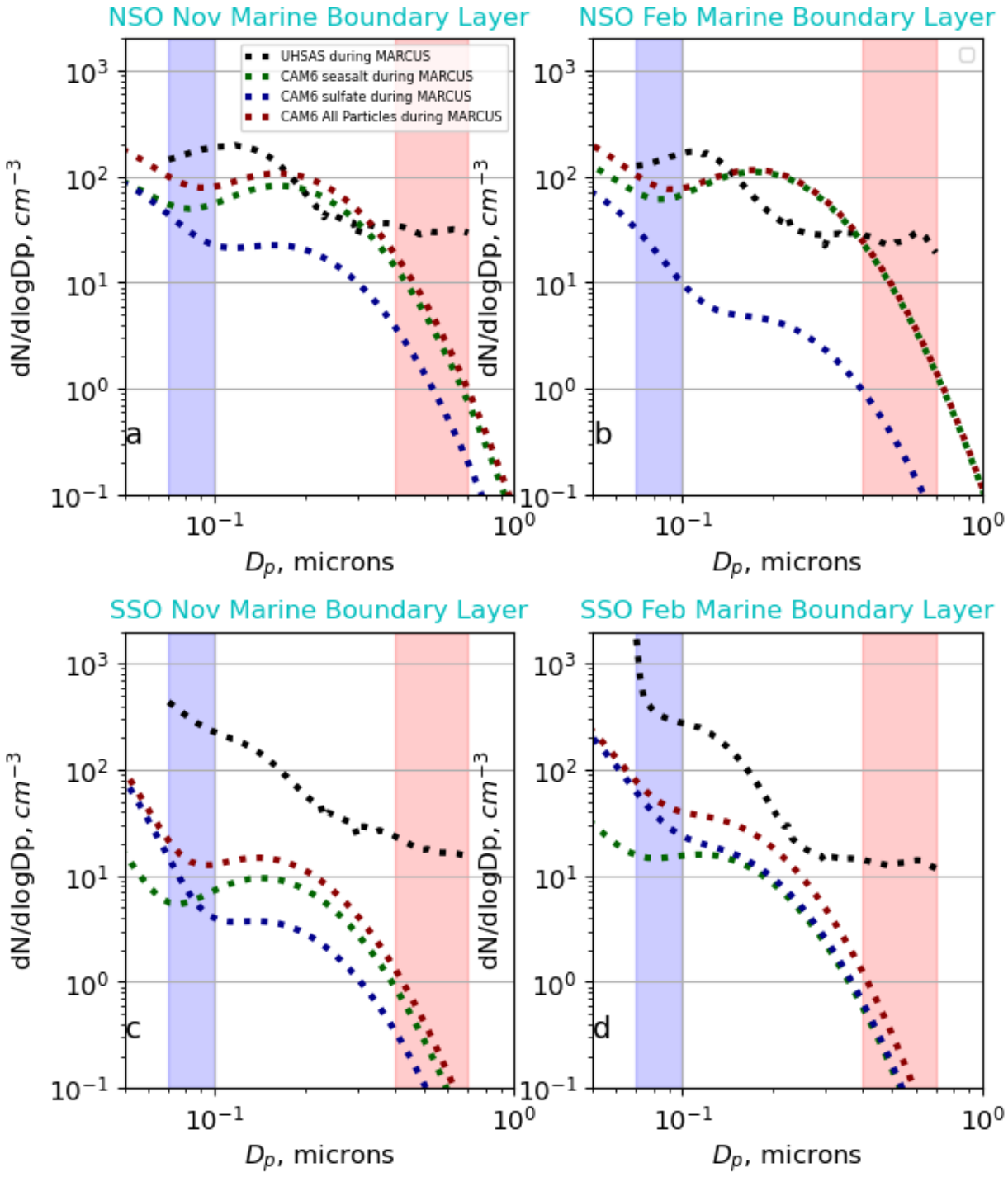

Figure 3.5 For time periods with no precipitation during MARCUS, average particle size distribution measured by the UHSAS (70 nm < D< 700 nm) in black, simulated from the CAM6 in red, and from CAM6 calculated sea salt particles in green and sulfates in blue over the NSO (a and b) and SSO (c and d) during 2017 November (a and c) and 2018 February (b and d). Shading illustrates particles with 70 nm < Dp < 100 nm (in blue) and with 400 nm < Dp < 700 nm (in red).

Figure 3.5 shows that for the non-precipitating scenarios, $N_{70\text{-}100}$ is in general underestimated by close to one order of magnitude over the SSO. Further, $N_{400\text{-}700}$ is underestimated by close to 2 orders of magnitude over the SSO. Except for the overall underestimation of the number concentration, the shapes of the simulated and observed aerosol size distributions also differ from each other. The underestimate of $N_{<150nm}$ over the SSO is significant for both November and February, which is highly related to the underestimation of Aitken-mode sulfate. Figure 3.5a and Figure 3.5b show the overestimation of middle size Ac (200 nm < Dp < 300-400 nm) concentration and underestimation of smaller size Ac (Dp < 150 nm) concentration are consistent over the NSO between seasons, with the former related to overestimation of sea salts. Another way to investigate the biases of N_{CCN} is from the perspective of the CCN-SS_w spectra which provides information about the hygroscopicity as discussed in the next section.

3.3.3. Hygroscopicity

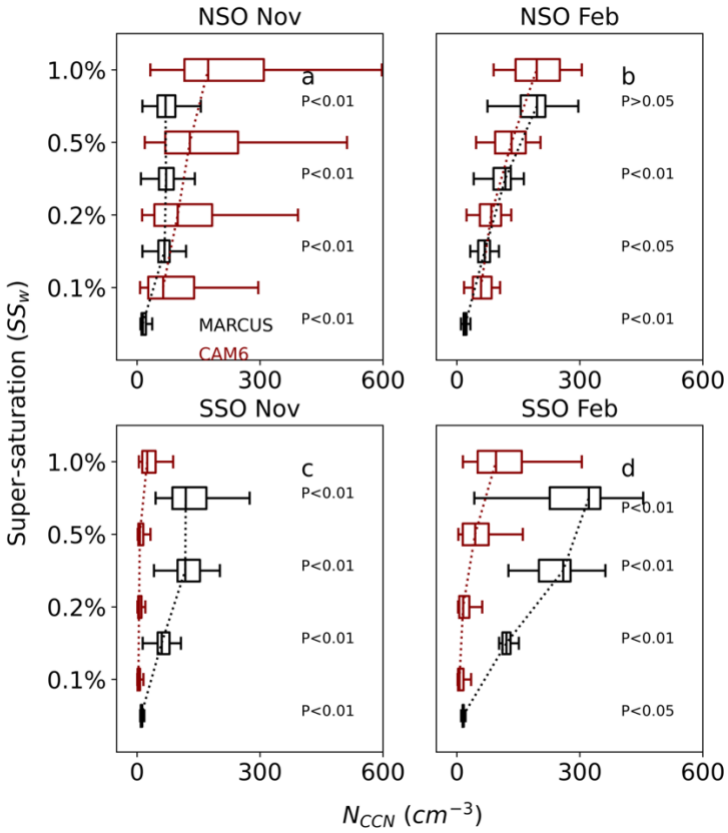

Figure 3.6 N_{CCN} as a function of SS_w (N_{CCN} - SS_w spectra) over the NSO (50°S -60°S, a and b) and SSO (south of 62°S, c and d) during November 2017 (a and c) and February 2018 (b and d) from CAM6 in red and MARCUS in black. Black and red dashed lines connect the median values of observed and simulated N_{CCN}. The P values are results from Welch's t-test for different mean values between the two datasets at each SS_w.

The box plots in Figure 3.6 indicate the concentration of CCN at a given SS_w, and thus long whiskers refer to large variations. The significance of different mean values from CAM6 and MARCUS is determined from Welch's t-test, which compares two data sets having different variances and different sample numbers. The P values show that except for the 1.0% SS_w in Figure 3.6b, CAM6 and MARCUS N_{CCN} show statistically different mean values.

In addition to a relationship with aerosol size distribution, the CCN spectra is related to the hygroscopicity of aerosols and provides indirect information about the bulk aerosol chemical composition. Hygroscopic sodium chloride particles are known to be highly-CCN-active and activate as CCN even under low SS_w of 0.1% and 0.2% (Ghan et al., 1998, Quinn et al., 2017). In CAM6, a hygroscopicity parameter, κ, of 1.16 is used to represent the general sea salt aerosols. Species like non-sea-salt sulfides (κ = 0.507), and secondary organic matter (κ = 0.14), are less hygroscopic and therefore require higher SS_w to activate as CCN (Petters and Kreidenweis, 2007, Xu et al., 2022). Here, the relationship between N_{CCN} and SS_w is used to infer the seasonal variability in CCN type and aerosol hygroscopicity. Figure 3.6 shows N_{CCN} as a function of SS_w (N_{CCN} - SS_w spectra hereafter) over the SO (50°S-68°S) with 0.1% the least favorable SS_w and 1.0% the most favorable for activation of aerosols into cloud droplets.

Median values of observed N_{CCN} in Figure 3.6a are nearly constant when $SS_w > 0.2\%$, showing most CCN are activated at SS_w of 0.2% or less over the NSO in 2017 November, suggesting the aerosols are very hygroscopic and potentially contain greater fractions of sea salts compared to the other cases in Figure 3.6. Comparing the simulated and observed shape of N_{CCN} - SS_w spectra in November (Figure 3.6a) and February (Figure 3.6b) suggests the CCN hygroscopicity is underestimated and decently captured, respectively. Over the NSO in November (samples acquired during Nov 5^{th} - 9^{th} and 25^{th} -29^{th}), the overestimation of N_{CCN} is associated with elevated simulated sea salt mass and number concentrations (Figure S3.6 and S3.7). A possible reason for the sea salt number concentration bias is the parameterizations used in the model. CAM6 emits sea salts using a power-law relationship of $U^{3.41}$ to describe the surface source, where U is the horizontal wind speed 10 m above the surface. Recently Hartery et al. (2020) found that the source followed a $U^{2.8}$

dependence by comparing the predicted sea spray concentration with SO in-situ SOCRATES measurements. Kang et al. (2022) utilized this new power law and accomplished cloud droplets budget closure, showing a mean difference between predicted and observed cloud droplet numbers using $U^{3.41}$ and $U^{2.8}$ were respectively 122 cm^{-3} and 5 cm^{-3}. Thus, the parameterization of sea salt emission can be location-dependent, and the use of $U^{3.41}$ could be overestimating the sea spray CCN over the SO. The long whiskers in Figure 3.6a compared to Figure 3.6b may also be related to the highly varying surface precipitation intensity shown by red lines in Figures S3.6 and S3.7 compared to S3.8.

In contrast, the activation of observed CCN over the SSO in February 2018 (Figure 3.6d) strongly depends on SS_w, implying that the aerosols are less hygroscopic, potentially related to the presence of substantial small sulfates. But the simulated CCN exhibits little dependence on SS_w (Figure 3.6c and 3.6d) compared to the observations, illustrating that except the number concentration is underestimated; the model may also overestimate the hygroscopicity. This shows that the CAM6 is not capturing the correct aerosol type and chemical composition over the SSO. McCoy et al. (2015) and Schmale et al. (2019) previously showed that aerosol composition over the SSO is dominated by sulfur-based particles, whose relative contribution to aerosol mass is around 60-70% at lower latitudes but increases to over 80% at more southerly latitudes. A similar trend was found by Humphries et al. (2021) (their Figure 3 and Figure A8) using data from the Clouds, Aerosols, Precipitation, Radiation, and atmospheric Composition over the southeRn oceaN 2 (CAPRICORN2) field campaign, which happened in 2018 over the similar region of SO as MARCUS. Since CAM6 has a hygroscopicity of 1.16 for sea salt and 0.507 for sulfate, this implies

the low bias in simulated N_{CCN} is associated with too little sulfate mass that leads to an overestimate of aerosol hygroscopicity by CAM6.

Considering the activation of aerosols highly depends on the supersaturation, the impact of hygroscopicity on the critical supersaturation at which aerosols are nucleated is also investigated. The multi type aerosols activation module in CAM6 is based on Abdul Razzak et al. (2000). Their Equation (9) shows $S_{mi} = \frac{2}{\sqrt{B_i}}(\frac{A}{3a_{mi}})^{3/2}$, where S_{mi} is the critical supersaturation for activating particles with radius equal to the mode radius a_{mi} and B_i is the hygroscopicity parameter used to treat the internal mixture of aerosol material for each mode i.

Over the SSO in February, for accumulation mode aerosols, overestimation of both B_i and the mode radius (a_{mi}) (the former is because $B_{sea\ salt}$ is larger than $B_{sulfate,}$ and the latter is related to the biased size distribution shown by Figure 3.5) lead to an underestimation of critical supersaturation. A smaller S_{mi} would lead to quicker nucleation of cloud droplets, but the number concentration of cloud droplets (N_d) over the SO in Feb is reduced because of the underestimated $N_{70\text{-}100}$.

Figures 3.1e and 3.1d illustrate the CAM6 simulated number and mass concentration by chemical composition for Ac with 70 nm < D < 700 nm respectively for the duration of the MARCUS campaign (November-March). For both Figure 3.1e and Figure 3.1d, the top two chemical aerosol types are sea salt and sulfate for both number and mass concentration in CAM6. The other aerosol types, such as organic aerosol ("POM+SOA"), and dust and black carbon ("the other") in Figure

1e, are multiplied by 10 to be visible for comparison. In CAM6, south of 50°S, the organic mass concentration is one order of magnitude less than that of sea salt or sulfate (Figure 3.1d). Because MARCUS did not include observations of chemical composition, previous field campaign results were used for reference. SOCRATES measurements using Scanning Transmission Electron Microscopy (Twohy et al. 2021) and CAPRICORN2 data using Time-of-Flight Aerosol Chemical Speciation Monitor (Humphries et al. 2021) indicated that marine organic aerosol contribute only 11-20% of what sulfates contribute to the bulk hygroscopicity over SO. However, the contribution of organics to condensational growth and formation of CCN in other remote marine boundary layers can be large (Zheng et al., 2021, Westervelt et al., 2012, Zhao et al., 2021). Thus, further studies about marine organics influences on CCN in ESMs can still be helpful.

3.3.4. Untangling the CCN Source by Sea Ice Condition

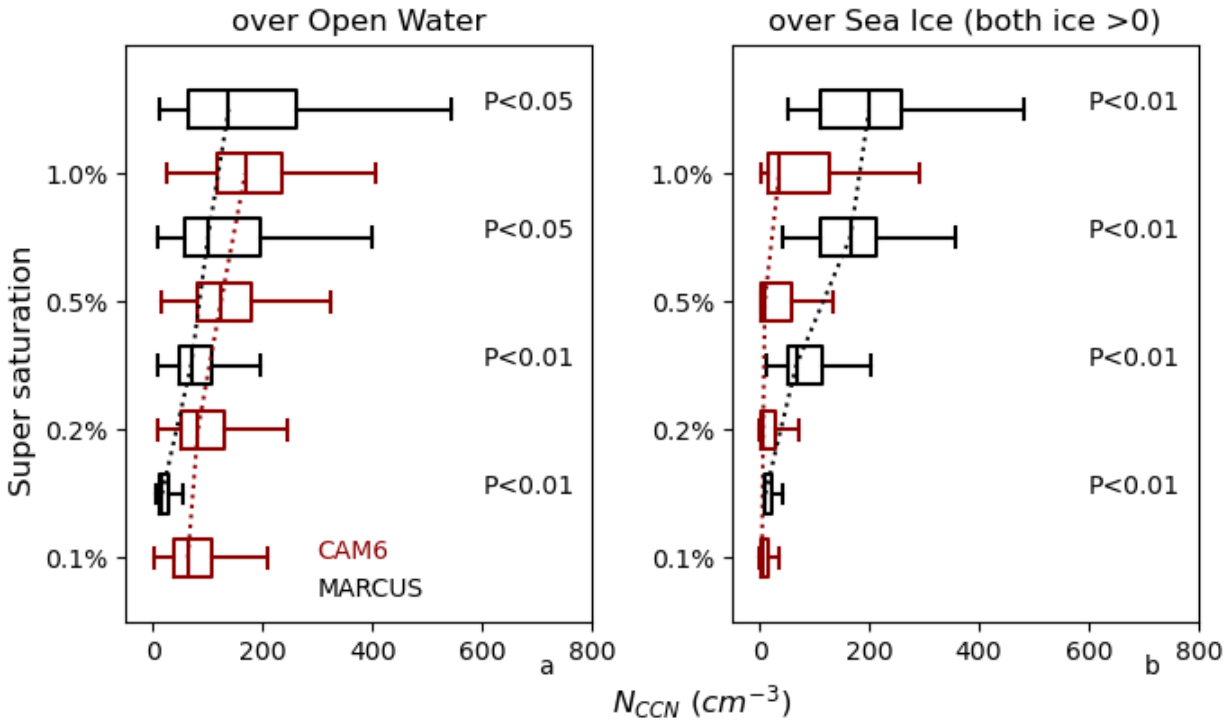

Figure 3.7 N_{CCN} -SS_w spectra over the open water (left) and sea ice (right) during the first three voyages of MARCUS from CAM6 in red and MARCUS in black respectively. The observation sample numbers are noted in text in black. The P values are results from Welch's t-test for each SS_w.

As discussed in Section 3.2.1, the observed sea ice was determined from a camera on the ice-breaker AA. The sea ice fraction is manually estimated as open water (0), broken ice (0.5), or solid ice (1) based on the sea ice coverage within the field of vision. Figure S3.3 shows the simulated (red) and manually estimated (black) sea ice fraction.

Figure 3.7 shows N_{CCN}-SS_w spectra as in Figure 3.6 but separates the samples by sea ice condition. Here the sea ice scenario (Figure 3.7b) is defined as when both the CAM6 simulated sea ice fraction is > 0 and the existence of sea ice was identified in the MARCUS observations (manual labeled sea ice scale > 0). Figure 3.7 shows that although the difference between means of CAM6 and MARCUS are all significant at a 0.05 significance level, the SS_w dependence of observed and simulated N_{CCN} are similar (Figures 3.7a than 3.7b), whereas the observed N_{CCN} more strongly depends on SS_w compared to CAM6 for data collected over sea ice. This suggests that the CCN type from CAM6 is more consistent with the MARCUS observations over the open water than over the sea ice. Compared with the CCN over the open water which provides primary CCN such as SS-CCN, the sources for local primary CCN are very limited over the sea ice. Gong et al. (2023) shows that fine sea salt aerosols from blowing snow over the sea ice can become natural CCN. However, as for the current use of CICE5, CAM6 does not include this snow-blowing-oriented CCN. This can be another reason for this different bias between over open-water and over sea ice.

The secondary CCN including the MB-CCN can thus become the primary contributor to N_{CCN}. Considering the air masses over the SSO come from higher altitudes compared to that over the NSO (Humphries et al. 2021), the long-distance transport of SS-CCN can be limited. This is consistent with Figure 3.7 showing that the CAM6 simulates the SS-CCN better than the MB-CCN. The fact that the underestimated N_{CCN} co-exist with the overestimated hygroscopicity, highlights the missing sulfates over the sea ice from the CAM6.

Considering the AA is an ice breaker which breaks the ice to move ahead, there are still sea ice leaks towards the heading of the ship even with a full coverage of sea ice in the field of vision. Sensitivity tests of sea ice conditions were performed, and results are provided in the supporting Figures S3.8 and S3.9 for sea ice scales of 0.2 and 0.7 respectively. The corresponding numbers of observed sea-ice-sample are shown by side at given sea ice scale. Figure 3.7, Figures S3.8 and S3.9 all show consistent conclusions as discussed above.

3.4. Conclusions and Discussion

In this chapter, reasons for the failed capture of the natural summertime marine cloud brightening close to the Antarctic Marginalized Ice Zone where cloud droplet number concentrations are underestimated by a factor of 2 over the South Southern Ocean (SSO) based on the nudged simulation of CAM6 (Gettelman et al. 2020) are investigated. Specifically, the number concentration of CCN over the SO is assessed by comparing data from field campaigns carried out over the summertime SO during MARCUS with output from the CAM6 nudged run for the corresponding time and location. This study quantifies the difference in observed and modeled N_{CCN} to better understand the CCN type transition by season and latitude.

The following are the main findings of this study:

- There indeed exists a low bias of N_{CCN}, with a relative bias up to -89% over the southernmost SO close to the Antarctic. For non-precipitating only scenarios, the low bias still exists over the areas south of 55°S with a modified normalized mean bias (B_n) of -35% for $N_{CCN,0.2}$.
- There also exists positive relative biases of $N_{CCN,\ 0.2}$ and $N_{CCN,\ 0.5}$ larger than +500% between 50°S-55°S, which is consistent with increased level of simulated sea salt mass concentration over this region.
- The underestimation of small Ac (as large as 80%) largely contributes to the underestimation of total Ac. Together with the overall underestimation of N_{CN} over the NSO, the increased activation ratio of CCN is underestimated by the CAM6 over the SSO and overestimated further north.
- The simulated and observed N_{CCN} have different mean values (11 out of 12 passed the Welch's t-test at the significance level of 0.05). Over the NSO, this is consistent with an overestimate of SS-CCN. CCN type over the NSO is better simulated by the CAM6 based on the slope of N_{CCN} - SS_w spectra. But the CCN type over the SSO is biased as shown by the overestimated hygroscopicity, consistent with the missing MB-CCN such as underestimated sulfates.
- The similar shape of observed and modeled N_{CCN} - SS_w spectra over the open water compared to that over sea ice imply that the CAM6 simulated primary SS-CCN better, compared to the MB-CCN. The overestimation of hygroscopicity over the ice is consistent with the missing MB-CCN such as sulfates.

The finding of potential overestimation of sea salt and underestimated sulfates over the SO is consistent with previous publications (McCluskey et al., 2023) using SOCRATES and CAPRICORN2 data.

There are some limitations of the current study that future studies and experiments can investigate. First, no chemical composition measurements from MARCUS were made; such measurements would provide the most direct data to compare with modeled latitudinal and seasonal transition of CCN types over the SO. Further deployment of mass spectrometers over the SO, particularly over the SSO, could provide the necessary data to assess simulated aerosol types.

Second, although measurements on mobile platform can help fill in the gaps from land-based long-term stations that are distant from regions of productivity in the ocean and sea-ice (Mallet et al., 2023), direct quantitative precipitation measurements from ship-borne platforms are harder to achieve due to a number of reasons. Sea spray aerosol and high winds influence surface-based tipping bucket measurements, making the quantification of light drizzle, which is frequent over the SO extra challenging (Montoya Duque, E. et al., 2022; Tansey et al., 2022). The semi-Eulerian sampling method (using mobile surface observing platform) during the MARCUS campaign is also unable to capture the full statistical distribution of precipitation rate and frequency. Additionally, CAM6 has a much longer timestep compared to the observation sample frequency, thus smoothing or averaging of observations can easily weaken the signals such as that of small-scale intermittent precipitation particularly when the ice breaker is moving fast. Observations of surface level precipitation are thus limited to radar reflectivity at 94 GHz. Siems et al. (2022) mentioned that there is no “truth” for precipitation across the SO region that covers ~15% of the

Earth's surface, and the fundamental understanding of precipitation phase, duration, and intensity over the SO still need further studies and analysis. All these above demand better quantifications of wet-scavenging and its influence on N_{CCN}, which is challenging and confusing currently.

Third, future studies can combine different field campaign measurements and satellite retrievals for synergistic analysis. This would allow expansion of the analysis from the MARCUS data which had limited independent samples after the removal of precipitating time periods, ship-stack contaminated samples, and times with instrument problems. Potential future studies can be performed by combining 1) satellite data (Mace et al., 2024, Werdell et al., 2019), 2) long-term static station observations at Kennaook-Cape Grim, Dumont d'Urville, and Baring Head, 3) other ship-borne data such as that acquired using the French RV Marion Dufresne, "Polar POD", and Australia's RV Investigator, and 4) data from up-coming field campaigns mentioned in Figure 3 in Mallet et al. (2023) such as the the Denman Marine voyage.

More importantly, the missing physics and model developments in the CAM6 should be a key objective for future studies since acquiring new observations may be years away. For example, the following updates could improve the quality of the simulations: update the SS-CCN by applying SO-related white cap parameterization (e.g. Albert, M. F. M. A. et al. 2016); update the MB-CCN using new surface emission dataset or online ocean DMS emissions (e.g. Online Air-Sea Interface for Soluble Species parameterization) (Johnson, 2010; Wang et al. 2019; Duseong et al. 2023); update the SSO CCN types using a potential updated sea ice scheme that includes drifting snow over ice; better represent the CCN type and its corresponding hygroscopicity factor kappa as one of the inputs to the Abdul-Razzak & Ghan parameterization; and update the aerosol microphysics

using aerosol schemes such as Community Aerosol and Radiation Model for Atmospheres (CARMA, Tilmes et al. 2023).

Regardless, compared to traditional model-observation studies which heavily rely on the column-based aerosol optical depth, this study presents an informative assessment of CCN predicted in a global climate model, proving a new diagnostic to use for assessing ESMs that specifically addresses the aerosols' potential indirect effect on clouds over a radiative important but pristine region. The study also examined marine boundary layer CCN using a unique ship-borne dataset from MARCUS, which are physically close to the locations of white capping and DMS emission and thus enhanced the understanding of natural background CCN over one of the most pristine areas on the Earth.

4. Observation-oriented CAM6 modification on SO CCN and the Influence on Cloud Droplet Number Concentration

4.1. Introduction

The high positive bias of simulated surface shortwave solar radiation over the Antarctic coast is one of the largest biases in Earth System Models (ESMs) over the Southern Hemisphere, and in fact, globally (Mallet et al., 2023). The SO has approximately 80% cloud coverage, dominated by reflective marine boundary layer low clouds (Mace et al., 2021; Huang et al., 2012; Naud et al., 2014; Warren et al., 1988). Global models have highlighted the important role of SO clouds for the extensive reflection of solar radiation by low-level clouds (Trenberth & Fasullo, 2010; Matus

et al. 2017). Even small changes in low cloud brightness in this region can significantly alter cloud feedback and climate sensitivity (Tan et al. 2016, McCoy et al. 2015). Cloud Condensation Nuclei (CCN) serve as particles on which water vapor condenses and are a limiting factor for cloud droplet number concentration (N_d). It is thus fundamental for ESMs to accurately represent CCN, including its abundance, size distribution, type, and latitudinal and seasonal variation.

An assessment of simulated CCN against ship-borne observations (Niu et al. 2024 and 2025) revealed two distinct biases of CCN in the Austral summer over the Australasian sector of the SO in the Community Atmospheric Model (CAM6, atmosphere section of the CESM) compared to a ship field campaign: 1) an overestimation of N_{CCN} at 0.2% and 0.5% supersaturation ($N_{CCN,\ 0.2}$ and $N_{CCN,\ 0.5}$) north of 55°S associated with an overestimation of accumulation mode sea salts, and 2) a close to 100% underestimation of $N_{CCN,\ 0.2}$ and $N_{CCN,\ 0.5}$ south of 55°S associated with an underestimation of secondary CCN, potentially sulfates. This paper, motivated by the biased SO N_{CCN} reported in Chapter 3, aims at an observation-oriented modification of simulations to achieve better agreement between simulated and observed N_{CCN}, and to determine its influence on simulated N_d.

The pristine SO marine boundary layer (MBL) environment includes limited anthropogenic pollutants and primarily natural background aerosols (Uetake et al. 2020). Within the SO MBL, the dominant CCN types include sea salt, sulfates, and marine organic aerosols. Specifically, using airborne measurements during the Southern Ocean Clouds, Radiation, Aerosol Transport Experimental Study (SOCRATES) field campaign, Twohy et al. (2021) demonstrated that the

chemical composition of particles below clouds with dry diameters (D) of ~100 nm < D < 500 nm, which contributed the most to CCN (Niu et al., 2024), were dominated by sulfur-based particles. The second-most frequent particle type in this size range was sodium-based sea spray, which includes particles comprised of mostly sodium chloride and those that contain sodium but are enriched in sulfur and depleted in chlorine due to uptake and condensation of sulfur gases (Mclnnes et al., 1994).

However, in atmospheric models such as CAM6, mixed aerosols are typically represented by several specific types. For pristine natural aerosols over the SO, the most relevant CAM6-simulated aerosol types corresponding to the above observations are sea salt and sulfate. The sea salts are CCN-active particles that are emitted by bubbles bursting from the ocean surface driven by surface winds. Empirical formulas as a function of horizontal wind speed at 10-m (U_{10}) parameterize sea salt emissions, which can be activated at given thermodynamic conditions based on Köhler theory. Compared to the physical processes for sea salt emissions, the formation of secondary sulfate CCN, however, follows more complicated chemical processes.

Biogenic volatile sulfurous and organic compounds, such as dimethyl sulfide (DMS, CH_3SCH_3), produced by phytoplankton and bacteria, represent an abundant natural source of sulfur (Hopkins et al., 2023; Teng et al., 2021; Ayers & Gras, 1991; Charlson et al., 1987). After its release to the atmosphere, DMS oxidizes to form methane sulfonic acid (MSA), sulfuric acid (H_2SO_4), and other oxidation products (Chen et al., 2018; Fung et al., 2022) that can lead to new particle formation in the free troposphere and MBL (Zheng et al., 2021). These ultrafine Aitken particles can be

transported through subsidence and entrainment, where they can further grow and act as CCN (Clarke et al., 1998). A number of studies have identified additional sources of sulfate (e.g. Jongebloed et al., 2023) and intermediate species such as hydroperoxymethyl thioformate (Veres et al., 2020) and methanethiol (Wohl et al. 2024). These emerging studies, supported by observational data, suggest many ESMs, including CAM6, underestimate gas-phase reactive sulfur species emissions and oversimplify processes involved in the production and evolution of sulfate aerosols.

The SO is where global DMS production maximizes but is poorly constrained in models (Bock et al. 2021; Revell et al., 2019). Efforts made in better describing and quantifying complex sulfate/DMS oriented chemistry into ESMs are still on-going (e.g. Kang et al. 2025, Jongebloed et al., 2024, Revell et al., 2019, Cala et al., 2023, Zhao et al., 2024). Instead of representing all the details of sulfate chemistry, this study aims at investigating the balance between sea-salt and sulfates as SO CCN and its subsequent influence on N_d and radiation in the commonly used less expensive CAM6. For sulfate aerosols regulating SO CCN seasonal and latitudinal variation (McCluskey et al. 2023, McCoy et al. 2021, Niu et al. 2024, and Humphries et al. 2021), given CAM6 with its simplified chemistry, a stopgap is made to manually elevate the sulfur source by increasing surface DMS emission.

Data acquired during the Measurement of Aerosols, Radiation, Clouds over the Southern Ocean (MARCUS) provide unprecedented season and latitudinal coverage of SO MBL CCN (McFarquhar et al. 2021). The MARCUS time coverage of 2018 spring and summer provides

different scenarios for DMS emissions, and the spatial coverage of 45-68°S provides different scenarios for dominant CCN types. Data acquired during the Southern Ocean Cloud Radiation and Aerosol Transport Experimental Study (SOCRATES) provide vertical distribution of aerosols during the same summer as MARCUS. And data acquired during the Clouds Aerosols Precipitation Radiation and atmospheric Composition over the Southern Ocean (CAPRICORN II) provide chemical observations of CCN-active aerosols south to the Antarctic coast, also during the 2018 summer. In this study, data acquired from the above three field campaigns are curated to investigate the CCN in the CAM6 model, in detail, 1) the CAM6 simulated N_{CCN} is modified by reducing sea salt emissions and increasing DMS emissions, 2) the performance of CAM6 with these modifications is evaluated by comparing simulations with observations during a sea-salt-dominant case and a sulfate-dominant case, 3) the sequential influence on N_d by comparing simulated N_d with those from surface-based remote sensing retrievals is checked, and 4) the resulted impacts on the top of atmosphere cloud shortwave radiative forcing is illustrated by comparing with the base-run results.

4.2. Methodology

To resolve the bias identified in Chapter 3, simulation configurations and co-locations presented here follow their configurations and are briefly mentioned in the Supporting Information Text S4.1. Details and summaries of the three field campaigns during the 2018 summer can be found in McFarquhar et al. (2021) and the aerosol measurement details can be found in Niu et al. (2024), Humphries et al. (2021), Sanchez et al. (2021), and Twohy et al. (2021). Only 1) narratives of the default representation of relevant aerosols, and modifications of their representation, and 2) application of remote retrievals are discussed here. The customized data selection and

4.2.1. Default configuration and modification of sulfates.

In CAM6, the default DMS surface fluxes are prescribed from a monthly mean climatology (Figure S4.1) from the marine biogeochemistry model (the HAMburg Ocean Carbon Cycle Model, HAMOCC5) (Maier-Reimer 1984, Maier-Reimer and Hasselmann 1987). Surface emission is parameterized using the DMS gas transfer velocity times the DMS concentration in the surface ocean water (Nighttingale et al. 2000). The DMS gas transfer velocity is proportional to the square of wind speed at 10 m (U_{10}^2) and the sea surface temperature, and quantifies the transfer of DMS across the air-sea interface. Related gas-phase chemical reactions used in the default CAM6 configuration include the oxidation of DMS to SO_2 and then to H_2SO_4. Details of new particle formation and nucleation pathways are found in Kang et al. (2025) for the related default E3SMv2 model, consistent with those used in CAM6.

In this chapter, the surface emission of DMS is multiplied by 2, 3, and 10 in sensitivity tests, which are represented by the acronyms DMS×2, DMS×3 and DMS×10, respectively. The range of DMS is selected based on time series comparison between simulations and observations (figures not shown). This method of scaling surface DMS emission is also used in Mulcahy et al. (2018), where they also add an extra 0.7 (in total DMS×1.7) for missing marine organic sources.

4.2.2. Default configuration and modification of sea-salt.

In CAM6, the mobilization flux of sea salts, by default, is proportional to U_{10} above the water to the power of 3.41 (Gong et al., 1997, 2003) times the fraction of open water at each grid. Recent studies (Revell et al., 2019; Hartery et al., 2020) show the previous $U_{10}^{3.41}$ parametrization

(Monahan & Muircheartaigh, 1980; A. D. Clarke et al., 2006, Gong, 2003) can overestimate the surface source by a factor of 2-4 for the SO, while $U_{10}^{2.8}$ is a better fit for high-wind environments. Hartery et al. (2020) validated the new $U_{10}^{2.8}$ parametrization by comparing the predicted sea spray aerosol concentration with aircraft measurements during SOCRATES, and Kang et al. (2022) applied the $U_{10}^{2.8}$ parameterization in a simplified source-and-sink budget model to SOCRATES data. In this study, $U_{10}^{2.8}$ is thus used to replace $U_{10}^{3.41}$ in a sensitivity test.

4.2.3. Setup of sensitivity tests

Sensitivity tests were designed to test each possible combination of modifications to emissions of sea salts (default $U_{10}^{3.4}$ or $U_{10}^{2.8}$) and sulfates (default DMS, DMS × 2, DMS × 3 or DMS × 10) described in Sections 4.2.1 and 4.2.2 (Table S4.1). Tests are referred to by their corresponding acronyms hereafter.

4.2.4. Retrievals of cloud droplet number concentration

For MARCUS, cloud properties such as N_d were retrieved using surface-based measurements from lidar, radar, and microwave radiometer. The retrieval algorithm (Mace et al. 2024a) applies a lidar forward model to non- or lightly precipitating liquid clouds with liquid water path < 200 g m^{-2}. The method utilizes the depth to the maximum in lidar-attenuated backscatter to estimate N_d with an uncertainty of about 30%. Mace et al. (2024b) evaluated these retrievals against satellite observations from the Moderate Resolution Imaging Spectroradiometer.

4.3. Results

4.3.1. Statistical Results

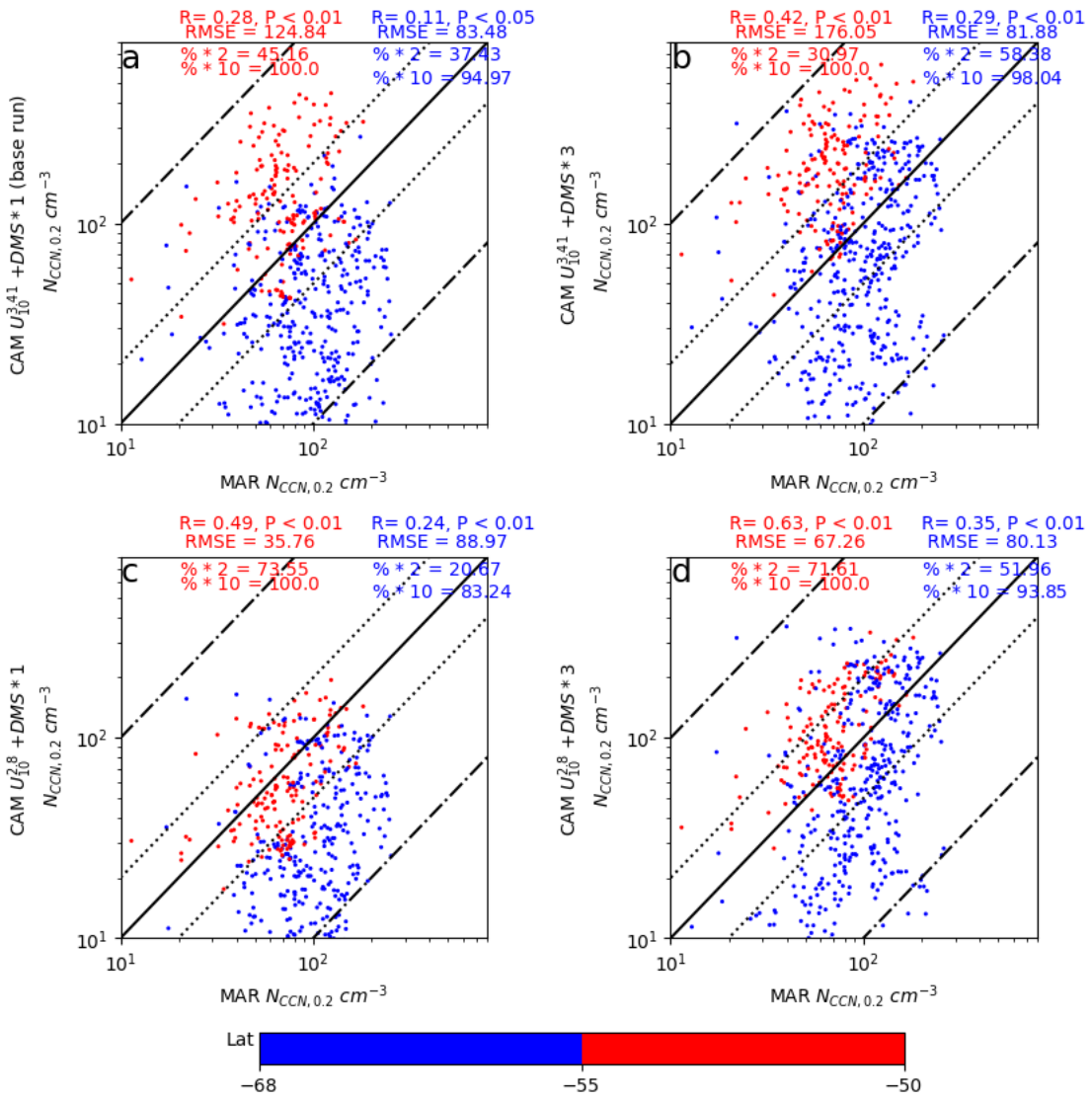

Figure 4.1 Scatter plot of $N_{CCN,0.2}$ simulated by CAM6 against MARCUS observations colored by latitude for times the ship was south of 50°S. In each panel, black solid line indicates 1:1 agreement, while dotted and dashed lines represent agreement within a factor of 2 and 10, respectively. The Pearson Correlation Coefficient (R) with P value, RMSE, along with percentage of data points falling within a factor of 2 (%′2) and 10 (%′10) agreement is reported in each panel. Values in blue (red) correspond to latitudes south of 55°S (from 50-55°S). Panel a shows base simulation using default DMS emission and wind dependence ($U_{10}^{3.41}$), panels b-d show sensitivity tests: b with $U_{10}^{3.41}$+DMS × 3, c with $U_{10}^{2.8}$+DMS×1, and d with $U_{10}^{2.8}$+DMS × 3.

Figure 4.1 compares simulated and observed $N_{CCN,\ 0.2}$. The Root Mean Squared Error (RMSE) measures the average magnitude of the errors but penalizes larger errors heavily by squaring the residuals. The Pearson Correlation Coefficient (R) illustrates if the observations and simulations vary together linearly, and the proportion of samples falling within a factor of 2 and 10 of the observations (2-fold coverage and 10-fold coverage) evaluates the percentage of bias outliers.

To combine the RMSE, R, and 2-fold (10-fold) coverage for comprehensive evaluation, with baserun as reference, a larger enhancement of $N_{CCN,\ 0.2}$ model performance over the 50-55°S region (in red) is shown by updating sea salt emissions in Fig 4.1c compared to updating DMS emissions in Fig 4.1b. A comparison between Fig 4.1a and Fig 4.1c reveals the sensitivity of the simulation to reduced sea salt emissions. Over 50-55°S (in red), model-observation agreement improves substantially, with RMSE decreasing from 124.84 cm^{-3} to 35.76 cm^{-3} and R from 0.28 to 0.49 at significance level 0.01. Fig 4.1c also illustrates a higher 2-fold coverage, increasing from 45.16% to 73.55%. This is consistent with the larger contribution of sea salt to CCN in this region, as indicated by Fig 3.1d and Fig 3.1e in Chapter 3, which show that sea salt fraction of accumulation mode aerosols (70 nm < D < 700 nm) number concentration is higher over 50-55°S and strongly dependent on wind speed.

For $N_{CCN,\ 0.2}$ south of 55°S (in blue), the enhanced model performance is realized in Fig 4.1b compared to Fig 4.1c. Sensitivity tests incorporating a tripling of surface DMS emissions serve as examples of sulfate enhancement. A comparison between Fig 4.1a and Fig 4.1b shows that increasing surface DMS emissions alone (test $U_{10}^{3.41}$+DMS × 3) results in statistically better

agreement between simulations and observations of $N_{CCN,\ 0.2}$ south of 55°S (in blue), with the RMSE decreasing from 83.48 cm^{-3} to 81.88 cm^{-3}, R increasing from 0.11 to 0.29, and the 2-fold (10-fold) coverage increasing from 37% to 58% (from 95% to 98%). This is likely associated with higher summertime sulfate concentration in this region, consistent with observations reported by Humphries et al. (2021) and Niu et al. (2024), and simulations presented in Chapter 3.

Fig 4.1d presents results from the sensitivity test $U_{10}^{2.8}$+DMS × 3, which incorporates both increased sulfates and reduced sea salt emissions. Compared to both $U_{10}^{3.4}$+DMS × 3 and $U_{10}^{2.8}$+DMS×1, this combined approach yields higher R, lower RMSE, and higher 2-fold and 10-fold coverages for $N_{CCN,\ 0.2}$ across the whole pristine SO. For Fig 4.1d itself, statistics show model performance is better over 50-55°S (in red) than further south (in blue). This difference is associated with the fact that >85% of the blue points outside of the 2-folder envelope in Fig 4.1d fall below the 1:1 line, indicating a systematic underestimation of simulated $N_{CCN,\ 0.2}$ relative to observations. It suggests that a simple, uniform tripling of surface DMS emissions may not adequately represent sulfate sources or its formation pathways south of 55°S.

All the above results are consistent with $N_{CCN,\ 0.5}$ (Figure S4.2). Detailed case studies with time series are presented in Section 4.3.2 and 4.3.3.

4.3.2. Case Study 1: Sea salt dominant scenario

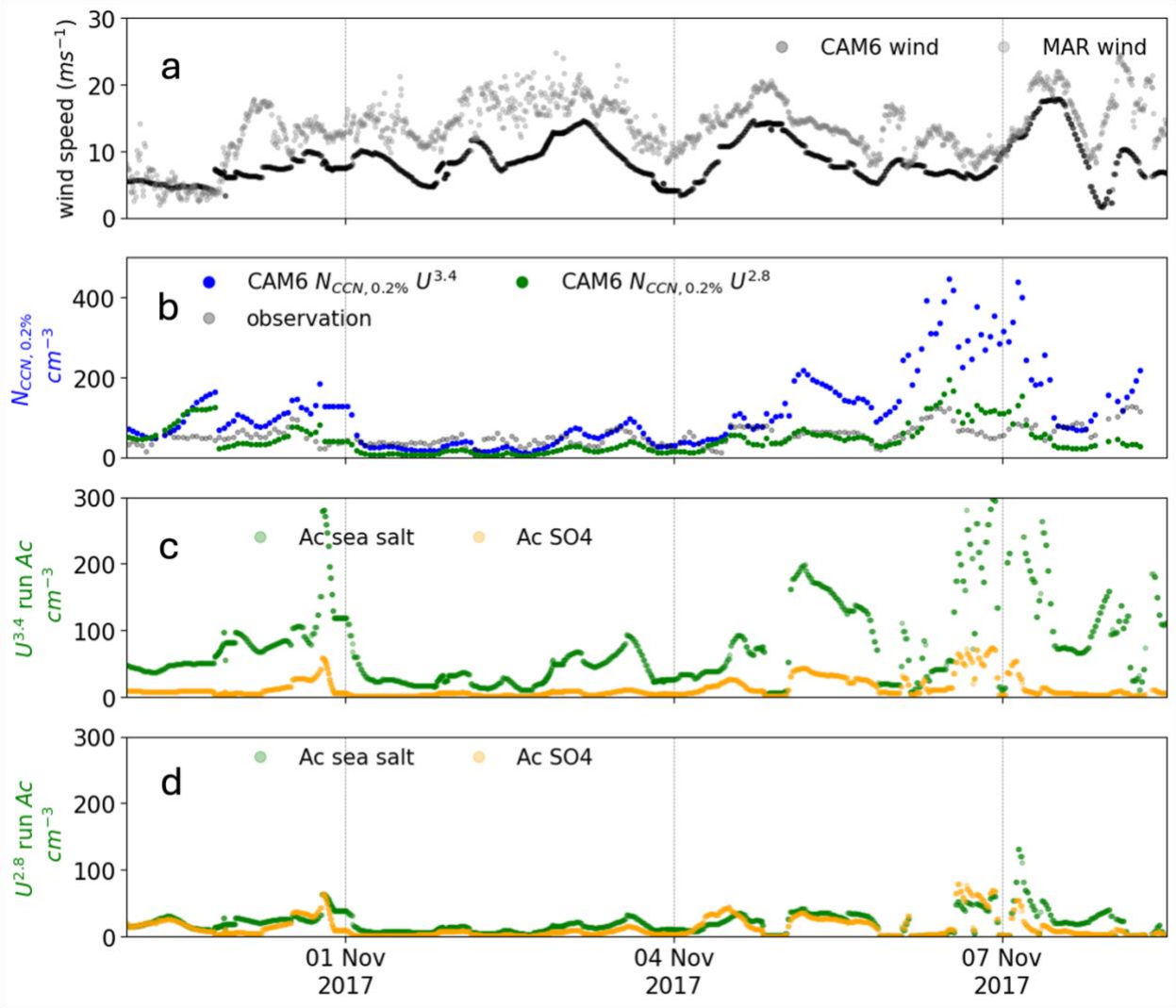

Figure 4.2 Time series during November 2017 voyage from Hobart to Davis of (a) surface wind speed with observations in grey and CAM6 simulations in black, (b) $N_{CCN,\,0.2}$ from CAM6 $U^{3.4}$ run in blue, from $U^{2.8}$ run in green, and observations in grey, (c-d) accumulation mode (Ac) sea-salt in green and sulfates in yellow, from CAM6 $U_{10}^{3.4}$ run in (c) and $U_{10}^{2.8}$ run in (d).

For a sea-salt-dominant case in Figure 4.2, updates on wind speed dependence improve the simulated N_{CCN}. In Fig 4.2a, the wind speeds from the CAM6 (default run using the $U_{10}^{3.4}$, in black) in general are underestimated during this period. While in Fig 4.2b, the simulated $N_{CCN,\,0.2}$ (default run using the $U_{10}^{3.4}$, in blue) are underestimated compared with the observations in grey. The underestimation of wind speed may be related to the nudging method; however, the underestimation of wind speed corresponds to overestimation of CCN number needs further

investigation. Fig 4.2c and Fig 4.2d therefore respectively show the accumulation mode sea-salt and sulfates number condensation before and after applying the updated wind speed dependence. Fig 4.2c shows the times of overestimation of sea salts are consistent with the overestimation of $N_{CCN,\,0.2}$ in Fig 4.2b in blue. These overestimations of sea salt are improved as shown in Fig 4.2d, which may explain the better agreement shown in Fig 4.2b between the simulated $N_{CCN,\,0.2}$ in green and the observations in grey. Similar updates are also seen for $N_{CCN,\,0.5}$ shown in the Supporting Information (SI).

4.3.3. Case Study 2: Sulfate dominant scenario

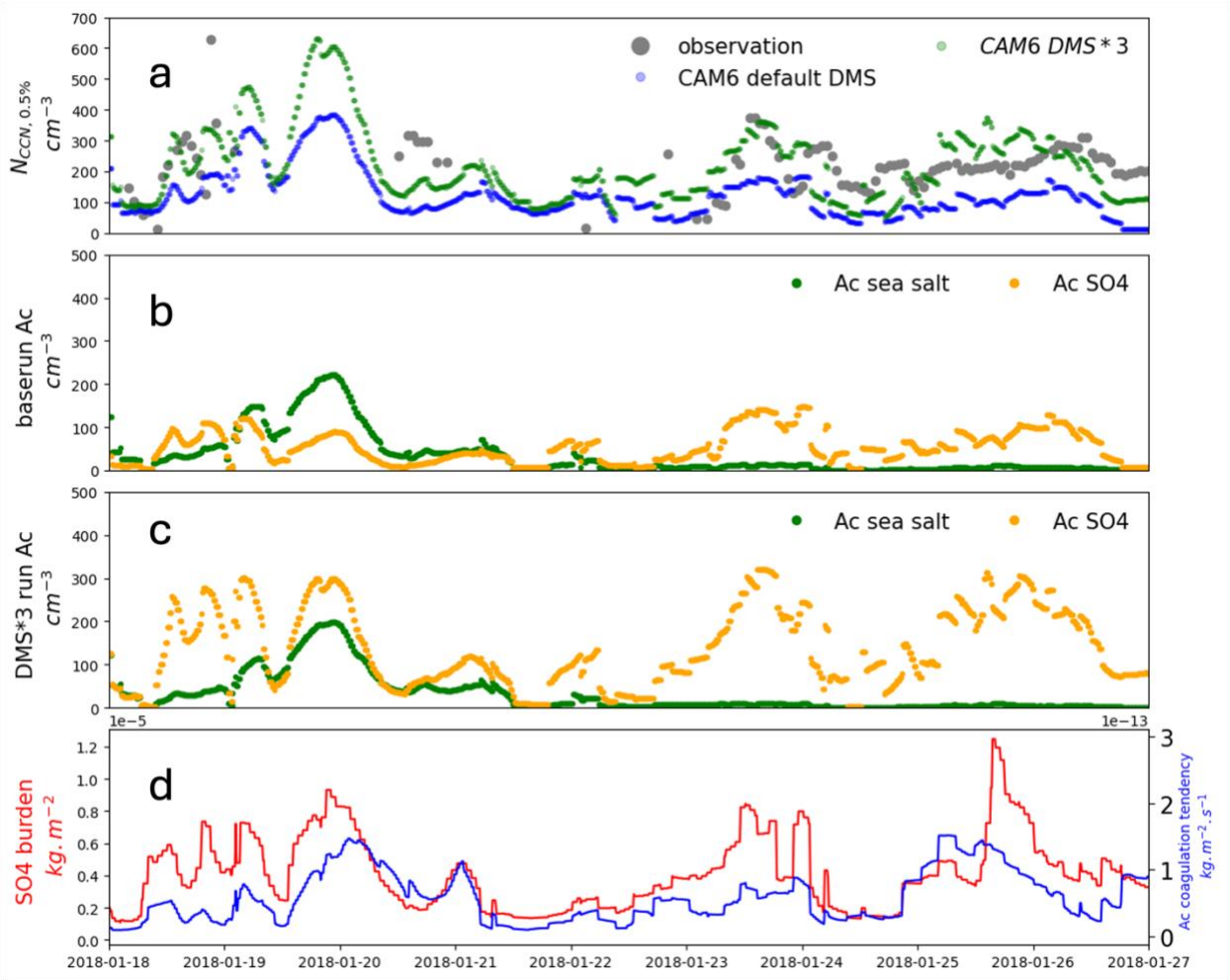

Figure 4.3 Time series during January 2018 voyage from Hobart to Casey of (a) $N_{CCN,\,0.5}$ from CAM6 $U^{3.4}$ run in blue, from $U^{2.8}$ run in green, and observations in grey (observation data gaps for

ship stack contamination removement); (b-c) number concentration of accumulation mode (Ac) sea-salt in green and sulfates in yellow, from CAM6 $U_{10}^{3.4}$+DMS×1 run in (b) and $U_{10}^{3.4}$+DMS × 3 run in (c); (d) vertically integrated mass of total sulfate burden in red and vertically integrated coagulation tendency of Ac mode sulfate from Aitken mode sulfates in blue.

Figure 4.3 shows a similar figure as Figure 4.2 but with time series of sulfate burden and sulfate coagulation tendency replacing wind speed. Fig 4.2a illustrates the base-run in blue provides underestimated $N_{CCN,0.5}$ compared with the observations in grey. The agreement between observations and simulations is better achieved for the $U_{10}^{3.4}$+DMS × 3 run in green. Fig 4.3b and Fig 4.3c respectively shows the number of Ac sea-salt and sulfates with the default DMS and DMS × 3. The increased amount of $N_{CCN,0.5}$ in Fig 4.3a is consistent with the increased amount of Ac sulfates, particularly during the peaks on Jan 18th and during 23rd-27th. The increased amount of Ac sulfates mass is largely influenced by gaining mass from Aitken coagulation indicated by blue lines in Fig 4.3d, while the other sources, for example, direct emission from external forcing, gas phase sulfuric acid condensation or chemistry production and their associated modal mass redistribution influence comparably less (figures not shown). Given the input data of DMS emission is monthly mean and that CAM6 has 1-degree resolution, this agreement between the $U_{10}^{3.4}$+DMS × 3 simulated $N_{CCN,0.5}$ and the 1-hour resolution ship-borne measurements is already commendable. However, the time series shows that there are some time periods during which the CAM6 still underestimated the observed peaks. To extend this to the whole January, these underestimations can be seen from the N_{CCN}-SS_w spectra below. Other time series plots like Figure 4.3 but for $N_{CCN,0.2}$ can be seen in the SI.

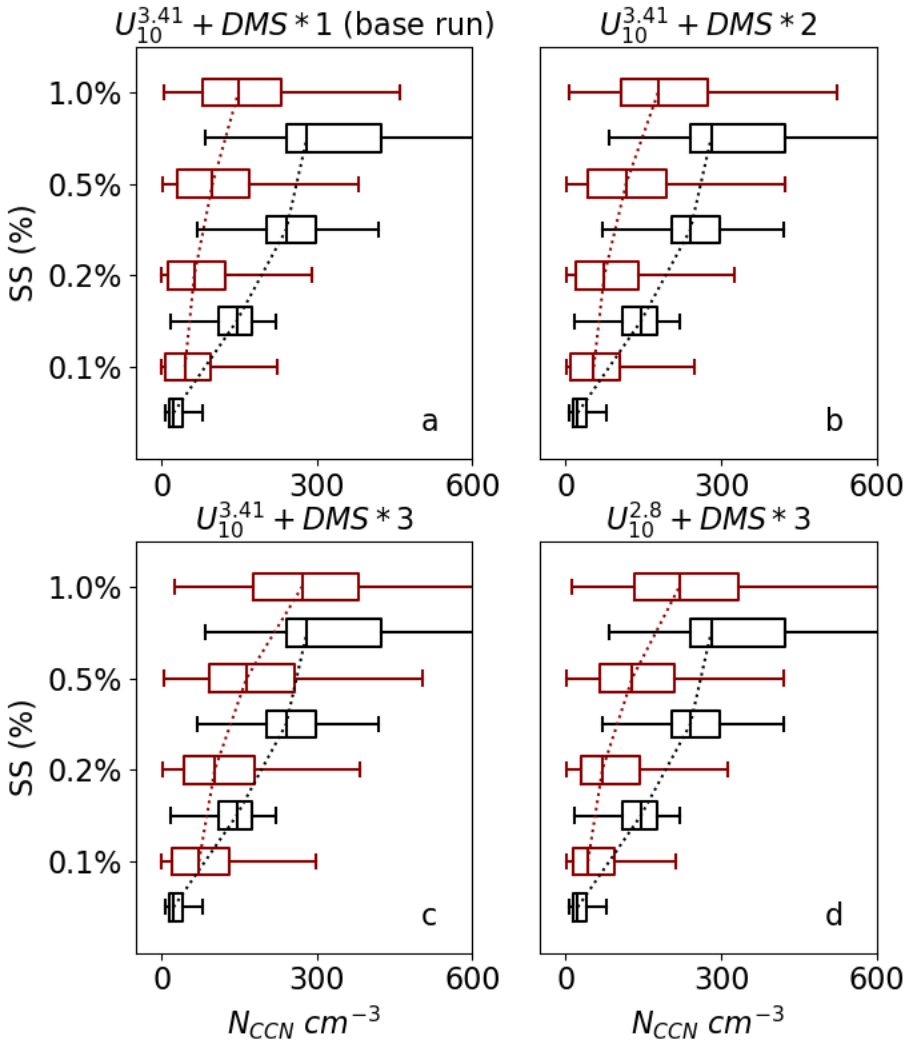

Figure 4.4 N_{CCN}-SS_w spectra with data during the 2018 January voyage from Hobart to Casey Station for (a) base run, (b) $U_{10}^{3.41}$+DMS × 2, (c) $U_{10}^{3.41}$+DMS × 3, and (d) $U_{10}^{2.8}$+DMS × 3 with observations in black and CAM6 simulations in red. The dashed lines connect the median values of N_{CCN} for each SS_w bin.

For a sulfate dominant case presented in this section in Figure 4.4 during the peak summer, updates on surface DMS emission enable a better agreement between CAM6 and observations. The sloping black dashed line in Figure 4.4 indicates that observed CCN (in black) are less hygroscopic

compared to the nearly vertical dashed red line in this case. Similar N_{CCN}-SS_w but for the sea-salt case with a nearly vertical dashed black line can be seen in the SI. In Fig 4.4a, the CAM6 base run (in red) 1) overestimates hygroscopicity, as indicated by the steeper slope of the red dashed line, and 2) underestimates N_{CCN} at SS_w of 0.2%, 0.5%, and 1.0%.

The scaling of DMS from 1 to 2, and 3 enables the red dashed lines to curve towards the right. For the CCN spectra, $N_{CCN,\ 1.0}$ corresponds to smaller particles more responsive to recent particle formation events that are the most sensitive to the scaling of DMS emission. $N_{CCN,\ 0.1}$ corresponds to larger particles and is the least sensitive reactor. As a result, the shape of the red line becomes more convex in Fig 4.4c. With the scale of 3, except for $N_{CCN,\ 0.1,}$ N_{CCN} at all other SS_w are still underestimated. In detail, a larger portion of the smaller particles (e.g. indicated by $N_{CCN,\ 1.0}$) have been able to grow and serve as CCN at 0.5% and 0.2% (the SS_ws closest to observations). For the CAM6, to achieve the best agreement of $N_{CCN,\ 0.2}$ and $N_{CCN,\ 0.5}$ between observations and simulations, a scale of DMS emission high as 10 is necessary (figure shown in the SI). If further taking the updates of wind speed dependence on sea salt particles into consideration, the values of simulated $N_{CCN,\ 0.1}$ become less in all the $U_{10}^{2.8}$ runs, leading to the shape of the curve from the simulation being further convex compared to the concave shape of the observed slope (Fig 4d).

There are a number of reasons why the 17th to 29th January 2018 is chosen as a typical case. First there are three field campaigns that happened during this particular time period over the Australasian Southern Ocean. Motivated by Chapter 3 which applied unique observations from MARCUS (conducted 29th October to 24 March 2018, between Hobart and the Antarctic coast) to

show the seasonal and latitudinal bias of CCN over the SO, the current study aims to guide the modification of the CAM6 using observations. Therefore, comprehensive variables including the vertical distribution of Ac from SOCRATES (15th Jan to 26 February 2018, conducted primarily over north of 60°S) and chemical composition data from CAPRICORN 2 (conducted 11 January to 21 February 2018, primarily during peak summer, between Hobart and the Antarctic coast) can be used to evaluate of sensitivity runs and their physical interpretations. 2) Except for the scaling of DMS, the sensitivity of CCN amount and size-hygroscopicity (indicated by red dashed lines in Figure 4.4) also depends on the absolute amount of surface DMS emission. Based on the Climatology, the high emission of DMS happens in peak summer when biological activities are active. Although the observed CCN during both January and February in 2018 during MARCUS are populated close to the Antarctic coast with a lower hygroscopicity than simulations (Figure in SI), the DMS emission input file (details in Section 4.2.1) shows a lower mass condensation in February than in January (Figure in SI). This may be related to the less sensitive of N_{CCN} spectra to the DMS modification in February (Figure in SI).

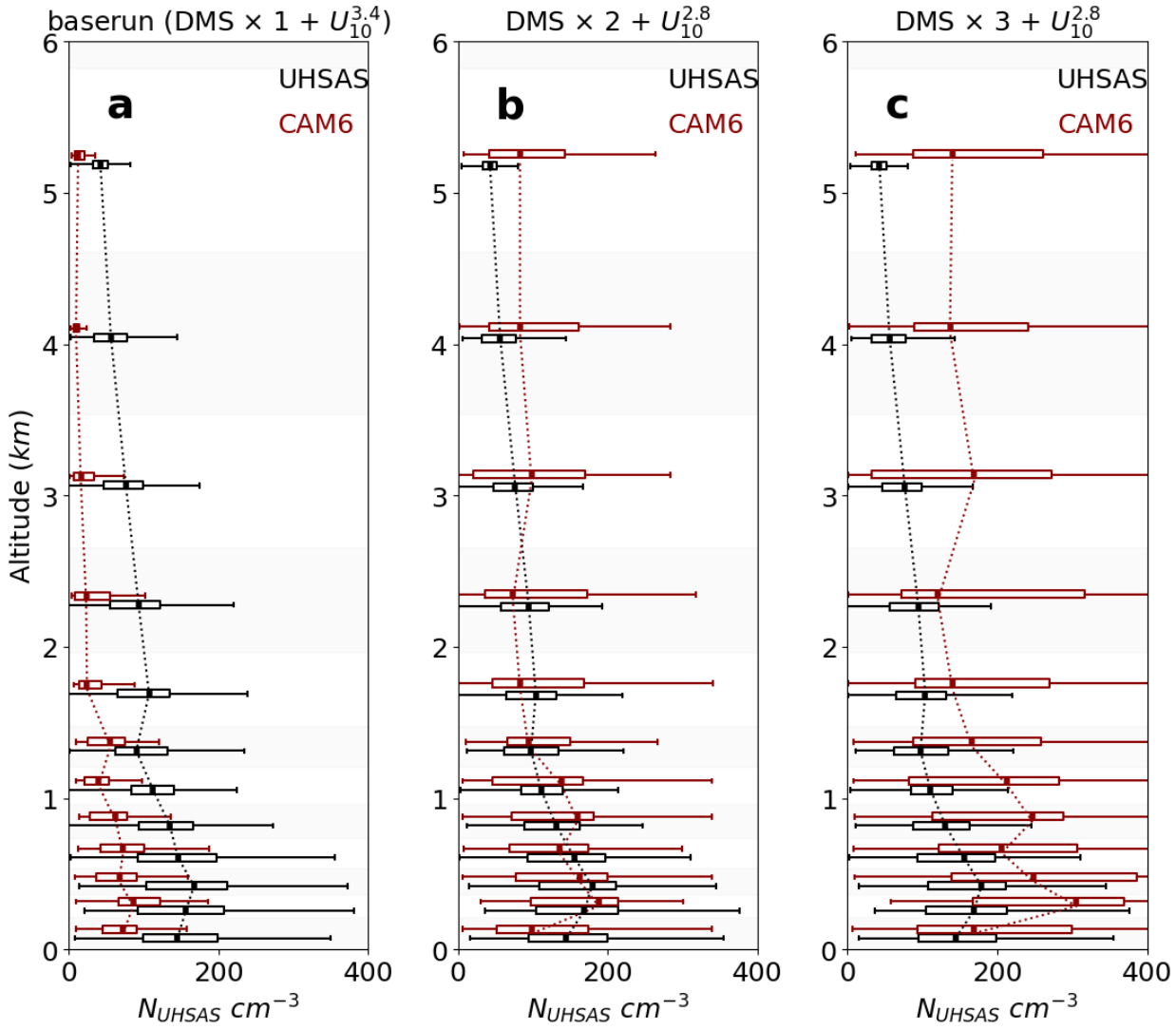

Figure 4.5 Comparisons of observed (black) and simulated (red) vertical distribution of Ac number concentration during the SOCRATES field campaign, with the base run on in a, $U_{10}^{2.8}$+DMS × 2 in b, and $U_{10}^{2.8}$+DMS × 3 in c. The dashed lines connect the median values of N_{CCN} for each SSw bin. Only the scenarios when relative humidity less than 90% is included.

In addition to the analysis using the MARCUS data, Figure 4.5 illustrates data acquired during the SOCRATES over the Australian SO during the same month of January. Fig 4.5a shows the observed Ac number measured by the Ultra High Sensitivity Aerosol Spectrometer (N_{UHSAS}) (60 nm < D < 1000 nm) has larger variations and medians at lower altitudes than higher altitudes. Fig 4.5a shows the vertical distribution of Ac simulated by the model compared to the measured

N_{UHSAS} is underestimated from the surface up to 5km. But the Ac simulated by CAM6 for the $U_{10}^{2.8}$+DMS × 2 run in Fig 5b shows insignificant differences from the medians of the SOCRATES measurements, although the variations in Ac from the CAM6 simulations illustrated by the error bars are larger than observed variation above 1km. However, the simulated Ac for the $U_{10}^{2.8}$+DMS × 3 run overestimated the medians and variations of measured N_{UHSAS} at all levels in Fig 4.5c. This implies that north of 60°S, doubling DMS leads to better vertical agreement between observed and simulated Ac than does tripling DMS. It further illustrates that the efficacy of increasing sulfates in the model by scaling the DMS inputs is different for different regions at varying elevations.

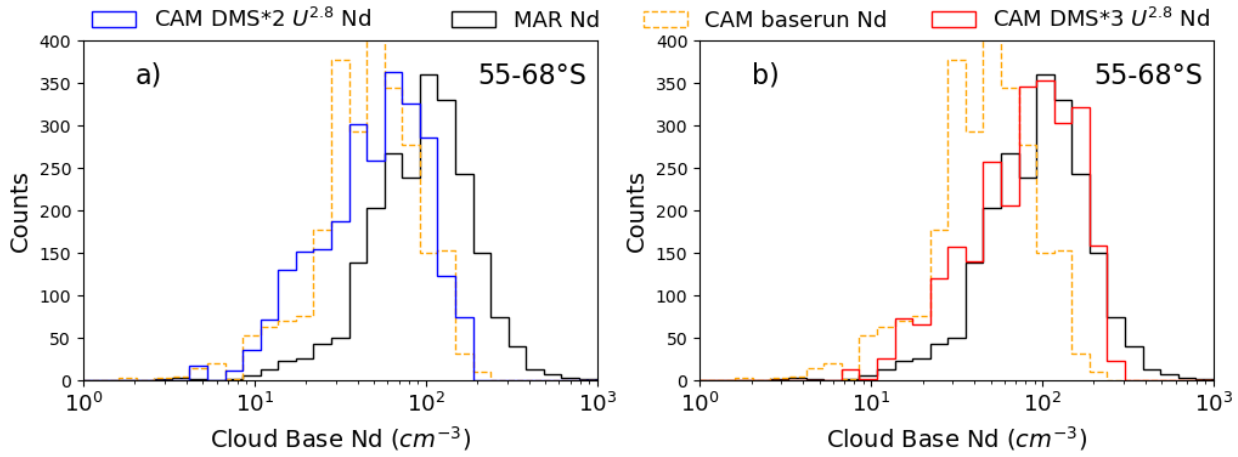

Figure 4.6 Histogram of cloud droplet number concentration (N_d) over 55°S–68°S from observations (MAR N_d; black) and simulations (CAM N_d; colored), with results from the base-run in orange and the test $U_{10}^{2.8}$+DMS × 3 in blue in (a) and $U_{10}^{2.8}$+DMS × 3 in red in (b). Only time periods with total precipitation < 0.01 mm h^{-1} and liquid water path < 200 g m^{-2} during the MARCUS voyages are included in the analysis.

Close to the Antarctic coast, it is hypothesized that underestimates in modeled N_{CCN} contribute to the misrepresentation of natural marine cloud brightening over the southern SO during austral summer, based on Chapter 3. Figure 4.6 demonstrates that N_d are more consistent with MARCUS observations for the $U_{10}^{2.8}$+DMS × 3 CAM run compared with the $U_{10}^{2.8}$+DMS × 2 CAM run. This

is consistent with Figure 4.4 which shows both $N_{CCN,\,0.2}$ and $N_{CCN,\,0.5}$ from the $U_{10}^{2.8}$+DMS × 3 CAM run have better agreement with the MARCUS observation. The retrieved N_d in black for non-precipitating thin clouds (LWP < 200 gm^{-2}) with no precipitation (total precipitation < 0.01 $mm\ h^{-1}$) exhibit a unimodal distribution centered around N_d = 100 cm^{-3}. The frequency of simulated high N_d scenario, defined in Mace et al. (2023) as the scenarios when N_d > 101 cm^{-3} which corresponds to the upper quartile of climatological statistics of long-term satellite retrieval N_d over the summertime SO, simulated by CAM6 base run (in yellow) is underestimated N_d by ~50% compared to retrievals (in black). Fig 4.6b show that the $U_{10}^{2.8}$+DMS × 3 run in red 1) increases the mode of N_d from 30 to 50 cm^{-3} compared to the base CAM run, more consistent with retrievals of N_d, 2) better simulates the high-N_d-scene frequency, but 3) still misses simulating scenarios with N_d > 250 cm^{-3}.

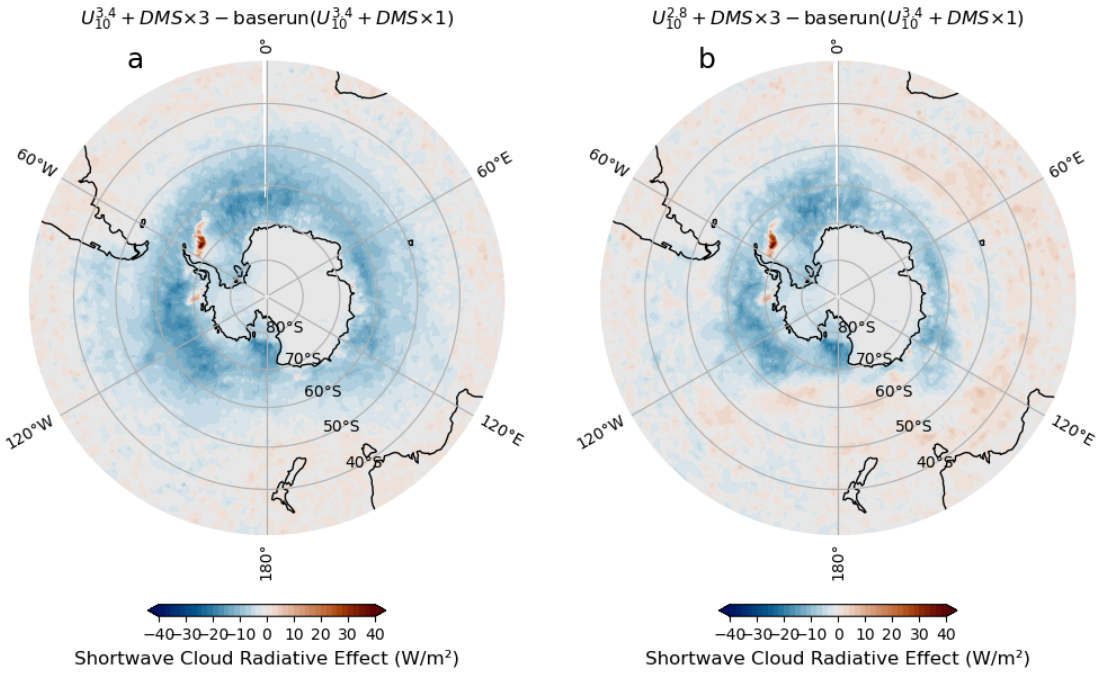

Figure 4.7 Difference of Shortwave Cloud Radiative Forcing (SCRF) at the top of atmosphere (TOA) over the SO during the January 2018 between the $U_{10}^{3.4}$+DMS × 3 run and the base run in (a), and between the $U_{10}^{2.8}$+DMS × 3 run and the base run in (b), with the color-bar settings identical to Figure 2 in Mallet et al. (2023).

Figure 4.7 illustrates the influence on shortwave reflection from the CAM6 updates that combine both wind speed dependence and DMS emission. The Shortwave Cloud Radiative Forcing (SCRF) is calculated using the net shortwave flux at the top of atmosphere (TOA) during all-sky condition minus that during clear sky conditions only. The analysis here is motivated by Figure 2 in Mallet et al. (2023) which shows that before the CAM6 updates there was universal positive bias in the amount of sunlight reaching the surface during the austral summer over the SO in 22 Coupled Model Intercomparison Project phase 6 (CMIP6) models compared to observations. Figure 4.7 shows that the blue color covers the most SO south of 55°S, implying more solar radiation gets reflected back to space by brighter clouds after the CAM6 updates. Fig 4.7b compared with Fig 4.7a shows that the including of sea salt updates constrains the reflective clouds to be along the Antarctic coast instead of over the general SO.

4.4. Conclusions and Discussion

This chapter, inspired by the Southern Ocean summertime shortwave bias close to the Antarctic coast noted by Mallet et al. (2023) and the identified CCN number bias noted in Chapter 3, aims to bridge the observations from field campaigns (MARCUS, SOCRATES, CAPRICORN II) with Earth System Model CAM6 simulations. CCN observations from aerosol probes are applied as guidance to modify aerosol parameterizations in the CAM6 model, whereas cloud droplet number concentration obtained from spaceborne radar-lidar retrievals are used for simulation evaluation. Separate CAM6 simulations reducing the dependence of sea salt emissions on wind speed and increasing surface DMS emissions are conducted to provide insight into previously reported biases in CAM6 simulations of N_{CCN}, including over-prediction in sea-salt dominated regions and under-prediction in sulfate dominated regions. The following conclusions are noted:

- Reducing the wind speed dependence of sea salt emission alone make simulated N_{CCN} at SS_w of 0.2% and 0.5% more consistent with observations, especially over the 50-55°S region. This finding aligns with conclusions from Niu et al. (2024) and Humphries et al. (2022), who respectively emphasized the role of primary CCN sources and their sensitivity to wind over the windier northern SO.
- In contrast, increasing surface DMS emissions enhances N_{CCN} at SS_w of 0.2% and 0.5%, primarily south of 55°S, consistent with higher observed sulfate contributions in this region, as reported by Humphries et al. (2021), and with the lower observed CCN hygroscopicity described in Niu et al. (2024, 2025).
- The test $U_{10}^{2.8}$+ DMS × 3 effectively reduces the N_d mode over 50–55°S and increases it south of 55°S, resulting in improved agreement with observations, particularly during the MCB events. These changes are consistent with the N_{CCN} representation more consistent with observations achieved through the updated emission treatments.
- The upscaling of DMS in the model results in better agreement of accumulation mode (Ac) aerosols and CCN, vertically and chemically, with observations, during the summer of 2018. However, the agreement varies in different scenarios. CAPRICORN data indicates the observed mass of sulfates can be 2-3 times of that from the base-run. MARCUS data shows by the Antarctic coast, sometimes DMS×3 still underestimates the $N_{CCN,0.2}$ and $N_{CCN,0.5}$ peaks. The SOCRATES data show that the vertical distribution of simulated Ac is more consistent with observations when DMS is increased by a scale of 2 rather than 3.
- The various efficiency of sulfate booming may be related to the absolute values of DMS emission map, new sulfate particle formation scheme, additional pathways of chemical species, transportation of sulfates and their precursors dominated by atmosphere

circulation, regional biased CCN sinks, and other factors. This study used a simple method to strike a new balance between the primary and secondary CCN by updating surface emission and improving the agreement of simulated SO N_d and reflected solar radiation with observations. Future studies can investigate the observed aerosol chemical composition and its precursors within the context of summer latitudinal variation, observations not available during the 2018 summer field campaigns, and apply this to future simulation developments and diagnosis.

- Although the observationally based modifications reported here are specific to CAM6, the physical basis related to these modifications are universal and hence the process-based understanding gained here provides insight to all ESMs.

5. Conclusions and Discussion

This dissertation builds upon the analysis of Southern Ocean (SO) Cloud Condensation Nuclei (CCN) presented in (2021) and Niu et al. (2024). That study illustrates that 62°S witnessed a transition of the boundary layer marine aerosol pattern over the SO (50°S–68°S, 63°E– 150°E) during the 2017-2018 spring and summer. The North SO (NSO) showed more signals of primary CCN-active aerosols with D > 700 nm, while the South SO (SSO, south of 62°S) showed signals from substantial secondary CCN-active aerosols with 60 nm < D < 100 nm. This shift of pattern is analyzed in this dissertation under the context of the dynamic circulation over the SO, its seasonality, and its proximity to extratropical cyclones in Chapter 2. It is shown that the increased N_{CCN} over the SSO in the summer (January - February 2018) is related to the aging processes above the Marine Boundary Layer (MBL) over the Antarctic continent. And the Recent Particle Formation (RPF) events and the consequential Aitken-mode aerosols are more frequently observed during the spring (2017 November) over the NSO and further north. Based on both Hysplit4 back trajectories and the observed ozone mixing ratio values, these RPF events can potentially happen in the MBL. The observations are consistent with the hypothesis that Aitken mode aerosols from gas-to-particle transition form during the spring within the MBL but get transported either to the south over the SSO or to the north over 40°S -50°S above the MBL. These aging and growth processes in the free troposphere result in the formation of aerosols with D <100 nm, which are transported to the surface along the circulation.

Given observations only show the patterns of aerosol and CCN variation but not the processes that cause these variation, numerical modeling is used to potentially provide more insights into the physical and chemical mechanisms responsible for these variations. Chapter 3 discusses a nudged

run using the CAM6 model during the MARCUS period. It shows the bias of simulated CCN varies north and south of 55°S. According to the N_{CCN} -SS spectra, the overestimation of sea salts is consistent with the overestimated N_{CCN} north of 55°S, while the underestimation of sulfates is consistent with the underestimated N_{CCN} south of 55°S. The N_{CCN} -SS spectra also demonstrates that the hygroscopicity of the N_{CCN} over sea ice is overestimated in the model. Therefore, two types of modifications are applied to CAM6 to improve the agreement of N_{CCN} between the observations and simulations. Doubling the open water dimethyl sulfide (DMS, CH3SCH3) emission flux and updating the power law coefficient of wind speed dependence from 3.41 to 2.8 shows the best agreement between observed N_{CCN} and simulated N_{CCN} for MARCUS. This also leads to better agreement between the simulated and surface-retrieved cloud droplet number concentration (N_d) from the mode of 40 cm^{-3} to 100 cm^{-3}, resulting in more reflective clouds along the Antarctic coast with an extra 5~12 W m^{-2} cloud shortwave forcing back to space.

Two ongoing studies related to this dissertation include 1) to discover the physical and chemical processes of sulfates aging and growth over the SO within the context of dynamic circulation using updated CAM6 chemistry including Methanethiol (MeSH, CH_3SH) and Hydroxymethyl Thioformate (HTMPF), 2) aerosol hygroscopicity analysis of aged and fresh anvils, and 3) to analyze the SO boundary layer clouds properties using similar methods as in Chapter 2 for the aerosol-cloud-interaction study.

6. References

Abdul-Razzak, H., & Ghan, S. J. (2000). A parameterization of aerosol activation: 2. Multiple aerosol types. *Journal of Geophysical Research*, 105(D5), 6837–6844. https://doi.org/10.1029/1999JD901161

Albert, M. F. M. A., Anguelova, M. D., Manders, A. M. M., Schaap, M., & de Leeuw, G. (2016). Parameterization of oceanic whitecap fraction based on satellite observations. *Atmospheric Chemistry and Physics*, 16(21), 13725–13751. https://doi.org/10.5194/acp-16-13725-2016

Alinejadtabrizi, T., Huang, Y., Lang, F., Siems, S., Manton, M., Ackermann, L., et al. (2024). Contributions of the synoptic meteorology to the seasonal CCN cycle over the Southern Ocean. *EGUsphere*, 2024, 1–24. https://doi.org/10.5194/egusphere-2024-2397

Alroe, J. *et al.* (2020) 'Marine productivity and synoptic meteorology drive summertime variability in Southern Ocean aerosols', *Atmospheric Chemistry and Physics*, 20(13), pp. 8047–8062. Available at: https://doi.org/10.5194/acp-20-8047-2020

Andreae, M.O. (2009) 'Correlation between cloud condensation nuclei concentration and aerosol optical thickness in remote and polluted regions', *Atmospheric Chemistry and Physics*, 9(2), pp. 543–556. Available at: https://doi.org/10.5194/acp-9-543-2009

Ayers, G.P. and Cainey, J.M. (2007) 'The CLAW hypothesis: A review of the major developments', *Environmental Chemistry*, 4(6), pp. 366–374. Available at: https://doi.org/10.1071/en07080

Ayers, G.P. and Gras, J.L. (1991) 'Seasonal relationship between cloud condensation nuclei and aerosol methanesulphonate in marine air', *Nature*, 353, pp. 834–835. Available at: https://doi.org/10.1038/353834a0

Bodas-Salcedo, A., Williams, K. D., Ringer, M. A., Beau, I., Cole, J. N. S., Dufresne, J. L., et al. (2014). Origins of the Solar Radiation Biases over the Southern Ocean in CFMIP2 Models. *Journal of Climate*, 27(1), 41–56. https://doi.org/10.1175/JCLI-D-13-00169.1

Bogenschutz, P. A., Gettelman, A., Hannay, C., Larson, V. E., Neale, R. B., Craig, C., & Chen, C. C. (2018). The path to CAM6: Coupled simulations with CAM5.4 and CAM5.5. *Geoscientific Model Development*, 11(1), 235–255. https://doi.org/10.5194/GMD-11-235-2018

Bourgeois, I., Peischl, J., Thompson, C. R., Aikin, K. C., Campos, T., Clark, H., Commane, R., Daube, B., Diskin, G. W., Elkins, J. W., Gao, R.-S., Gaudel, A., Hintsa, E. J., Johnson, B. J., Kivi, R., McKain, K., Moore, F. L., Parrish, D. D., Querel, R., Ray, E., Sánchez, R., Sweeney, C., Tarasick, D. W., Thompson, A. M., Thouret, V., Witte, J. C., Wofsy, S. C., & Ryerson, T. B. (2020). Global-scale distribution of ozone in the remote troposphere from the ATom and HIPPO airborne field missions. *Atmospheric Chemistry and Physics*, 20, 10611–10635. https://doi.org/10.5194/acp-20-10611-2020

Cala, B. A., Archer-Nicholls, S., Weber, J., Abraham, N. L., Griffiths, P. T., Jacob, L., Shin, Y. M., Revell, L. E., Woodhouse, M., & Archibald, A. T. (2023). Development, intercomparison, and evaluation of an improved mechanism for the oxidation of dimethyl sulfide in the UKCA model. *Atmospheric Chemistry and Physics*, 23, 14735–14760. https://doi.org/10.5194/acp-23-14735-2023

Charlson, R. J., Lovelock, J. E., Andreae, M. O., & Warren, S. G. (1987). Oceanic phytoplankton, atmospheric sulphur, cloud albedo and climate. *Nature*, 326(6114), 655–661. https://doi.org/10.1038/326655a0

Chen, Q., Sherwen, T., Evans, M., & Alexander, B. (2018). DMS oxidation and sulfur aerosol formation in the marine troposphere: A focus on reactive halogen and multiphase chemistry. *Atmospheric Chemistry and Physics*, 18(18), 13617–13637. https://doi.org/10.5194/acp-18-13617-2018

Clarke, A. D., Varner, J. L., Eisele, F., Mauldin, R. L., Tanner, D., & Litchy, M. (1998). Particle production in the remote marine atmosphere. *Journal of Geophysical Research*, 103(D13), 16397–16409. https://doi.org/10.1029/97JD02987

Clarke, A. D., Owens, S. R., & Zhou, J. (2006). An ultrafine sea salt flux from breaking waves. *Journal of Geophysical Research: Atmospheres*, 111(D6), D06202. https://doi.org/10.1029/2005JD006565

Cala, B. A., Archer-Nicholls, S., Weber, J., Abraham, N. L., Griffiths, P. T., Jacob, L., Shin, Y. M., Revell, L. E., Woodhouse, M., & Archibald, A. T. (2023). Development, intercomparison, and evaluation of an improved mechanism for the oxidation of dimethyl sulfide in the UKCA model. *Atmospheric Chemistry and Physics*, 23, 14735–14760. https://doi.org/10.5194/acp-23-14735-2023

Charlson, R. J., Lovelock, J. E., Andreae, M. O., & Warren, S. G. (1987). Oceanic phytoplankton, atmospheric sulphur, cloud albedo and climate. *Nature*, 326(6114), 655–661. https://doi.org/10.1038/326655a0

Chen, Q., Sherwen, T., Evans, M., & Alexander, B. (2018). DMS oxidation and sulfur aerosol formation in the marine troposphere: A focus on reactive halogen and multiphase chemistry. *Atmospheric Chemistry and Physics*, 18(18), 13617–13637. https://doi.org/10.5194/acp-18-13617-2018

Clarke, A. D., Varner, J. L., Eisele, F., Mauldin, R. L., Tanner, D., & Litchy, M. (1998). Particle production in the remote marine atmosphere. *Journal of Geophysical Research*, 103(D13), 16397–16409. https://doi.org/10.1029/97JD02987

Clarke, A. D., Owens, S. R., & Zhou, J. (2006). An ultrafine sea salt flux from breaking waves. *Journal of Geophysical Research: Atmospheres*, 111(D6), D06202. https://doi.org/10.1029/2005JD006565

Dong, S., Sprintall, J., & Gille, S. T. (2006). Location of the Antarctic Polar Front from AMSR-E satellite sea surface temperature measurements. *Journal of Physical Oceanography*, 36(11), 2075–2089. https://doi.org/10.1175/JPO2973.1

Emmons, L. K., Walters, S., Hess, P. G., Lamarque, J.-F., Pfister, G. G., Fillmore, D., et al. (2010). Description and evaluation of the model for ozone and related chemical tracers, version 4

(MOZART-4). *Geoscientific Model Development*, 3(1), 43–67. https://doi.org/10.5194/gmd-3-43-2010

Feng, L., Smith, S. J., Braun, C., Crippa, M., Gidden, M. J., Hoesly, R., et al. (2020). The generation of gridded emissions data for CMIP6. *Geoscientific Model Development*, 13(2), 461–482. https://doi.org/10.5194/gmd-13-461-2020

Fiddes, S. L., Protat, A., Mallet, M. D., Alexander, S. P., & Woodhouse, M. T. (2022). Southern Ocean cloud and shortwave radiation biases in a nudged climate model simulation: Does the model ever get it right? *Atmospheric Chemistry and Physics*, 22(22), 14603–14630. https://doi.org/10.5194/acp-22-14603-2022

Fossum, K., et al. (2018). Summertime primary and secondary contributions to Southern Ocean cloud condensation nuclei. *Scientific Reports*, 8. https://doi.org/10.1038/s41598-018-32047-4

Fung, K. M., Heald, C. L., Kroll, J. H., Wang, S., Jo, D. S., Gettelman, A., et al. (2022). Exploring dimethyl sulfide (DMS) oxidation and implications for global aerosol radiative forcing. *Atmospheric Chemistry and Physics*, 22(2), 1549–1573. https://doi.org/10.5194/acp-22-1549-2022

Gettelman, A., & Morrison, H. (2015). Advanced two-moment bulk microphysics for global models. Part I: Off-line tests and comparison with other schemes. *Journal of Climate*, 28(3), 1268–1287. https://doi.org/10.1175/JCLI-D-14-00102.1

Gettelman, A., Bardeen, C. G., McCluskey, C. S., Järvinen, E., Stith, J., Bretherton, C., et al. (2020). Simulating observations of Southern Ocean clouds and implications for climate. *Journal of Geophysical Research: Atmospheres*, 125(21), e2020JD032619. https://doi.org/10.1029/2020JD032619

Ghan, S. J., Guzman, G., & Abdul-Razzak, H. (1998). Competition between sea salt and sulfate particles as cloud condensation nuclei. *Journal of the Atmospheric Sciences*, 55(22), 3340–3347. https://doi.org/10.1175/1520-0469(1998)055<3340:CBSSAS>2.0.CO;2

Golaz, J., Larson, V. E., & Cotton, W. R. (2002). A PDF-based model for boundary layer clouds. Part II: Model results. *Journal of the Atmospheric Sciences*, 59(24), 3552–3571. https://doi.org/10.1175/1520-0469(2002)059<3552:APBMFB>2.0.CO;2

Golaz, J. C. (2002). A PDF-based parameterization for boundary layer clouds. Colorado State University.

Gong, S. L., Barrie, L. A., Prospero, J. M., Savoie, D. L., Ayers, G. P., Blanchet, J.-P., & Spacek, L. (1997). Modeling sea salt aerosols in the atmosphere: 2. Atmospheric concentrations and fluxes. *Journal of Geophysical Research: Atmospheres*, 102(D3), 3819–3830. https://doi.org/10.1029/96JD03401

Gong, S. L. (2003). A parameterization of sea salt aerosol source function for sub- and super-micron particles. *Global Biogeochemical Cycles*, 17(4), 1097. https://doi.org/10.1029/2003GB002079

Gong, X., Zhang, J., Croft, B., Yang, X., Frey, M. M., Bergner, N., et al. (2023). Arctic warming by abundant fine sea salt aerosols from blowing snow. *Nature Geoscience*, 16(9), 768–774. https://doi.org/10.1038/s41561-023-01254-8

Hamilton, D. S., Lee, L. A., Pringle, K. J., Reddington, C. L., Spracklen, D. V., & Carslaw, K. S. (2014). Occurrence of pristine aerosol environments on a polluted planet. *Proceedings of the National Academy of Sciences*, 111(52), 18466–18471. https://doi.org/10.1073/pnas.1415440111

Hartery, S., Toohey, D. W., Revell, L., Sellegri, K., Kuma, P., Harvey, M., & McDonald, A. J. (2020). Constraining the surface flux of sea spray particles from the Southern Ocean. *Journal of Geophysical Research: Atmospheres*, 125, e2019JD032026. https://doi.org/10.1029/2019JD032026

Hoose, C., Kristjánsson, J. E., Iversen, T., Kirkevåg, A., Seland, Ø., & Gettelman, A. (2009). Constraining cloud droplet number concentration in GCMs suppresses the aerosol indirect effect. *Geophysical Research Letters*, 36, L12807. https://doi.org/10.1029/2009GL038568

Hopkins, F. E., Archer, S. D., Bell, T. G., Suntharalingam, P., & Todd, J. D. (2023). The biogeochemistry of marine dimethyl sulfide. *Nature Reviews Earth & Environment*, 4(6), 361–376. https://doi.org/10.1038/s43017-023-00428-7

Huang, Y., Siems, S. T., Manton, M. J., Protat, A., & Delanoë, J. (2012). A study on low altitude clouds over the Southern Ocean using DARDAR. *Journal of Geophysical Research: Atmospheres*, 117, D18204. https://doi.org/10.1029/2012JD017800

Hudson, J. G., Noble, S., & Jha, V. (2011). On the relative role of sea salt cloud condensation nuclei (CCN). *Journal of Atmospheric Chemistry*, 68(1), 71–88. https://doi.org/10.1007/s10874-011-9210-5

Humphries, R. S., et al. (2015). Boundary layer new particle formation over east Antarctic sea ice. *Atmospheric Chemistry and Physics*, 15(23), 13339–13364. https://doi.org/10.5194/acp-15-13339-2015

Humphries, R., Keywood, M., Gribben, S., McRobert, I., Ward, J., Selleck, P., et al. (2021). Southern Ocean latitudinal gradients of cloud condensation nuclei. *Atmospheric Chemistry and Physics*, 21, 1–35. https://doi.org/10.5194/acp-2020-1246

Intergovernmental Panel on Climate Change (IPCC) (2014) 'Evaluation of climate models', in *Climate Change 2013: The Physical Science Basis*, pp. 741–866. Available at: https://doi.org/10.1017/CBO9781107415324.020

Intergovernmental Panel on Climate Change (IPCC) (2023) *Climate change 2023: Synthesis report*, in Lee, H. and Romero, J. (eds.), pp. 35–115. Available at: https://doi.org/10.59327/IPCC/AR6-9789291691647

Jo, D. S., Tilmes, S., Emmons, L. K., Wang, S., & Vitt, F. (2023). A new simplified parameterization of secondary organic aerosol in the Community Earth System Model Version 2 (CESM2; CAM6.3). *Geoscientific Model Development*, 16(13), 3893–3906. https://doi.org/10.5194/gmd-16-3893-2023

Johnson, M. T. (2010). A numerical scheme to calculate temperature and salinity dependent air–water transfer velocities for any gas. *Ocean Science*, 6(4), 913–932. https://doi.org/10.5194/os-6-913-2010

Jongebloed, U. A., Chalif, J. I., Tashmim, L., Porter, W. C., Bates, K. H., Chen, Q., Osterberg, E. C., Koffman, B. G., Cole-Dai, J., Winksi, D. A., Ferris, D. G., Kreutz, K. J., Wake, C. P., & Alexander, B. (2024). Dimethyl sulfide chemistry over the industrial era: comparison of key oxidation mechanisms and long-term observations. *EGUsphere*. https://doi.org/10.5194/egusphere-2024-3026

Kanaya, Y., Miyazaki, K., Taketani, F., Miyakawa, T., Takashima, H., Komazaki, Y., Pan, X., Kato, S., Sudo, K., Sekiya, T., Inoue, J., Sato, K., & Oshima, K. (2019). Ozone and carbon monoxide observations over open oceans on R/V Mirai from 67°S to 75°N during 2012–2017. *Atmospheric Chemistry and Physics*, 19, 7233–7254. https://doi.org/10.5194/acp-19-7233-2019

Kang, L., Marchand, R. T., Wood, R., & McCoy, I. L. (2022). Coalescence scavenging drives droplet number concentration in Southern Ocean low clouds. *Geophysical Research Letters*, 49(7), e2022GL097819. https://doi.org/10.1029/2022GL097819

Kang, L., Marchand, R., Ma, P.-L., Huang, M., Wood, R., Jongebloed, U., & Alexander, B. (2025). Impacts of DMS emissions and chemistry on E3SMv2 simulated cloud droplet numbers and aerosol concentrations over the Southern Ocean. *Journal of Advances in Modeling Earth Systems*, 17, e2024MS004683. https://doi.org/10.1029/2024MS004683

Kaufman, Y. J., & Tanré, D. (1994). Effect of variations in supersaturation on the formation of cloud condensation nuclei. *Nature*, 369(6475), 45–48. https://doi.org/10.1038/369045a0

Kay, J. E., et al. (2016). Global climate impacts of fixing the Southern Ocean shortwave radiation bias in CESM. *Journal of Climate*, 29(12), 4617–4636. https://doi.org/10.1175/JCLI-D-15-0358.1

Köhler, H. (1936). The nucleus in and the growth of hygroscopic droplets. *Transactions of the Faraday Society*, 32, 1152–1161. https://doi.org/10.1039/TF9363201152

Koren, I., Dagan, G., & Altaratz, O. (2014). From aerosol-limited to invigoration of warm convective clouds. *Science*, 344(6188), 1143–1146. https://doi.org/10.1126/science.1252595

Lachlan-Cope, T., et al. (2020). Annual variability of Antarctic aerosol size distributions at Halley Research Station. *Atmospheric Chemistry and Physics*, 20(7), 4461–4476. https://doi.org/10.5194/acp-20-4461-2020

Larson, V. E., & Golaz, J. C. (2005). Using probability density functions to derive consistent closure relationships among higher-order moments. Monthly Weather Review, 133(4), 1023–1042. https://doi.org/10.1175/mwr2902.1

Lang, F., Huang, Y., Siems, S. T., & Manton, M. J. (2018). Characteristics of the marine atmospheric boundary layer over the Southern Ocean. *Journal of Geophysical Research: Atmospheres*, 123(15), 7799–7820. https://doi.org/10.1029/2018JD028700

Lee, L. A., Pringle, K. J., Reddington, C. L., Mann, G. W., Stier, P., Spracklen, D. V., et al. (2013). The magnitude and causes of uncertainty in global model simulations of cloud condensation nuclei. *Atmospheric Chemistry and Physics*, 13, 8879–8914. https://doi.org/10.5194/acp-13-8879-2013

Liu, X., Ma, P. L., Wang, H., Tilmes, S., Singh, B., Easter, R. C., et al. (2016). Description and evaluation of a new four-mode version of the modal aerosol module (MAM4) within version 5.3 of the community atmosphere model. *Geoscientific Model Development*, 9(2), 505–522. https://doi.org/10.5194/gmd-9-505-2016

Mace, G. G. (2010). Cloud properties and radiative forcing over Southern Ocean storm tracks. *Journal of Geophysical Research: Atmospheres*, 115(D10). https://doi.org/10.1029/2009JD012517

Mace, G. G., Protat, A., Humphries, R. S., Alexander, S. P., McRobert, I. M., Ward, J., et al. (2021). Southern Ocean cloud properties derived from CAPRICORN and MARCUS data. *Journal of Geophysical Research: Atmospheres*, 126, e2020JD033368. https://doi.org/10.1029/2020JD033368

Mace, G. G., Benson, S., Humphries, R., Gombert, P. M., & Sterner, E. (2023). Natural marine cloud brightening in the Southern Ocean. *Atmospheric Chemistry and Physics*, 23(2), 1677–1685. https://doi.org/10.5194/acp-23-1677-2023

Mace, G. G., Benson, S., Sterner, E., Protat, A., Humphries, R., & Hallar, A. G. (2024). Association between cloud droplet number and air mass history over the Southern Ocean. *Journal of Geophysical Research: Atmospheres*, 129, e2023JD040673. https://doi.org/10.1029/2023JD040673

Mace, G. G. (2024). Deriving cloud droplet number concentration from surface-based remote sensing. *Atmospheric Measurement Techniques*, 17, 3679–3695. https://doi.org/10.5194/amt-17-3679-2024

Mallet, M. D., Humphries, R. S., Fiddes, S. L., Alexander, S. P., Altieri, K., Angot, H., et al. (2023). Untangling the influence of Antarctic and Southern Ocean life on clouds. Elementa: Science of the Anthropocene, 11(1), 1. https://doi.org/10.1525/ELEMENTA.2022.00130

Maier-Reimer, E. (1984). Towards a global ocean carbon model. In *Interactions between climate and biosphere* (pp. 295–310). Swets & Zeitlinger.

Maier-Reimer, E., & Hasselmann, K. (1987). Transport and storage of CO_2 in the ocean—An inorganic ocean-circulation carbon cycle model. *Climate Dynamics, 2*, 63–90.

Mallet, M. D., Humphries, R. S., Fiddes, S. L., Alexander, S. P., Altieri, K., Angot, H., et al. (2023). Untangling the influence of Antarctic and Southern Ocean life on clouds. *Elementa: Science of the Anthropocene, 11*(1), 1. https://doi.org/10.1525/elementa.2022.00130

Matus, A. V., & L'Ecuyer, T. S. (2017). The role of cloud phase in Earth's radiation budget. *Journal of Geophysical Research: Atmospheres, 122*(5), 2559–2578. https://doi.org/10.1002/2016JD025951

McCluskey, C. S., Gettelman, A., Bardeen, C. G., DeMott, P. J., Moore, K. A., Kreidenweis, S. M., et al. (2023). Simulating Southern Ocean Aerosol and Ice Nucleating Particles in the Community Earth System Model Version 2. *Journal of Geophysical Research: Atmospheres*, 128(8). https://doi.org/10.1029/2022JD036955

McCoy, D. T., D. L. Hartmann, and D. P. Grosvenor, 2014: Observed Southern Ocean cloud properties and shortwave reflection. part ii: Phase changes and low cloud feedback. *Journal of Climate*, 27 (23), 8858 – 8868, doi:10.1175/JCLI-D-14-00288.1.

McCoy, D. T., Burrows, S. M., Wood, R., Grosvenor, D. P., Elliott, S. M., Ma, P.-L., et al. (2015). Natural aerosols explain seasonal and spatial patterns of Southern Ocean cloud albedo. *Science Advances, 1*(6), e1500157. https://doi.org/10.1126/sciadv.1500157

McCoy, I. L., Bretherton, C. S., Wood, R., Twohy, C. H., Gettelman, A., Bardeen, C. G., & Toohey, D. W. (2021). Influences of recent particle formation on Southern Ocean aerosol variability and low cloud properties. Journal of Geophysical Research: Atmospheres, 126(8), e2020JD033529. https://doi.org/10.1029/2020JD033529

McFarquhar, G. M., Bretherton, C. S., Marchand, R., Protat, A., DeMott, P. J., Alexander, S. P., et al. (2021). Observations of Clouds, Aerosols, Precipitation, and Surface Radiation over the Southern Ocean: An Overview of CAPRICORN, MARCUS, MICRE, and SOCRATES. Bulletin of the American Meteorological Society, 102(4), E894–E928. https://doi.org/10.1175/BAMS-D-20-0132.1

McFarquhar, G. M. (2022). Rainfall microphysics. In R. Morbidelli (Ed.), Rainfall. Modeling, measurement and Applications, Amsterdam, 2022 (pp. 1–26). Elsevier. https://doi.org/10.1016/B978-0-12-822544-8.00009-3

McInnes, L. M., D. S. Covert, P. K. Quinn, and M. S. Germani (1994), Measurements of chloride depletion and sulfur enrichment in individual sea-salt particles collected from the remote marine boundary layer, *J. Geophys. Res.*, 99(D4), 8257–8268, doi:10.1029/93JD03453.

Mechem, D. B., Robinson, P. C., & Kogan, Y. L. (2006). Processing of cloud condensation nuclei by collision-coalescence in a mesoscale model. *Journal of Geophysical Research*, 111(D18). https://doi.org/10.1029/2006jd007183

Medeiros, B., Shaw, J., Kay, J. E., & Davis, I. (2023). Assessing clouds using satellite observations through three generations of global atmosphere models. *Earth and Space Science*, 10, e2023EA002918.

Mulcahy, J. P., Jones, C., Sellar, A., Johnson, B., Boutle, I. A., Jones, A., et al. (2018). Improved aerosol processes and effective radiative forcing in HadGEM3 and UKESM1. Journal of Advances in Modeling Earth Systems, 10, 2786–2805. https://doi.org/10.1029/2018MS001464

Monahan, E. C. (1986). The ocean as a source for atmospheric particles. In P. Buat-Ménard (Ed.), *The role of air-sea exchange in geochemical cycling* (pp. 129–163). Springer Netherlands. https://doi.org/10.1007/978-94-009-4738-2_6

Montoya Duque, E., Huang, Y., Siems, S. T., May, P. T., Protat, A., & McFarquhar, G. M. (2022). A characterization of clouds and precipitation over the Southern Ocean from synoptic to micro scales during the CAPRICORN field campaigns. *Journal of Geophysical Research: Atmospheres*,127(17), e2022JD036796. https://doi.org/10.1029/2022jd036796

Naud, C.M., A. D. Del Genio, M. Bauer, and W. Kovari, 2010: Cloud vertical distribution across warm and cold fronts in CloudSat-CALIPSO data and a general circulation model. *J. Climate*, 23, 3397–3415.

Naud, C. M., Booth, J. F., & Del Genio, A. D. (2014). Evaluation of ERA-Interim and MERRA cloudiness in the Southern Ocean. *Journal of Climate, 27*(5), 2109–2124. https://doi.org/10.1175/JCLI-D-13-00432.1

Niu, Q. (2021). 60°S-62°S Witnessed a Shift Pattern of Southern Ocean Boundary Layer Aerosols and CCN. SHAREOK. https://shareok.org/handle/11244/12345

Niu, Q. (2025). MARCUS Clouds and CCN data with CAM6 simulation co-location [Data set]. Zenodo. https://doi.org/10.5281/zenodo.16059627

Niu, Q., McFarquhar, G. M., Marchand, R., Theisen, A., Cavallo, S. M., Flynn, C., et al. (2024). 62°S witnesses the transition of boundary-layer marine aerosol patterns over the Southern Ocean (50°S–68°S, 63°E–150°E) during spring and summer: Results from MARCUS (I). *Journal of Geophysical Research: Atmospheres, 129*(9), e2023JD040396. https://doi.org/10.1029/2023JD040396

Niu, Q., McCluskey, C., & McFarquhar, G. M. (2025). Marine boundary layer cloud condensation nuclei bias over the Southern Ocean: Comparisons between the Community Atmosphere Model 6 and field observations. *Journal of Geophysical Research: Atmospheres, 130*, e2024JD042734. https://doi.org/10.1029/2024JD042734

Nightingale, P. D., Malin, G., Law, C. S., Watson, A. J., Liss, P. S., Liddicoat, M. I., Boutin, J., & Upstill-Goddard, R. C. (2000). *Global Biogeochemical Cycles, 14*(1), 373–387. In situ evaluation of air-sea gas-exchange parameterizations using novel conservative and volatile tracers. https://doi.org/10.1029/1999GB900091

O'Dowd, C. D., M. H. Smith, I. E. Consterdine, and J. A. Lowe, 1997: Marine aerosol, sea-salt, and the marine sulphur cycle: a short review. Atmospheric Environment, 31 (1), 73–80, doi: https://doi.org/10.1016/S1352-2310(96)00106-9.

O'Dowd, C. D., Smith, M. H., Consterdine, I. E., & Lowe, J. A. (1997). Marine aerosol, sea-salt, and the marine sulphur cycle: A short review. *Atmospheric Environment*, 31(1), 73–80. https://doi.org/10.1016/S1352-2310(96)00106-9

Petters, M. D., & Kreidenweis, S. M. (2007). A single parameter representation of hygroscopic growth and cloud condensation nucleus activity. *Atmospheric Chemistry and Physics*, 7(8), 1961–1971. https://doi.org/10.5194/acp-7-1961-2007

Pruppacher, H. R., and J. D. Klett, 1997: Microphysics of Clouds and Precipitation. *Kluwer Academic Publisher*, ch.17 pp.

Quinn, P. K., Bates, T. S., Schulz, K. S., Coffman, D. J., Frossard, A. A., Russell, L. M., et al. (2014). Contribution of sea surface carbon pool to organic matter enrichment in sea spray aerosol. *Nature Geoscience*, 7(3), 228–232. https://doi.org/10.1038/ngeo2092

Quinn, P., D. Coffman, J. Johnson, L. Upchurch, and T. Bates, 2017: Small fraction of marine cloud condensation nuclei made up of sea spray aerosol. *Nature Geoscience*, 10 (9), 674–679.

Revell, L. E., Kremser, S., Hartery, S., Harvey, M., Mulcahy, J. P., Williams, J., Morgenstern, O., McDonald, A. J., Varma, V., Bird, L., & Schuddeboom, A. (2019). The sensitivity of Southern Ocean aerosols and cloud microphysics to sea spray and sulfate aerosol production in the HadGEM3-GA7.1 chemistry–climate model. *Atmospheric Chemistry and Physics, 19*, 15447–15466. https://doi.org/10.5194/acp-19-15447-2019

Riihimaki, L., Riihimaki, L., Zhang, D., & Zhang, D. *Planetary* Boundary Layer Height (PBLHTSONDE1MCFARL), 2017-10-31 to 2018-03-24, ARM Mobile Facility (MAR), Hobart, AUS to Antarctic Coast - resupply ship Aurora Australis; AMF2 (M1). Atmospheric Radiation Measurement (ARM) User Facility. https://doi.org/10.5439/1991783

Russell, L. M., Moore, R. H., Burrows, S. M., & Quinn, P. K. (2023). Ocean flux of salt, sulfate, and organic components to atmospheric aerosol. Earth-Science Reviews, 239, 104364. https://doi.org/10.1016/j.earscirev.2023.104364

Sanchez, K. J., Chen, C.-L., Russell, L. M., Betha, R., Liu, J., Price, D. J., et al. (2018). Substantial seasonal contribution of observed biogenic sulfate particles to cloud condensation nuclei. Scientific Reports, 8(1), 3235. https://doi.org/10.1038/s41598-018-21590-9

Sanchez, K. J., Roberts, G. C., Saliba, G., Russell, L. M., Twohy, C., Reeves, M. J., et al. (2021). Measurement report: Cloud processes and the transport of biological emissions affect Southern Ocean particle and cloud condensation nuclei concentrations. Atmospheric Chemistry and Physics, 21(5), 3427–3446. https://doi.org/10.5194/ACP-21-3427-2021

Schmale, J., and Coauthors, 2019: Overview of the Antarctic circumnavigation expedition: Study of preindustrial-like aerosols and their climate effects (ace-space). *Bulletin of the American Meteorological Society*, 100 (11), 2260 – 2283, doi:10.1175/BAMS-D-18-0187.1.

Schwartz, S. E. (1996). The whitehouse effect—Shortwave radiative forcing of climate by anthropogenic aerosols: An overview. *Journal of Aerosol Science*, 27(3), 359–382. https://doi.org/10.1016/0021-8502(95)00533-1

Seinfeld, J. H., Bretherton, C., Carslaw, K. S., Coe, H., DeMott, P. J., Dunlea, E. J., et al. (2016). Improving our fundamental understanding of the role of aerosol-cloud interactions in the climate system. Proceedings of the National Academy of Sciences of the United States of America, 113(21), 5781–5790. https://doi.org/10.1073/PNAS.1514043113/SUPPL_FILE/PNAS.201514043SI.PDF

Siems, S. T., Huang, Y., & Manton, M. J. (2022). Southern Ocean precipitation: Toward a process-level understanding. WIREs Climate Change, 13(6), e800. https://doi.org/10.1002/wcc.800

Sim´o, R., and J. Dachs, 2002: Global ocean emission of dimethylsulfide predicted from biogeophysical data. Global Biogeochemical Cycles, 16 (4), 26–1–26–10, doi:https://doi.org/10.1029/2001GB001829

Simmonds, I., & Keay, K. (2000). Mean Southern Hemisphere Extratropical Cyclone Behavior in the 40-Year NCEP–NCAR Reanalysis. *Journal of Climate*, *13*(5), 873-885. https://doi.org/10.1175/1520-0442(2000)013<0873:MSHECB>2.0.CO;2

Stein, A.F., Draxler, R.R, Rolph, G.D., Stunder, B.J.B., Cohen, M.D., and Ngan, F., (2015). NOAA's HYSPLIT atmospheric transport and dispersion modeling system, Bull. Amer. Meteor. Soc., 96, 2059-2077, http://dx.doi.org/10.1175/BAMS-D-14-00110.1

Stuefer, M., Stuefer, M., & Wong, T. (2017). Camera that monitors a site area (CAMSEASTATEMOVIE). Atmospheric Radiation Measurement (ARM) User Facility. https://doi.org/10.5439/1971079

Tan, I., et al. (2016). Observational constraints on mixed-phase clouds imply higher climate sensitivity. *Science, 352*(6282), 224–227. https://doi.org/10.1126/science.aad5300

Tansey, E., Marchand, R., Protat, A., Alexander, S. P., & Ding, S. (2022). Southern Ocean precipitation characteristics observed from CloudSat and ground instrumentation during the Macquarie Island cloud and radiation experiment (MICRE): April 2016 to March 2017. Journal of Geophysical Research: Atmospheres, 127(5), e2021JD035370. https://doi.org/10.1029/2021JD035370

Teng, Z.-J., Qin, Q.-L., Zhang, W., Li, J., Fu, H.-H., Wang, P., et al. (2021). Biogeographic traits of dimethyl sulfide and dimethylsulfoniopropionate cycling in polar oceans. Microbiome, 9(1), 207. https://doi.org/10.1186/s40168-021-01153-3

Thomas, M.A., Devasthale, A. and Kahnert, M. (2022) 'Marine aerosol properties over the Southern Ocean in relation to the wintertime meteorological conditions', Atmospheric Chemistry and Physics, 22, pp. 119–137. Available at: https://doi.org/10.5194/acp-22-119-2022

Tilmes, S., Mills, M. J., Zhu, Y., Bardeen, C. G., Vitt, F., Yu, P., et al. (2023). Description and performance of a sectional aerosol microphysical model in the Community Earth System Model (CESM2). *Geoscientific Model Development*, 16(21), 6087–6125. https://doi.org/10.5194/gmd-16-6087-2023

Trenberth, K. E., & Fasullo, J. T. (2010). Simulation of Present-Day and Twenty-First-Century Energy Budgets of the Southern Oceans. Journal of Climate, 23(2), 440–454. https://doi.org/10.1175/2009JCLI3152.1

Twohy, C. H., DeMott, P. J., Russell, L. M., Toohey, D. W., Rainwater, B., Geiss, R., et al. (2021). Cloud-nucleating particles over the southern ocean in a changing climate. Earth's Future, 9(3), e2020EF001673. https://doi.org/10.1029/2020EF001673

Uetake, J., Hill, T. C. J., Moore, K. A., DeMott, P. J., Protat, A., & Kreidenweis, S. M. (2020). Airborne bacteria confirm the pristine nature of the Southern Ocean boundary layer. *Proceedings of the National Academy of Sciences, 117*(24), 13275–13282. https://doi.org/10.1073/pnas.2000134117

Uin Upton, NY (United States)], J. [Brookhaven N. Lab. (BNL). (2016). Cloud Condensation Nuclei Particle Counter (CCN) Instrument Handbook. United States: ARM Climate Research Facility, Pacific Northwest National Laboratory, Richland, WA. https://doi.org/10.2172/1251411

Uin, J., Aiken, A. C., Dubey, M. K., Kuang, C., Pekour, M., Salwen, C., et al. (2019). Atmospheric Radiation Measurement (ARM) Aerosol Observing Systems (AOS) for Surface-Based In Situ Atmospheric Aerosol and Trace Gas Measurements. Journal of Atmospheric and Oceanic Technology, 36(12), 2429–2447. https://doi.org/10.1175/JTECH-D-19-0077.1

Uin, J., Andrews, E., Enekwizu, O., Hayes, C., & Salwen, C. (2022). Cloud condensation nuclei particle counter (AOSCCN1COLSPECTRA). Atmospheric Radiation Measurement (ARM) User Facility. https://doi.org/10.5439/1342134

Veres, P. R., Neuman, J. A., Bertram, T. H., Assaf, E., Wolfe, G. M., Williamson, C. J., et al. (2020). Global airborne sampling reveals a previously unobserved dimethyl sulfide oxidation mechanism in the marine atmosphere. *Proceedings of the National Academy of Sciences, 117*(9), 4505–4510. https://doi.org/10.1073/pnas.1919344117

Warren, S. G., Hahn, C. H., London, J., Chervin, R. M., & Jenne, R. L. (1988). Global distribution of total cloud cover and cloud type amounts over the ocean (No. DOE/ER-0406; NCAR/TN-317-STR). U.S. Department of Energy. https://doi.org/10.5065/D6QC01D1

Wang, S., Kinnison, D., Montzka, S. A., Apel, E. C., Hornbrook, R. S., Hills, A. J., et al. (2019). Ocean biogeochemistry control on the marine emissions of brominated very short-lived ozone-

depleting substances: A machine-learning approach. *Journal of Geophysical Research: Atmospheres*, 124(22), 12319–12339. https://doi.org/10.1029/2019JD031288

Weisman, M. L., and J. B. Klemp, 1982: The dependence of numerically simulated convective storms on vertical wind shear and buoyancy. *Mon. Wea. Rev*., 110, 504-520.

Westervelt, D. M., Moore, R. H., Nenes, A., & Adams, P. J. (2012). Effect of primary organic sea spray emissions on cloud condensation nuclei concentrations. *Atmospheric Chemistry and Physics*, 12(1), 89–101. https://doi.org/10.5194/acp-12-89-2012

Williams, J., de Reus, M., Krejci, R., Fischer, H., & Ström, J. (2002). Application of the variability-size relationship to atmospheric aerosol studies: Estimating aerosol lifetimes and ages. *Atmospheric Chemistry and Physics*, 2(2), 133–145. https://doi.org/10.5194/acp-2-133-2002

Wohl, C., Hartery, S., von der Weiden-Reinmüller, S.-L., Tesson, S. V. M., Burkart, J., Breitenlechner, M., et al. (2024). Marine emissions of methanethiol increase aerosol cooling in the Southern Ocean. *Science Advances*, *10*, eadq2465. https://doi.org/10.1126/sciadv.adq2465

Wood, R. (2006). Rate of loss of cloud droplets by coalescence in warm clouds. *Journal of Geophysical Research*, 111(D21). https://doi.org/10.1029/2006jd007553

Xu, X., Yin, J., Zhang, X., Xue, H., Gu, H., & Fan, H. (2022). Airborne measurements of cloud condensation nuclei (CCN) vertical structures over Southern China. *Atmospheric Research*, 268, 106012. https://doi.org/10.1016/j.atmosres.2021.106012

Yuan, X., J. Patoux, and C. Li, 2009: Satellite-based midlatitude cyclone statistics over the Southern Ocean: 2. tracks and surface fluxes. *Journal of Geophysical Research: Atmospheres*, 114 (D4), doi: https://doi.org/10.1029/2008JD010874

Zender, C. (2010). CITESEERX. CiteSeerX. https://citeseerx.ist.psu.edu/

Zhao, B., Donahue, N. M., Zhang, K., et al. (2024). Global variability in atmospheric new particle formation mechanisms. *Nature, 631*, 98–105. https://doi.org/10.1038/s41586-024-07547-1

Zhang, G. J., & McFarlane, N. A. (1995). Sensitivity of climate simulations to the parameterization of cumulus convection in the Canadian Climate Centre general circulation model. Atmosphere-Ocean, 33(3), 407–446. https://doi.org/10.1080/07055900.1995.9649539

Zhao, X., Liu, X., Burrows, S. M., & Shi, Y. (2021). Effects of marine organic aerosols as sources of immersion-mode ice-nucleating particles on high-latitude mixed-phase clouds. Atmospheric Chemistry and Physics, 21(4), 2305–2327. https://doi.org/10.5194/acp-21-2305-2021

Zheng, G., Wang, Y., Wood, R. *et al.* New particle formation in the remote marine boundary layer. *Nat Commun* 12, 527 (2021). https://doi.org/10.1038/s41467-020-20773-1

Zhou, X., Atlas, R., McCoy, I. L., Bretherton, C. S., Bardeen, C., Gettelman, A., et al. (2021). Evaluation of Cloud and Precipitation Simulations in CAM6 and AM4 Using Observations Over the Southern Ocean. Earth and Space Science, 8(2), e2020EA001241. https://doi.org/10.1029/2020EA001241

7. Supporting Information (SI)

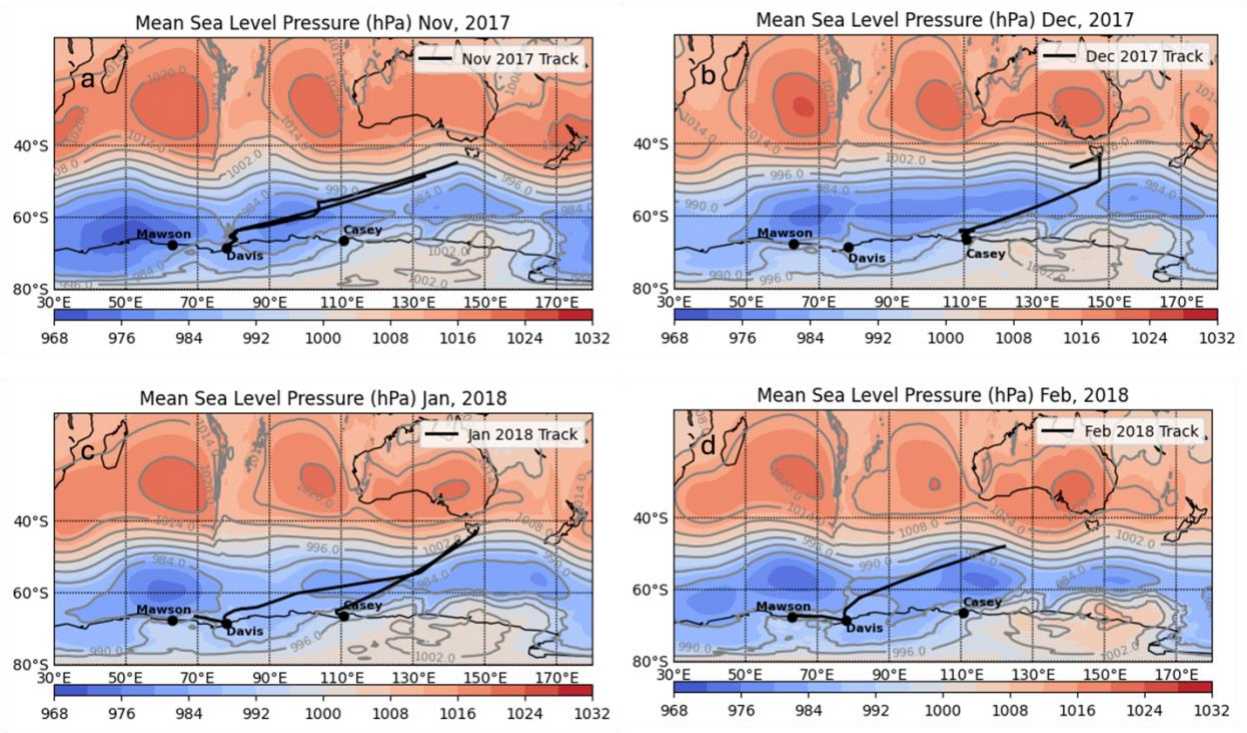

Figure S2.1 Mean sea-level-pressure over the SO between Hobart and the Antarctic Stations during November in a, December in b, January in c, and February in d, with red indicates high pressure and blue indicates low pressure. MARCUS ship tracks are plotted in black each month.

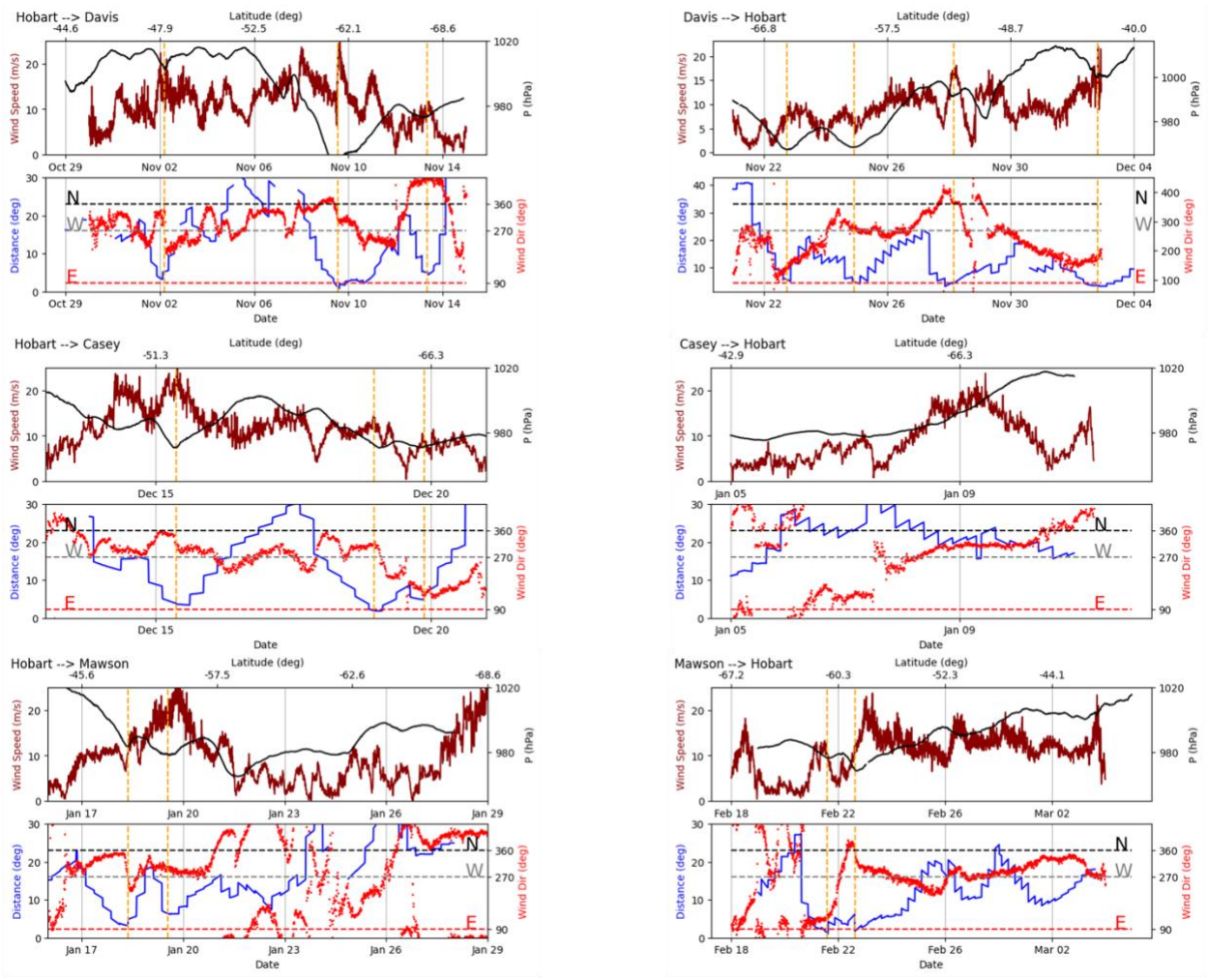

Figure S2.2 Similar to Figure 2.3 but for all the voyages between Hobart and the Antarctic Stations.

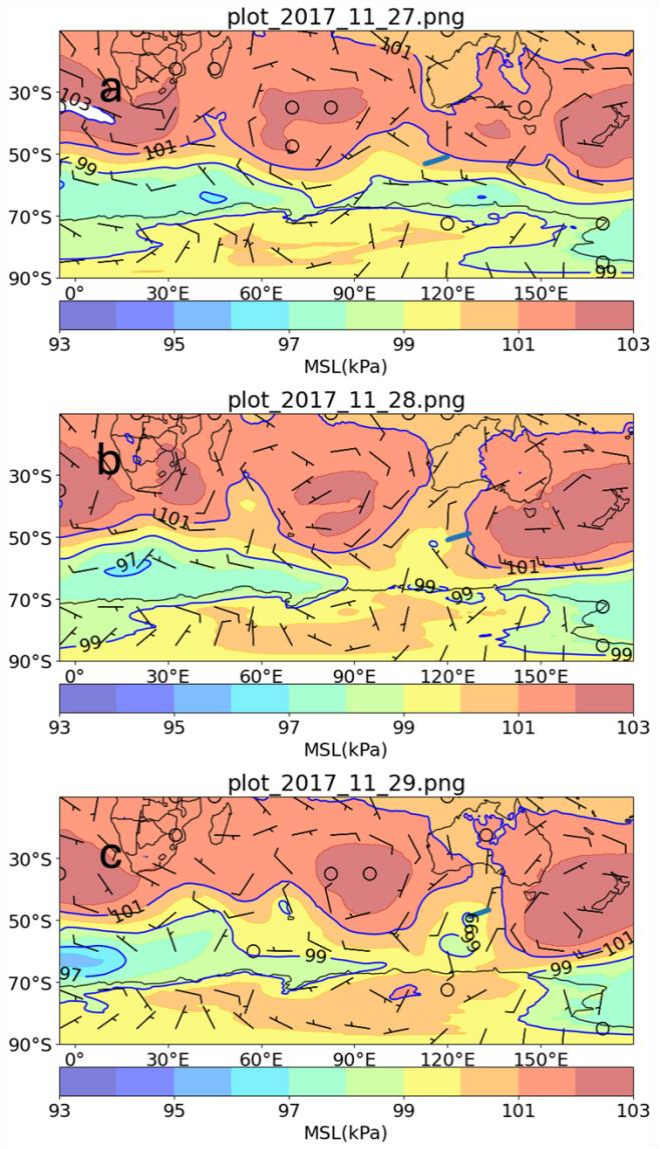

Figure S2.3 The map of mean surface level overlaid with surface wind barbs during the voyage between David and Hobart during November 27th – 29th, 2017 and the ship track each day.

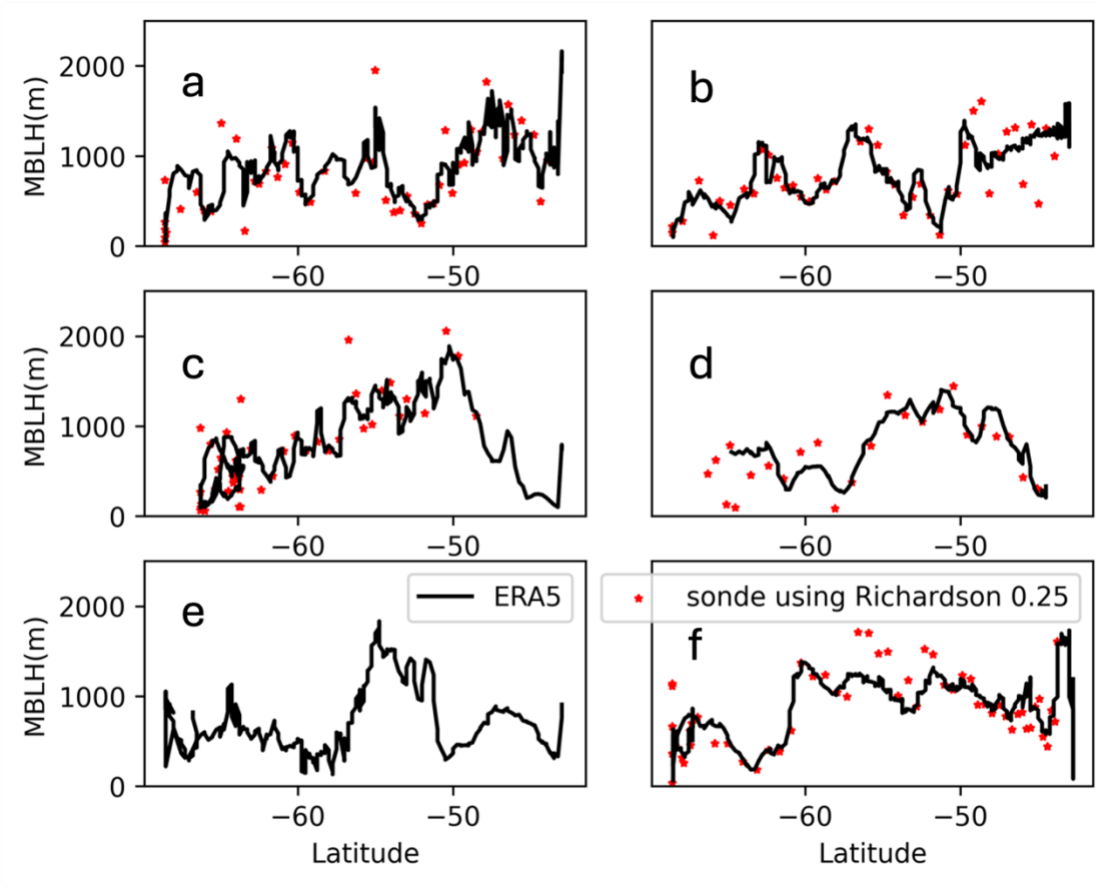

Figure S2.4 Marine Boundary Layer Height (MBLH) as a function of latitude during MARCUS voyages between Hobart and the Antarctic stations. Red dots are the MBLH derived using the sonde data, and black lines are those from the ERA5 after co-location with the AA location.

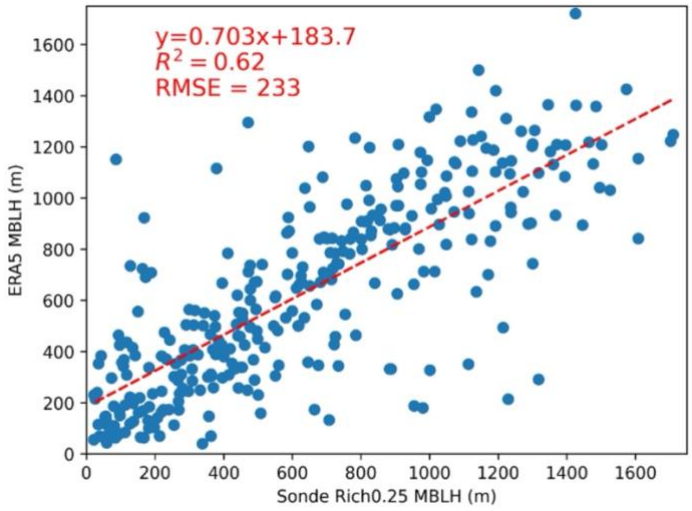

Figure S2.5 Scatter plot of the MBLH derived from soundings released on AA during the voyages between Hobart and Antarctic stations and from ERA5. The red dashed line shows the best linear fit, with the notes for fitting results.

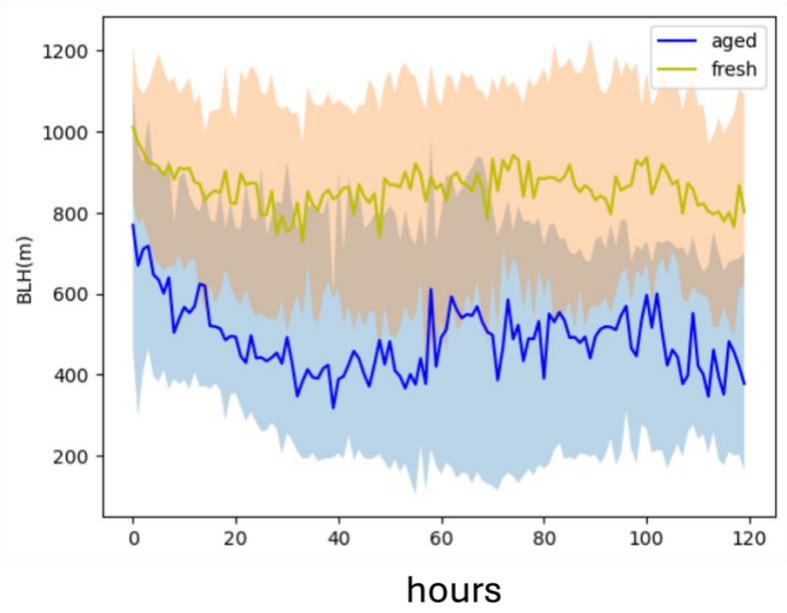

Figure S2.6 Similar to Figure 2.9e but with boundary layer height as a function of time.

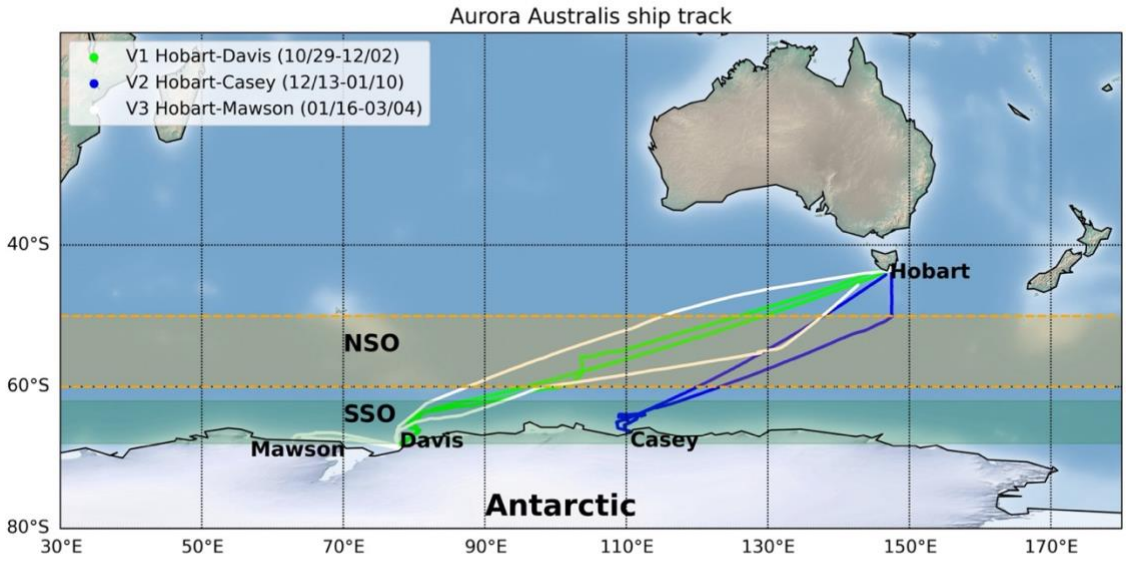

Figure S3.1. Ship tracks of the MARCUS voyages used in this study, with orange shading covering the North Southern Ocean (NSO) and green shading covering the South Southern Ocean (SSO).

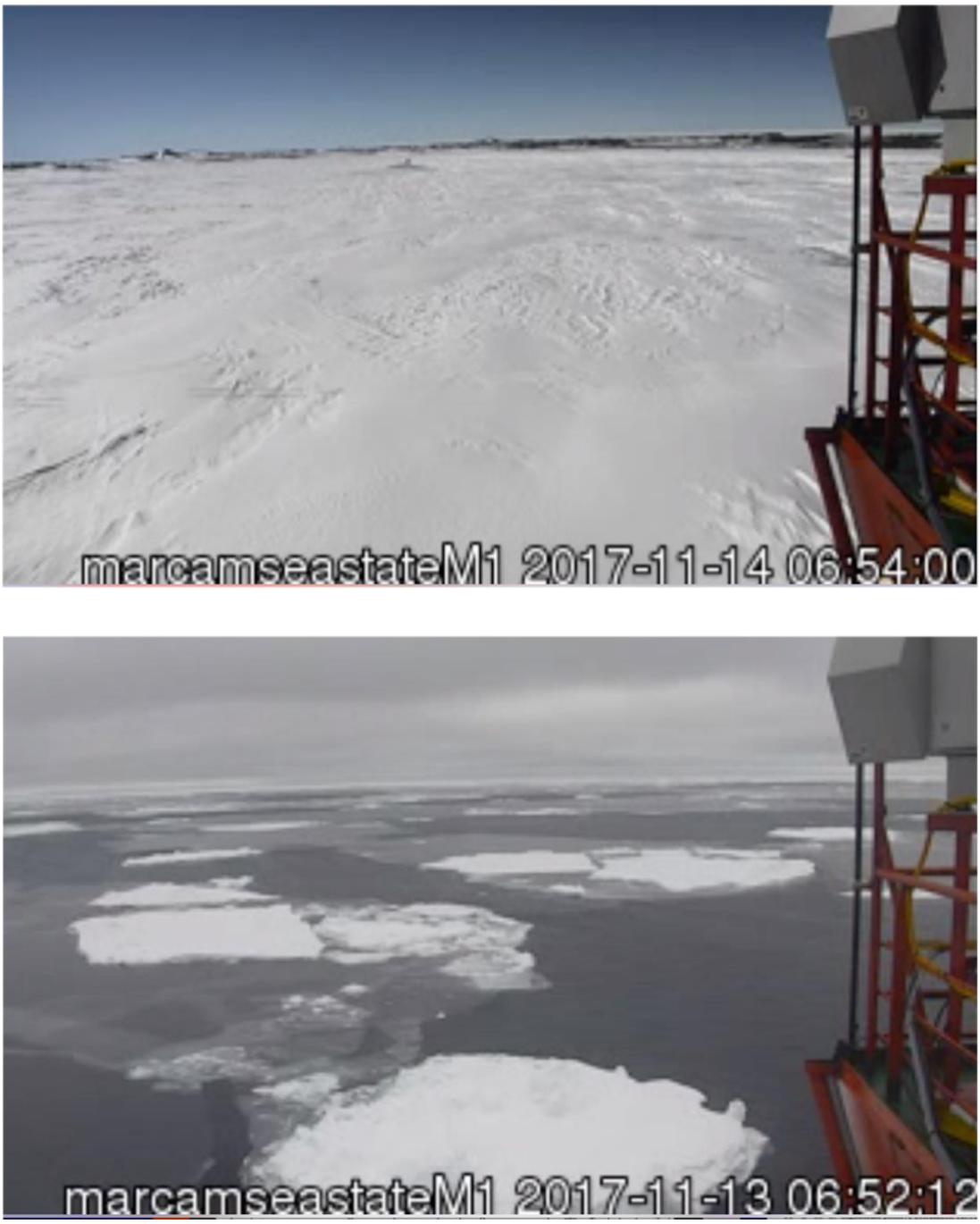

Figure S3.2 Sea ice conditions monitored by the camera during MARCUS (**DOI:** 10.5439/1971079), with manual labels equal to 1 for solid sea ice (top) and equal to 0.5 for scattered sea ice (bottom) close to the Antarctic during the voyage from Hobart to Davis.

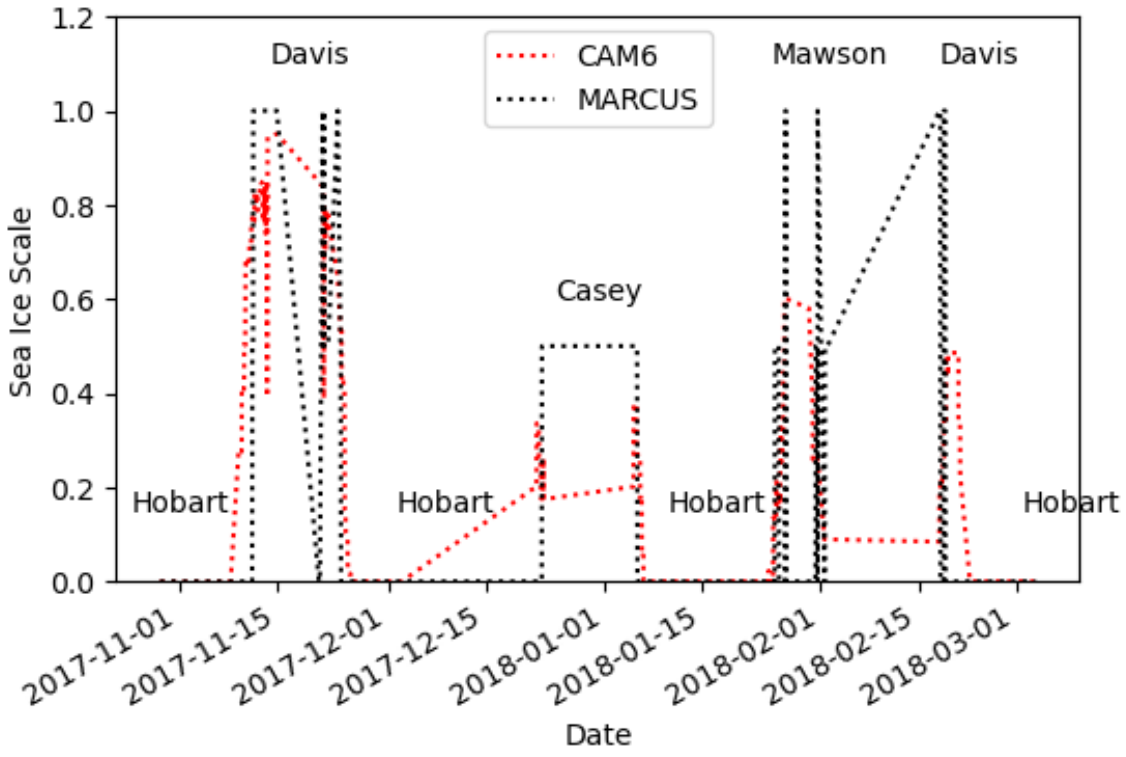

Figure S3.3. Time series of sea ice scales during the first three voyages of MARCUS as simulated from CAM6 (variable "ICEFRAC") in red and observed MARCUS in black.

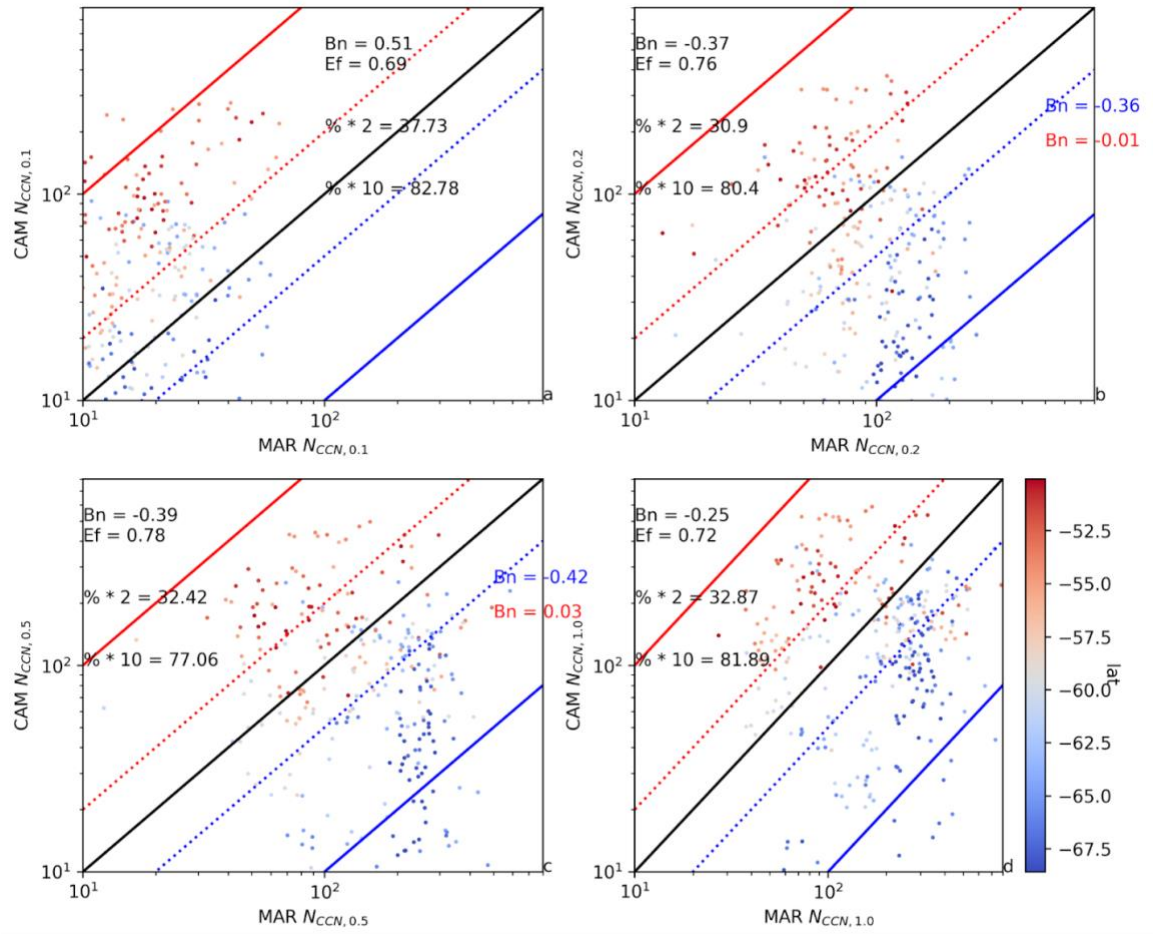

Figure S3.4 As in Figure 3.3 but only including data between 50°S and the Antarctic and for SS_w 0.1% (a), 0.2% (b), 0.5% (c), 1.0% (d), with the red and blue text referring to B_n calculated for 50°S-62°S and 62°S-68°S respectively.

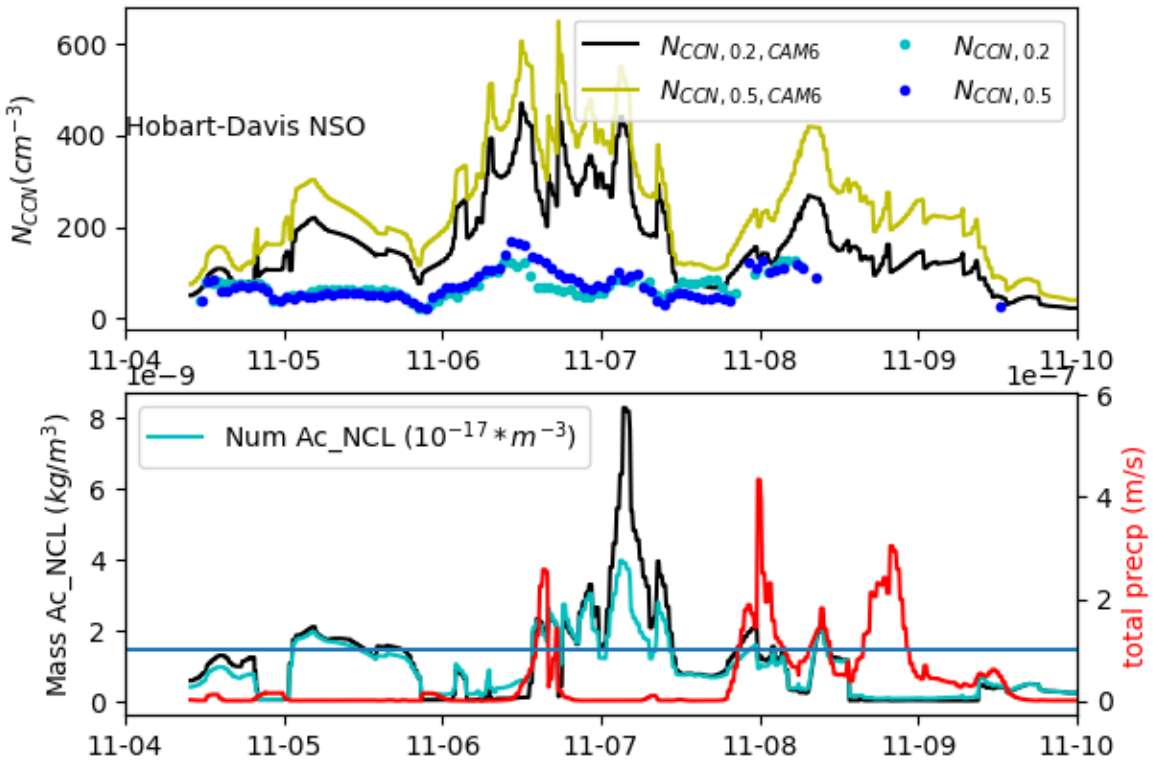

Figure S3.5 Supporting information for Figure 5a, for voyage from Hobart to Davis over the NSO during November 2017, time series of observed $N_{CCN,0.2}$ (blue dots), $N_{CCN,0.5}$ (cyan dots), simulated $N_{CCN,0.2}$ (black line) and $N_{CCN,0.5}$ (yellow dots) on the top; and accumulation mode sea salt mass (black) and number (cyan) concentration, and modeled surface total precipitation (red) on the bottom.

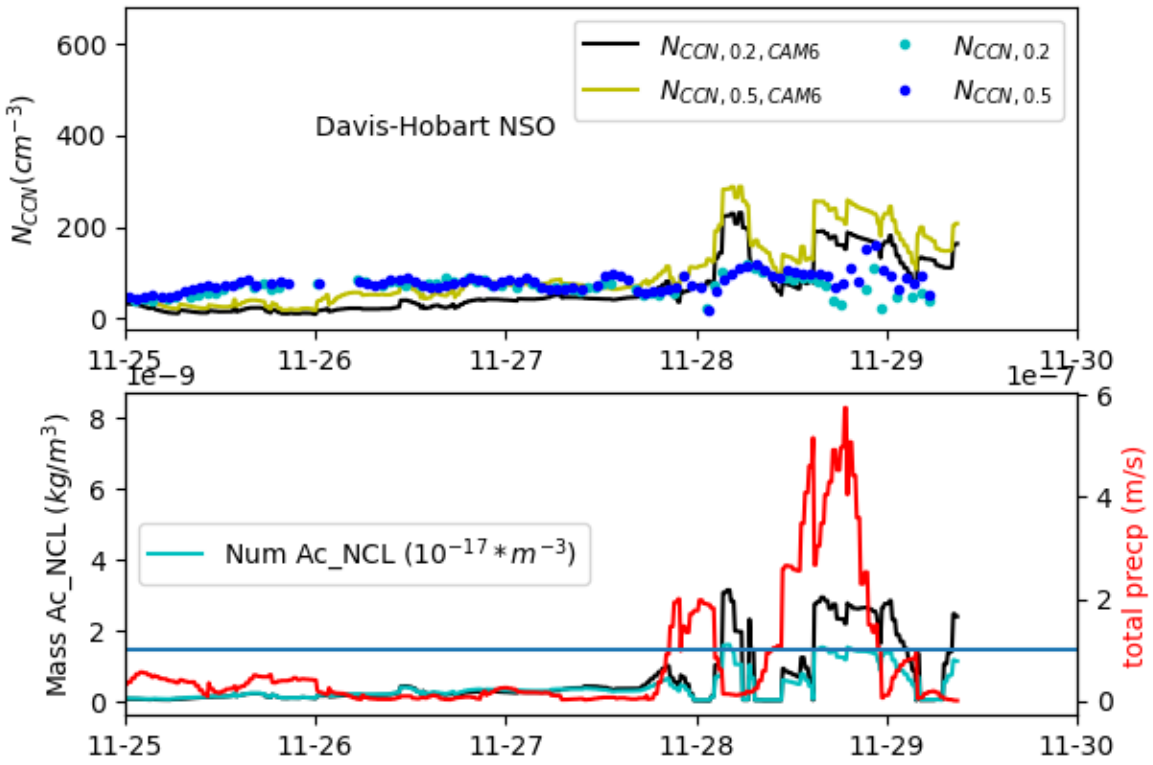

Figure S3.6 As in Figure S5, except for the voyage from Davis to Hobart in November 2017.

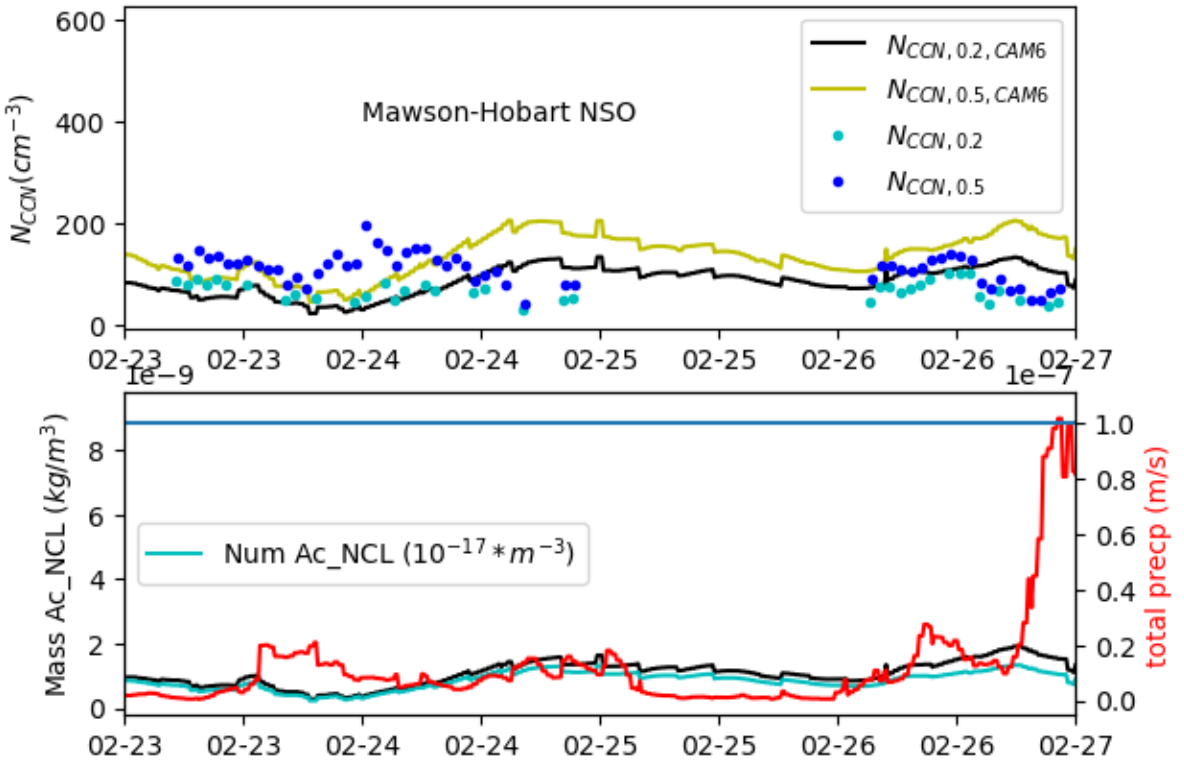

Figure S3.7 As in Figure S5, except corresponding to Figure 5b, for voyage from Mawson to Hobart over the NSO during February 2018.

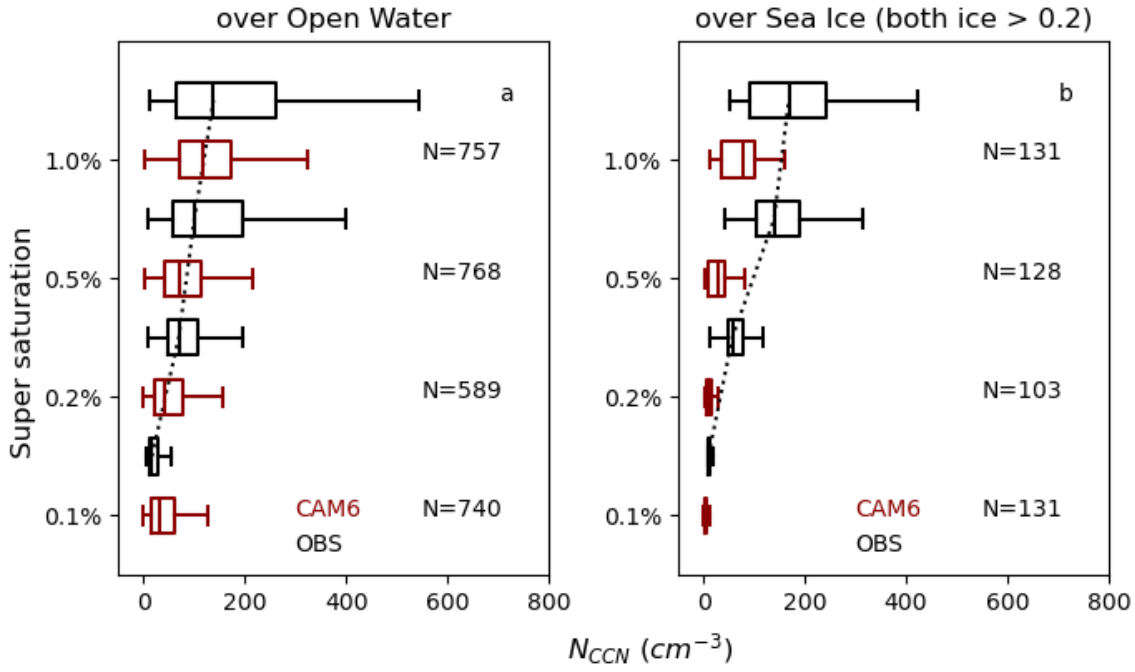

Figure S3.8 As in Figure 3.6, except "over-sea-ice" defined as when both CAM6 and MARCUS show a sea ice scale above 0.2.

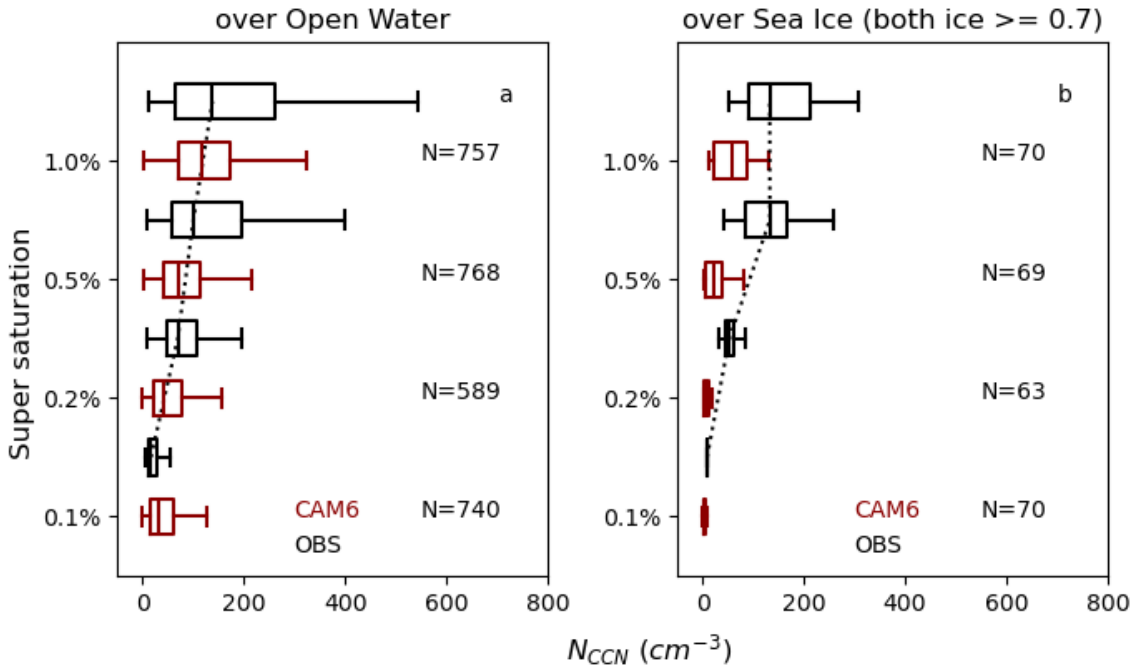

Figure S3.9 As in Figure 3.6, except "over-sea-ice" defined as when both CAM6 and MARCUS show a sea ice scale above 0.7.

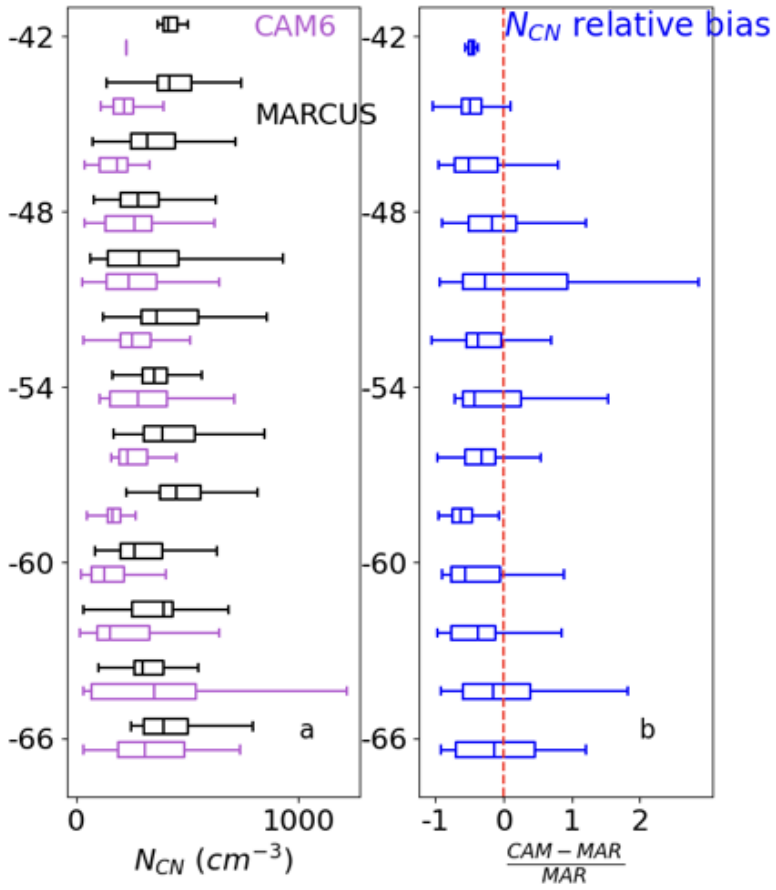

Figure S3.10 Latitudinal dependence of NCN in (a) with observations in black and simulation in red, and the calculated relative biases (b). The dashed line on (b) represents the scenario where simulations and observations perfectly agree (a bias of zero). The whiskers extend from the box to the farthest data point, lying within 1.5 times of the inter-quartile range in each one-degree latitude bin.

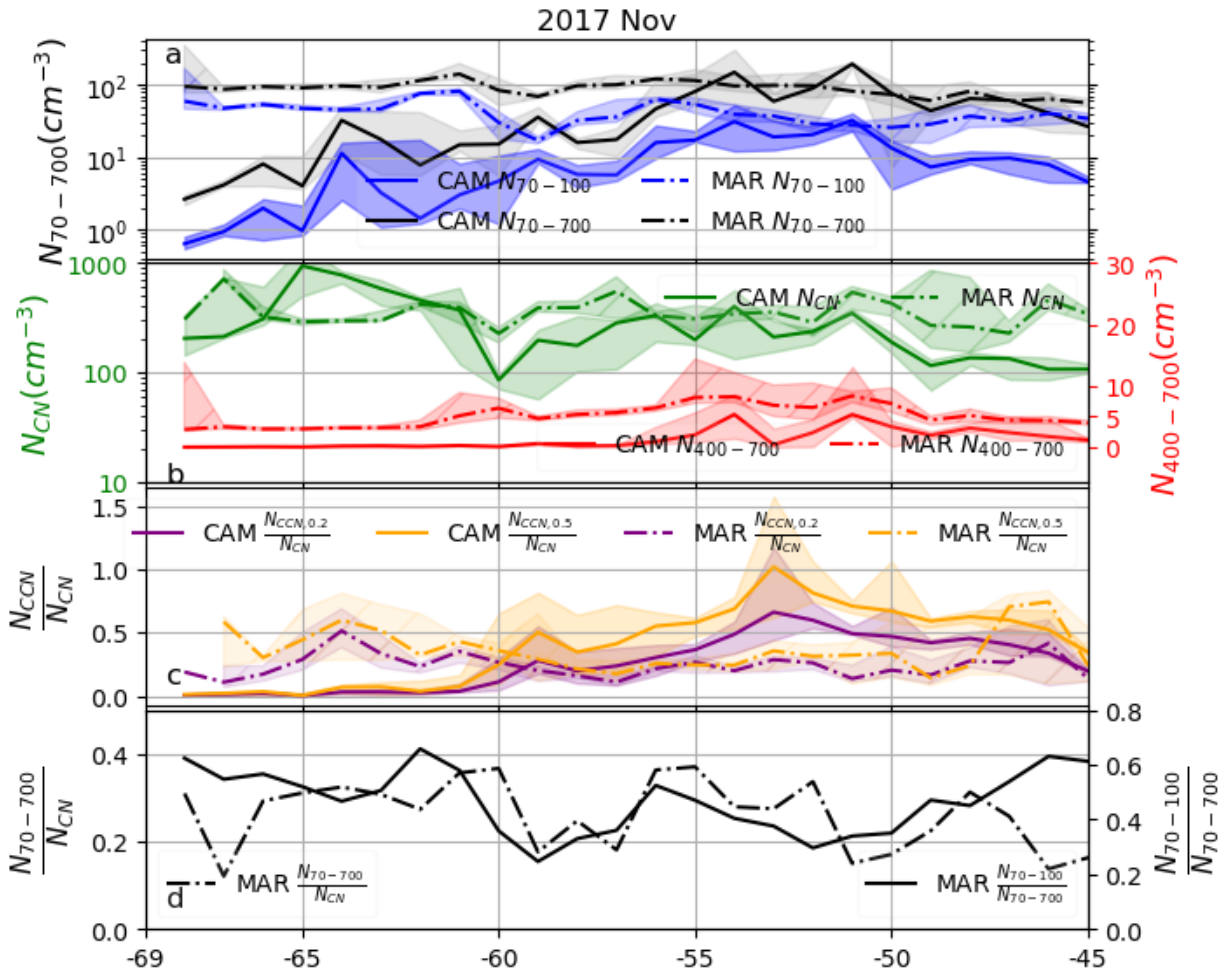

Figure S3.11 Similar to Figure 3.4 but only for data acquired during 2017 November.

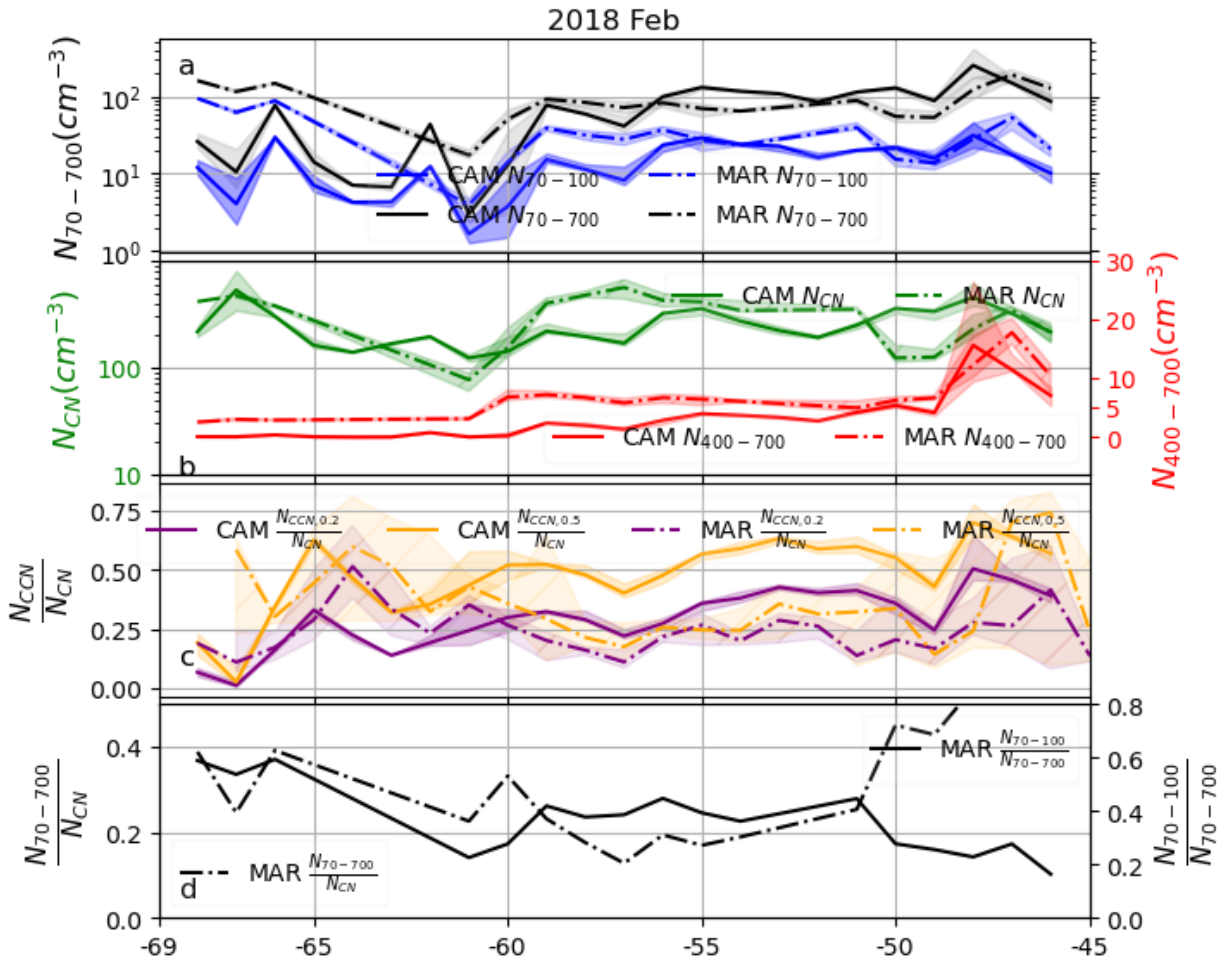

Figure S3.12 Similar to Figure 3.4 but only for data acquired during 2018 February.

Aerosol Mode	σ_g	Low (high) bound (m)	Species
Aitken	1.6	8.70×10^{-9} (5.20×10^{-8})	N, M_{SO4}, M_{SOA}, M_{NCL}
Accumulation	1.6	5.35×10^{-8} (4.80×10^{-7})	N, M_{SO4}, M_{SOA}, M_{POA}, M_{BC}, M_{DST}, M_{NCL}
Coarse	1.2	4.00×10^{-7} (4.00×10^{-5})	N, M_{SO4}, M_{DST}, M_{NCL}
Primary Carbon	1.6	1.00×10^{-8} (1.00×10^{-7})	N, M_{POA}, M_{BC}

Table S3.1 MAM4 modes, smallest and largest size of each mode with the associated species carried, including mode specific number (N) and species-specific mass ($M_{species}$), species include secondary organic aerosol (SOA), dust (DST), sea salt (NCL), sulfate (SO_4), primary organic matter (POA), black carbon (BC).

SS	NSO # Nov (Feb)	SSO # Nov (Feb)
0.1%	184(52)	156(78)
0.2%	160(38)	142(51)
0.5%	186(57)	157(80)
1.0%	187(55)	158(81)

Table S3.2 Observation sample sizes for CCN over the NSO and SSO at different SS_w measured during MARCUS. Each sample represents a 10-minute average.

Text S4.1.

During MARCUS, the Australian icebreaker, Aurora Australis (AA), made three full latitudinal transects over the SO on resupply voyages from Hobart, Australia (42.9°S, 147.3°E) to the Australian Antarctic stations Casey (66.16°S, 110.3°E), Davis (68.3°S, 77.6°E), and Mawson (67.4°S, 62.5°E), as shown as Fig S1. The nature of the resupply voyages means that specific cloud or weather systems were not targeted so that the data collected are expected to be representative of cloud and aerosol conditions over the SO in general. Only the three voyages between Hobart and the Antarctic stations are used in this study. Because effluents from the AA ship stack contaminated aerosols measurements much of the time, periods when ship stack contamination impacted the measurement of aerosols have been removed using the machine learning method of Niu et al. (2024), resulting in 26% data recovery. Details of aerosol instruments are discussed in Niu et al. (2024, 2025).

The simulation used in this study was conducted with the Community Atmosphere Model version 6 (CAM6, Bogenschutz et al., 2018). CAM6 is the atmospheric component of Version 2.1 of the Community Earth System Model (CESM2.1, publicly available at http://www.cesm.ucar.edu/models/cesm2.1/). CAM6 incorporates a two-moment cloud microphysics scheme for four hydrometeor classes (liquid, ice, rain, and snow), following the Morrison-Gettelman MG2 scheme (Gettelman & Morrison, 2015). CAM6 also uses the Cloud Layers Unified by Bi-normals (CLUBB, Golaz et al., 2002; Larson & Golaz, 2005) parameterization for the planetary boundary layer, shallow convection, and cloud macrophysics. CAM6 retains the deep convection scheme of Zhang and McFarlane (1995).

Here, sea ice was based on the monthly mean climatology from the Community Ice CodE (CICE5, Hunke et al., 2015). Aerosols in CAM6 are predicted by a four-mode version of the Modal Aerosol Module (MAM4) (Liu et al., 2016), initialized based on climatological profiles in 2000 from the CMIP6 emissions inventory (Feng et al., 2020).

The CAM6 simulation was performed with specified dynamics for surface temperature and winds (i.e., nudging) to Modern ERA-retrospective Analysis for Research and Applications (MERRA-2) reanalysis with a 24-hr relaxation timescale, following the model setup of Gettelman et al. (2020). A finite-volume dynamical core of 0.9° longitude -1.2°latitude resolution was used with 32 vertical levels and a model time step of 30 min. The model output was written to disk every 10 min. For co-located comparisons of model output against observations, the 1-min averaged ship track was used to determine the geographic location of the ice breaker at a given time. The closest grid cell and the closest time steps were used in each interpolation to obtain a singular value at the ship location at a given time within a voyage. CCN are hourly measured for cycling through different supersaturations (Niu et al. 2024, 2025), while the receival of cloud droplet number has been output every 30 seconds (Mace et al. 2024a). One of the key input variables, averaged liquid water path from microwave radiometer is shown in Fig S3. Further quality controls of the remote sensing data include 1) a passed convergence test of the computations of both cloud droplet number concentration (N_d) and effective cloud radius (R_e), 2) a passed test of the cloud layer adiabaticity, 3) the retrieved N_d < 1000 cm^{-3}, and 4) the retrieved R_e <50 um. Retrievals are first averaged by 10 minutes to reduce the noise and then are resampled hourly to match the simulation at the closest timestep.

Vertically, the lowest level (with a valid value) in the simulated cloud layer is used to compare with the retrieved cloud base N_d.

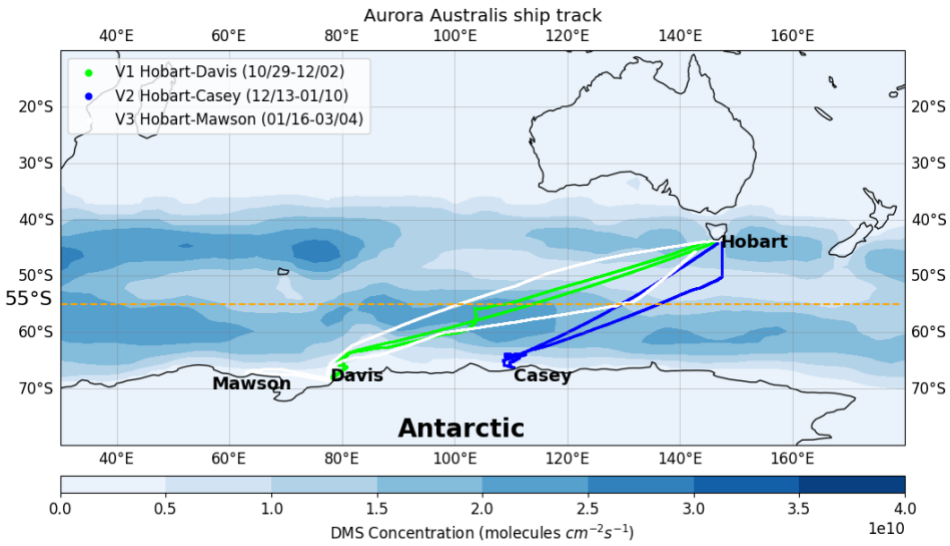

Figure S4.1 Ship tracks during MARCUS with voyages between the Australian Antarctic stations and Hobart, Australia illustrated by color as shown in legend. The orange line represents 55°S. The background color represents the monthly mean of surface ocean DMS emission in January 2018 from the Chemistry Climate Model Initiative.

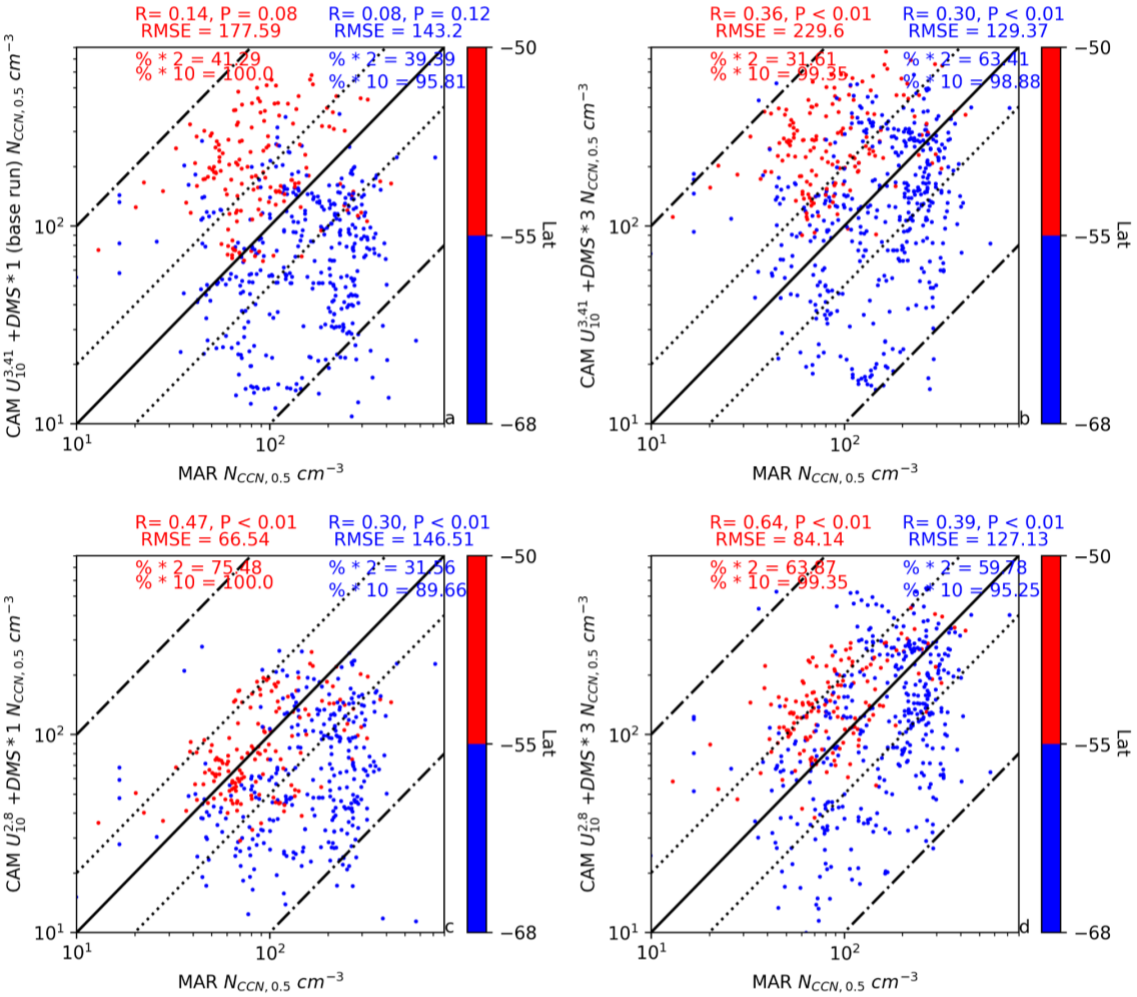

Figure S4.2 As Figure 1 but for $N_{CCN,0.5}$.

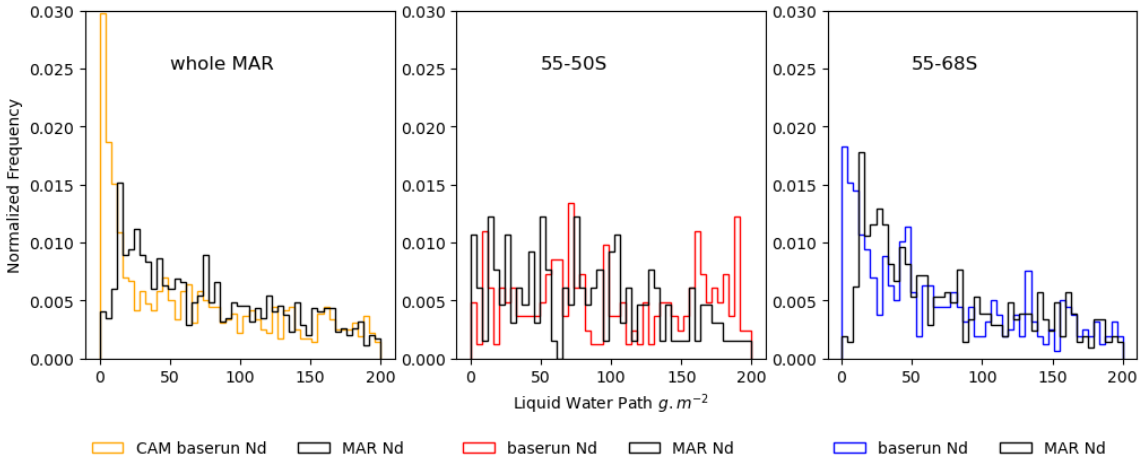

Figure S4.3 As Figure 4 but for liquid water path (LWP).

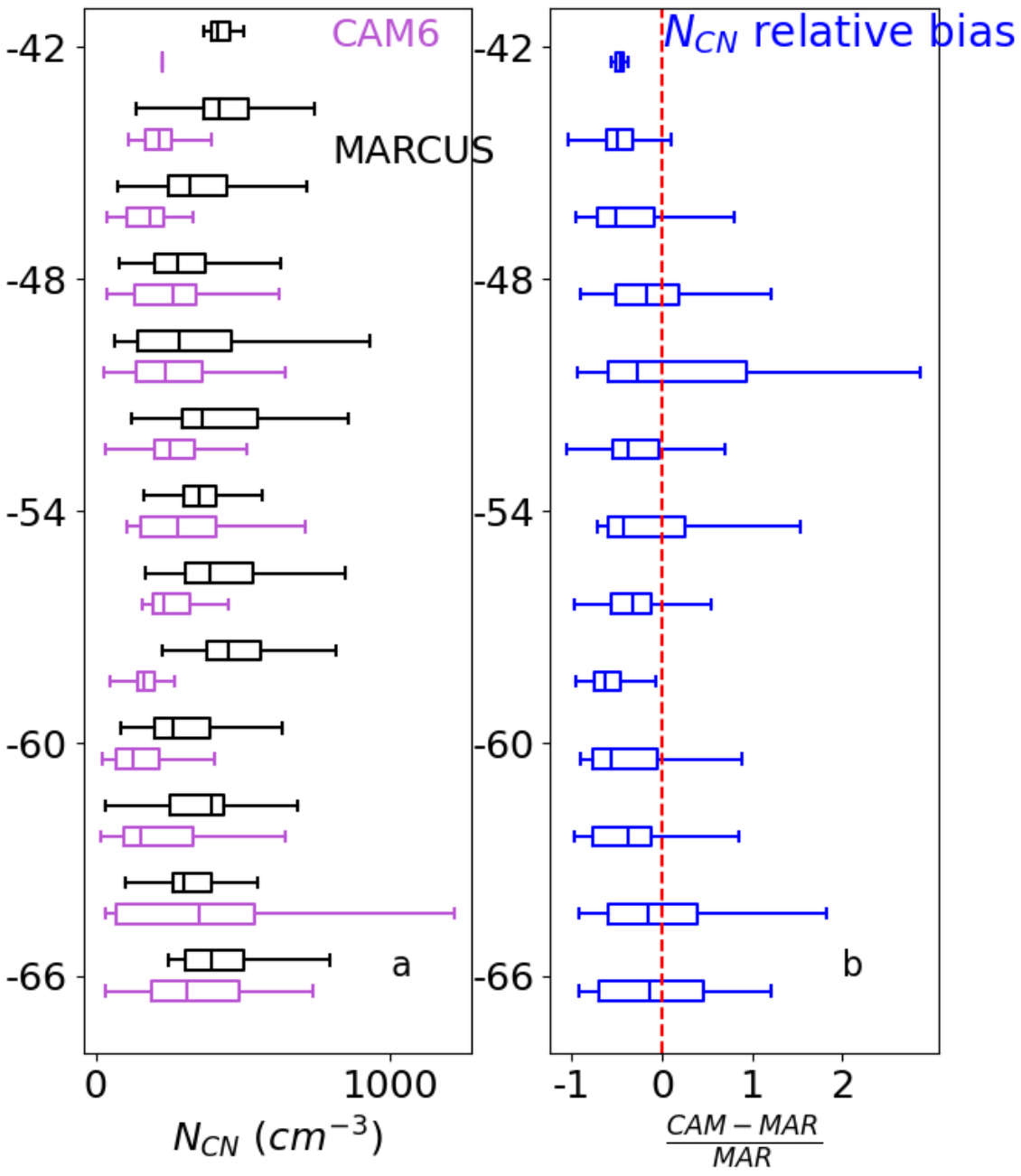

Figure S4.4 a) Latitudinal dependence of N_{CN} with observations in black and simulations in red, and **b)** the calculated relative biases. The dashed line in (b) represents the scenario where simulations and observations perfectly agree (a bias of zero). The whiskers extend from the box to the farthest data point lying within 1.5 times of the inter-quartile range in each one-degree latitude bin.

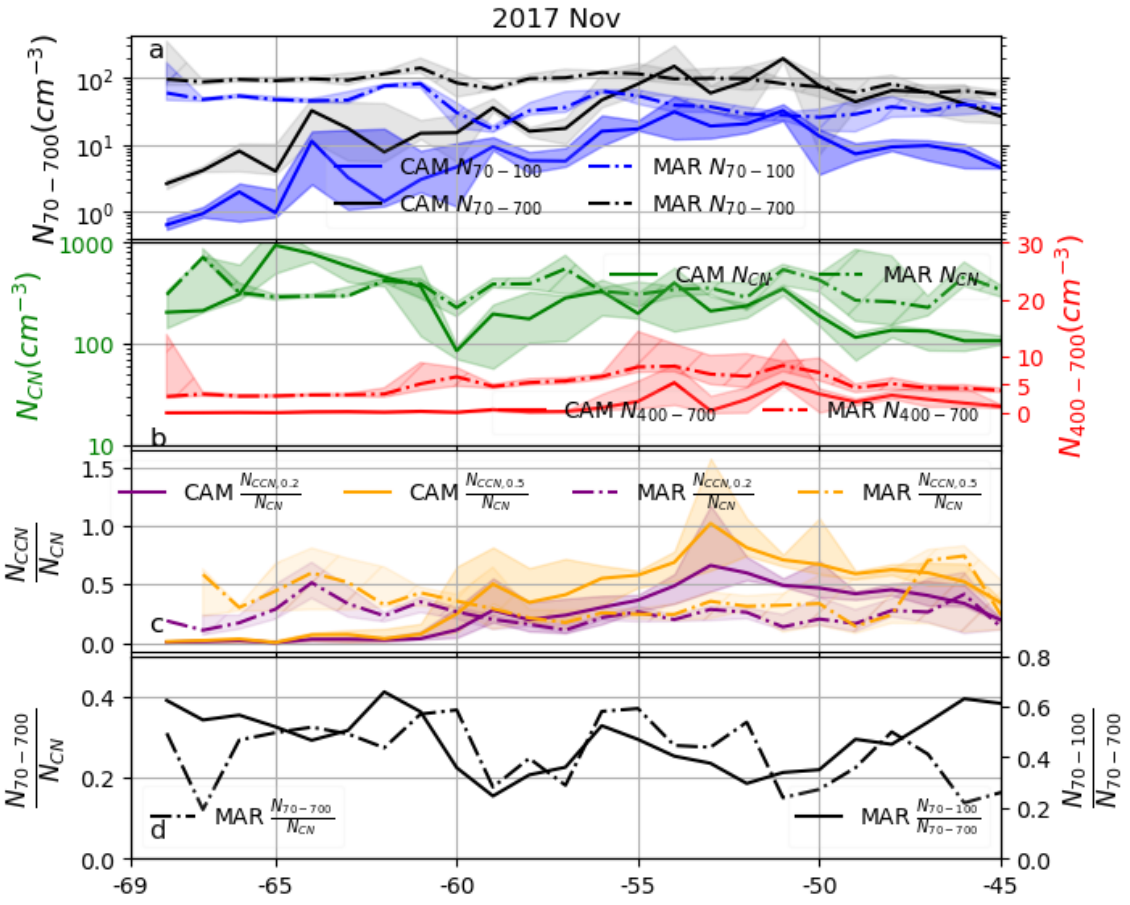

Figure S4.5 Similar to Figure 4.4 but only for data acquired during 2017 November.

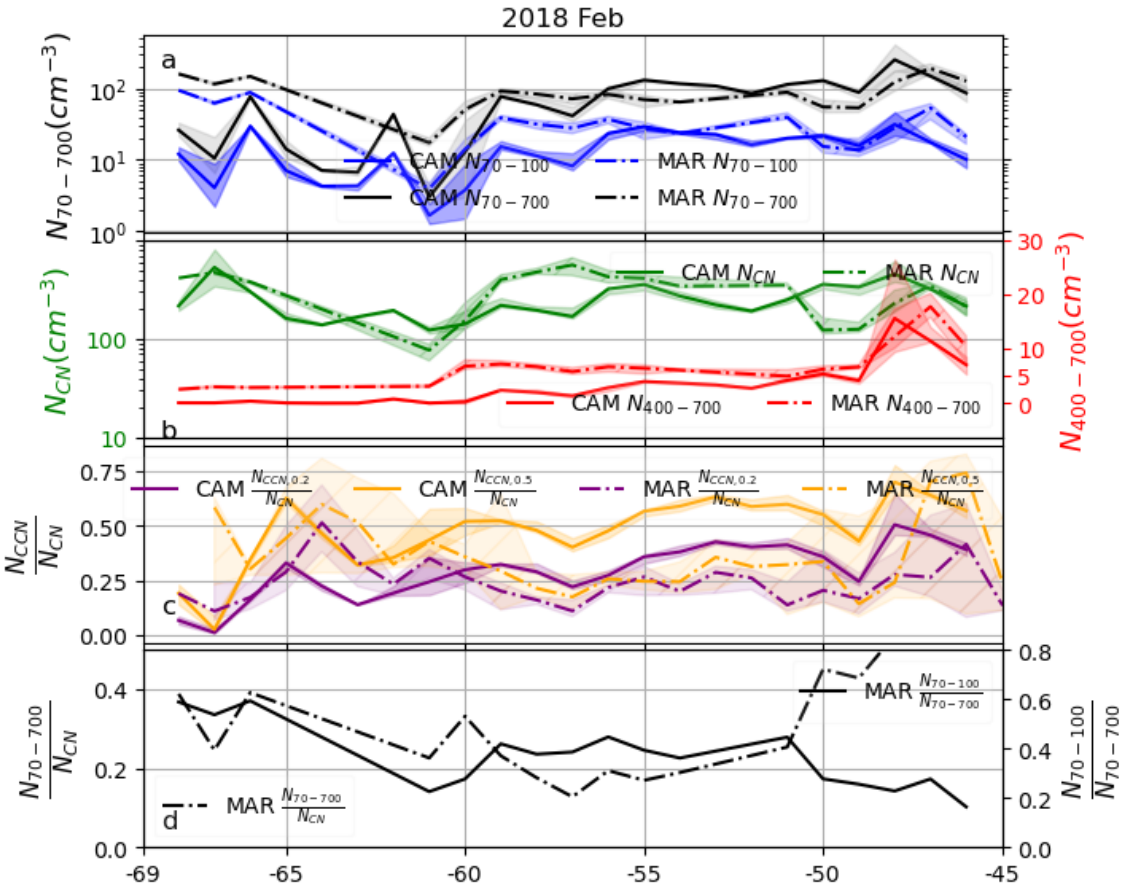

Figure S4.6 Similar to Figure 4.4 but only for data acquired during 2018 February.

	DMS (default)	**DMS*2**	**DMS*3**	**DMS*10**
$U_{10}^{3.41}$ (default)	Base run	$U_{10}^{3.41}$+DMS*2	$U_{10}^{3.41}$+DMS*3	$U_{10}^{3.41}$+DMS*10
$U_{10}^{2.8}$	$U_{10}^{2.8}$+DMS	$U_{10}^{2.8}$+DMS*2	$U_{10}^{2.8}$+DMS*3	$U_{10}^{2.8}$+DMS*10

Table S4.1 Sensitivity tests configuration and acronyms used in this study.